February 1999

Effects of Grit Roughness and Pitch Oscillations on the L303 Airfoil

J. M. Janiszewska
R. Reuss Ramsay
J. D. Lee
G. M. Gregorek
The Ohio State University
Columbus, Ohio

National Renewable Energy Laboratory
1617 Cole Boulevard
Golden, Colorado 80401-3393
A national laboratory of the U.S. Department of Energy
Managed by Midwest Research Institute
for the U.S. Department of Energy
under contract No. DE-AC36-83CH10093

Foreword

Airfoils for wind turbines have been selected by comparing data from different wind tunnels, tested under different conditions, making it difficult to make accurate comparisons. Most wind tunnel data sets do not contain airfoil performance in stall commonly experienced by turbines operating in the field. Wind turbines commonly experience extreme roughness for which there is very little data. Finally, recent tests have shown that dynamic stall is a common occurrence for most wind turbine operating in yawed, stall or turbulent conditions. Little dynamic stall data exists for the airfoils of interest to a wind turbine designer. In summary, very little airfoil performance data exits which is appropriate for wind turbine design.

Recognizing the need for a wind turbine airfoil performance data base, the National Renewable Energy Laboratory (NREL), funded by the U.S. Department of Energy, awarded a contract to Ohio State University (OSU) to conduct a wind tunnel test program. Under this program, OSU tested a series of popular wind turbine airfoils. A standard test matrix was developed to assure that each airfoil was tested under the same conditions. The test matrix was developed in partnership with industry and is intended to included all of the operating conditions experienced by wind turbines. These conditions include airfoil performance at high angles of attack, rough leading edge (bug simulation), steady and unsteady angles of attack.

Special care has been taken to report as much of the test conditions and raw data as practical so that designers can make their own comparisons and focus on details of the data relevant to their design goals. Some of the airfoil coordinates are proprietary to NREL or an industry partner. To protect the information which defines the exact shape of the airfoil, the coordinates have not been included in the report. Instructions on how to obtain these coordinates may be obtained by contacting C.P. (Sandy) Butterfield at NREL.

C.P. (Sandy) Butterfield
Wind Technology Division
National Renewable Energy Laboratory
1617 Cole Blvd.
Golden, Colorado, 80401 USA
Internet Address: Sandy_Butterfield@NREL.GOV
Phone 303-384-6902
FAX 303-384-6901

Preface

The Ohio State University Aeronautical and Astronautical Research Laboratory is conducting a series of steady state and unsteady wind tunnel tests on a set of airfoils which have been or will be used for horizontal axis wind turbines. The purpose is to investigate the effect of pitch oscillations and leading edge grit roughness on airfoil performance. The study of pitch oscillation effects can help to understand the behavior of horizontal axis wind turbines in yaw. The results of these tests will aid in the development of new airfoil performance codes which account for unsteady behavior and also aid in the design of new airfoils for wind turbines. The application of leading edge grit roughness (LEGR) simulates surface irregularities that occur on wind turbines. These irregularities on the blades are due to the accumulation of insect debris, ice, and/or the aging process and can significantly reduce the output of the horizontal axis wind turbines. The experimental results from the application of leading edge grit roughness will help develop airfoils that are less sensitive to roughness.

The present work was made possible by the efforts and financial support of the National Renewable Energy Laboratory which provided major funding and technical monitoring, the U.S. Department of Energy is credited for it funding of this document through the National Renewable Energy Laboratory under contract number DE-AC36-83CH10093. The staff of The Ohio State University Aeronautical and Astronautical Research Laboratory appreciate the contributions made by personnel from that organization. In addition, the authors would like to recognize the efforts of Michael Peterson, an undergraduate student research assistant.

Summary

A NREL L303 airfoil model was tested in The Ohio State University Aeronautical and Astronautical Research Laboratory 3×5 subsonic wind tunnel under steady state and unsteady conditions. The test defined baseline conditions for steady state angles of attack from -20° to +40° and examined unsteady behavior by oscillating the model about its quarter chord pitch axis for three mean angles, three frequencies, and two amplitudes. For all oscillating cases, Reynolds numbers of 0.75, 1, and 1.25 million were used. In addition, the above conditions were repeated after the application of leading edge grit roughness (LEGR) to determine contamination effects on the airfoil performance.

Typical steady state results of the L303 testing showed a baseline maximum lift coefficient of 1.29 at 21.0° angle of attack for 1 million Reynolds number. The application of LEGR reduced the maximum lift coefficient by 35% and increased the minimum drag coefficient value by 105%. The zero lift pitching moment coefficient of -0.0449 showed an 87% decrease in magnitude to -0.0058 with LEGR applied.

Data were also obtained for two pitch oscillation amplitudes, ±5.5° and ±10°. The larger amplitude consistently gave a higher maximum lift coefficient than the smaller amplitude and both sets of unsteady maximum lift coefficients were greater than the steady state values. Stall was delayed on the airfoil while the angle of attack was increasing, thereby causing an increase in maximum lift coefficient. A hysteresis behavior was exhibited for all the unsteady test cases. The hysteresis loops were larger for the higher reduced frequencies and for the larger amplitude oscillations. As in the steady case, the effect of LEGR in the unsteady case was to reduce the lift coefficient at high angles of attack. In addition, the hysteresis behavior persisted into lower angles of attack than was observed under clean conditions.

In general, the unsteady maximum lift coefficient was up to 110% higher than the steady state maximum lift coefficient, and variation in the quarter chord pitching moment coefficient magnitude was close to the steady state values at high angles of attack and close to zero. These findings indicate the importance of considering the unsteady flow behavior occurring in wind turbine operation because use of steady values could result in grossly inaccurate loads.

Contents Page

List of Figures Page

List of Tables Page

List of Symbols

AOA	Angle of attack
A/C, a.c.	Alternating current
c	Model chord length
C_d	Drag coefficient
C_{dmin}	Minimum drag coefficient
C_{dp}	Pressure drag coefficient
C_{dw}	Wake drag coefficient
C_{du}	Uncorrected drag coefficient
C_l	Lift coefficient
C_{lmax}	Maximum lift coefficient
$C_{l\ dec}$	Lift coefficient at angle of maximum lift, but with angle of attack decreasing
C_{lu}	Uncorrected lift coefficient
C_m, $C_{m¼}$	Pitching moment coefficient about the quarter chord
$C_{m\ dec}$	Pitching moment coefficient at angle of maximum lift, but with angle of attack decreasing
$C_{m\ inc}$	Pitching moment coefficient at angle of maximum lift, but with angle of attack increasing
C_{mo}	Pitching moment coefficient about the quarter chord, at zero lift
$C_{m¼u}$	Uncorrected pitching moment coefficient about the quarter chord
C_p	Pressure coefficient, $(p- p_\infty)/q_\infty$
C_{pmin}	Minimum pressure coefficient
f	Frequency
h	Wind tunnel test section height
hp, Hp, HP	Horsepower
Hz	Hertz
k	Grit particle size
k/c	Grit particle size divided by airfoil model chord length
p	Pressure
q	Dynamic pressure
q_u	Uncorrected dynamic pressure
q_w	Dynamic pressure through the model wake
q_∞	Free stream dynamic pressure
Re	Reynolds number
Re_u	Uncorrected Reynolds number
t	Time
U_∞	Corrected free stream velocity
V	Velocity
V_u	Uncorrected velocity
x	Axis parallel to model reference line
y	Axis perpendicular to model reference line

α	Angle of attack
α_{dec}	Decreasing angle of attack
α_{inc}	Increasing angle of attack
α_{m}	Median angle of attack
α_{mean}	Mean angle of attack
α_{u}	Uncorrected angle of attack
ϵ	Tunnel solid wall correction scalar
ϵ_{sb}	Solid blockage correction scalar
ϵ_{wb}	Wake blockage correction scalar
Λ	Body-shape factor (0.305 used)
π	3.1416
σ	Tunnel solid wall correction parameter
ω_{red}, $\omega_{reduced}$	Reduced frequency, $\pi fc/U_{\infty}$

Introduction

Horizontal axis wind turbine rotors experience unsteady aerodynamics due to wind shear when the rotor is yawed, when rotor blades pass through the support tower wake, and when the wind is gusting. An understanding of this unsteady behavior is necessary to assist in the design of new rotor airfoils. The rotors also experience performance degradation due to surface roughness. These surface irregularities are due to the accumulation of insect debris, ice, and the aging process. Wind tunnel studies that examine both the steady and unsteady behavior of airfoils can help define pertinent flow phenomena, and the resultant data can also be used to validate analytical computer codes.

The L303 airfoil design resulted from a request by NREL for an airfoil suitable for application to the root sections of HAWT rotors. In these applications, thick airfoils are required (t/c in excess of 25%), for structural considerations with operation to high angles of attack. Experience has shown that thick airfoils are less susceptible to excessive flow separation when they have relatively blunt trailing edges as opposed to the sharp trailing edges of conventional sections. The AARL/OSU has developed techniques for analyzing such airfoils since they are typically required for application to the inboard sections of propellers.

A NREL L303 airfoil model was tested in The Ohio State University Aeronautical and Astronautical Research Laboratory (OSU/AARL) 3×5 subsonic wind tunnel (3×5) under steady flow with stationary model conditions, and with the model undergoing pitch oscillations. To study the possible extent of performance loss due to surface roughness, a standard grit pattern (LEGR) was used to simulate leading edge contamination. After baseline cases were completed, the LEGR was applied for both steady state and model pitch oscillation cases. The Reynolds numbers for steady state conditions were 0.75, 1, and 1.25 million, for the angle of attack range from -20° to +40°. While the model underwent pitch oscillations, data was acquired at Reynolds numbers of 0.75, 1, and 1.25 million, at frequencies of 0.6, 1.2, and 1.8 Hz. Two sine wave forcing functions were used; ±5.5° and ±10°, at mean angles of attack of 7°, 13°, and 19°. For purposes herein, any reference to unsteady conditions means the model was in pitch oscillation.

Experimental Facility

Wind Tunnel

The OSU/AARL 3×5 was used to conduct tests on the L303 airfoil section. Schematics of the top and side views of the tunnel are shown in figures 1 and 2. This open circuit tunnel had a velocity range of 0 - 55 m/s (180 ft/s) produced by a 2.4-m (8-ft) diameter, six-bladed fan. The fan was belt driven by a 93.2-kw (125-hp)

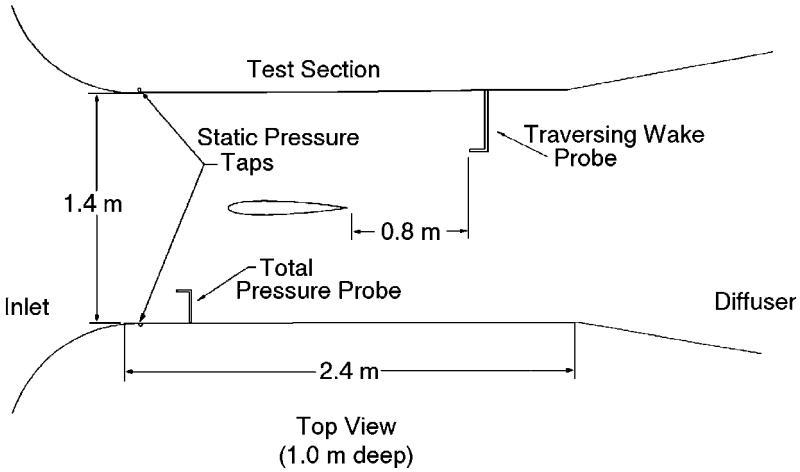

Figure 1. 3×5 wind tunnel, top view.

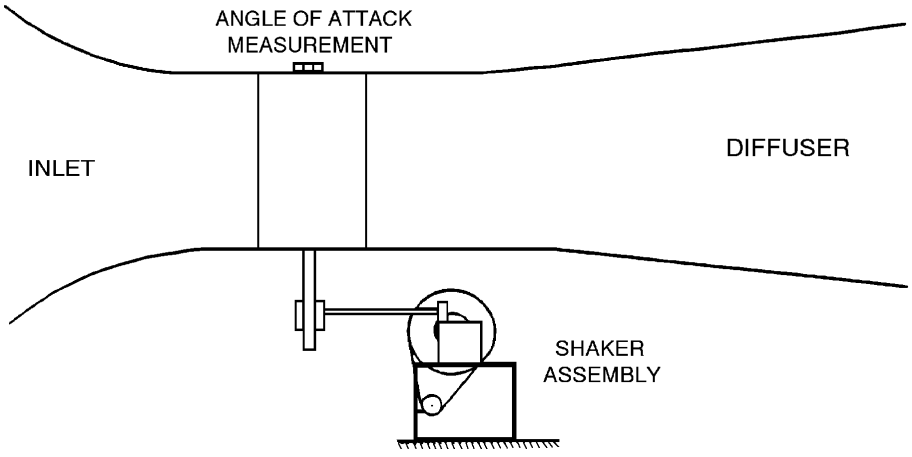

Figure 2. 3×5 wind tunnel, side view.

three phase a.c. motor connected to a variable frequency motor controller. Nominal test section dimensions were 1.0-m (39-in) high by 1.4-m (55-in) wide by 2.4-m (96-in) long. The 457-mm (18-in) chord airfoil model was mounted vertically in the test section. A steel tube through the quarter chord of the model was used to attach the model to the tunnel during testing. An angle of attack potentiometer was fastened to the model at the top of the tunnel as shown in figure 2. The steady state angle of attack was adjusted with a worm gear drive attached to the model strut below the tunnel floor.

Oscillation System

Portions of the testing required the use of a reliable model pitch oscillation system. The OSU/AARL "shaker" system incorporated a face cam and follower arm attached to the model support tube below the wind tunnel floor, figure 3. The choice of cam governed the type and amplitude of the wave form produced. Sine wave forms having amplitudes of ±5.5° and ±10° were used for these tests; the wave form is defined by the equation

$$\alpha = \alpha_m + A\sin(2\pi ft)$$

where A is the respective amplitude. The shaker system was powered by a 5-hp a.c. motor with a variable line frequency controller. The useable oscillating frequency range was 0.1 - 2.0 Hz, with three frequencies used for this test: 0.6, 1.2, and 1.8 Hz.

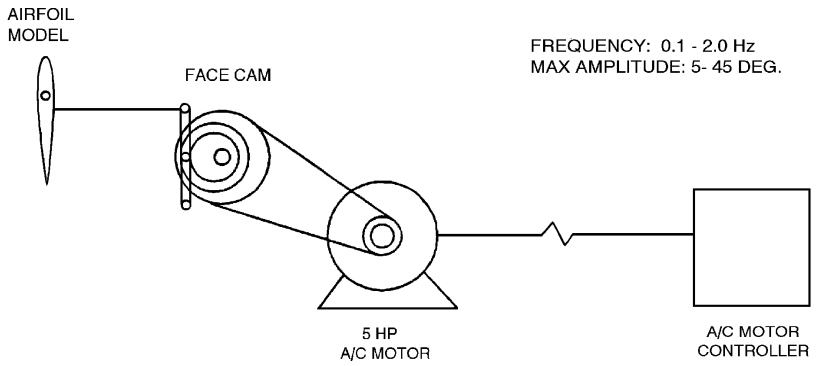

Figure 3. 3×5 wind tunnel oscillation system.

Model Details

A 457-mm (18-in) constant chord L303 airfoil model was designed and manufactured for the 3×5 wind tunnel test program. Figure 4 shows the airfoil section. The model coordinates are presented in tabular form in appendix A. The physical configuration was selected with a maximum thickness of 30% and a trailing

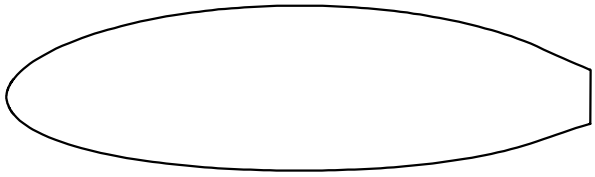

Figure 4. L303 airfoil section.

edge of 10%. Aerodynamically, the design lift coefficient goal was a nominal 0.3 with the capability for a maximum of 1.2 with a "soft stall" thereafter. The front 60% of the contour was derived by cambering a modified ellipse. The rear contours were adjusted iteratively to achieve a positive pressure coefficient in the thick base region in order to keep the pressure drag low near the design lift. The experimental results have confirmed that all the aerodynamic design goals were met or exceeded. Thus this airfoil represents a good baseline section from which others may be designed by further extrapolation of the design technique.

The model was constructed from a nine layer composite lay up of alternating fiberglass and carbon fiber over ribs. The main load bearing member was a 38-mm (1.5-in) diameter steel tube which passed through the model quarter chord station. Ribs and end plates were used to transfer loads from the composite skin to the steel tube. The final surface was filled, painted and wet sanded to attain given coordinates within a requested tolerance of ±0.25 mm (±0.01 inches). The completed model was measured at three spanwise locations using a Sheffield-Cordax coordinate measurement machine. Measurements were made in English units and later converted to metric. Figure 5 shows the results of comparing measured-to-desired coordinates by calculating differences normal to the profiled surface at three stations on the model. The manufactured model was slightly smaller than the designed coordinates specified but still acceptable.

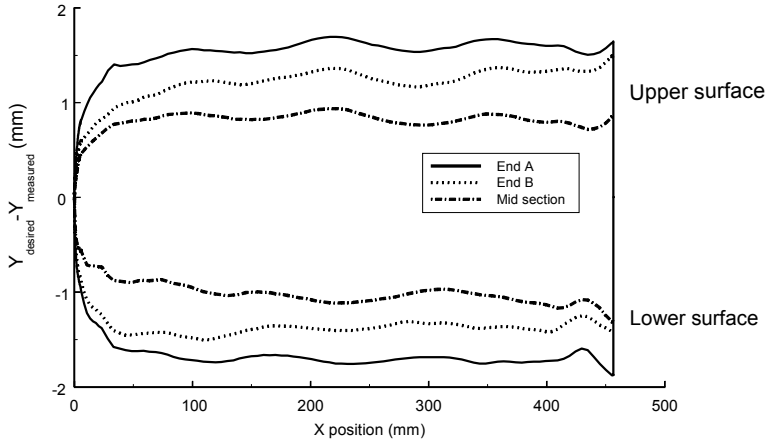

Figure 5. Measured-to-desired model coordinates difference curves.

To minimize pressure response times, which is important for the unsteady testing, the lengths of surface pressure tap lead-out lines had to be as short as possible. Consequently, a compartment was built into the

model and the pressure scanning modules were installed inside the model. This compartment was accessed through a panel door fitted flush with the model contour on the lower (pressure) surface.

For test cases involving roughness, a standard roughness pattern developed for the National Renewable Energy Laboratory airfoil test program was employed. The pattern was generated using a molded insect pattern taken from a wind turbine in the field. The particle density was 5 particles per cm^2 (32 particles per square inch) in the middle of the pattern, thinning to 1.25 particles per cm^2 (8 particles per square inch) at the edge of the pattern. Figure 6 shows the roughness pattern. To make a usable template, the pattern was repeatedly cut into a steel sheet 102-mm (4-in) wide and 91-cm (3-ft) long with holes just large enough for one grain of grit. Based on average particle size from the field specimen, standard #40 lapidary grit was chosen for the roughness elements, giving a particle height to chord ratio of 0.0019 for a 457-mm (18-in) chord model.

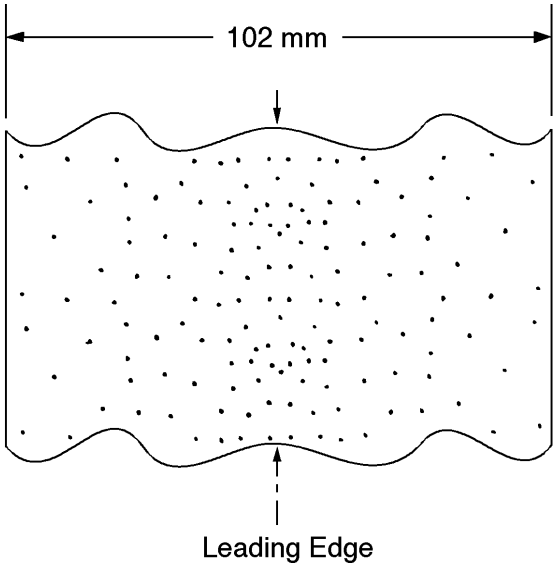

Figure 6. Roughness pattern.

To use the template, 102-mm (4-in) wide double-sided tape was applied to one side of the template and grit was poured and brushed from the opposite side. The tape was then removed from the template and transferred to the model. This method allowed the same roughness pattern to be replicated for any test.

Test Equipment and Procedures

Data Acquisition

Data were acquired and processed from 62 surface pressure taps, four individual tunnel pressure transducers, an angle of attack potentiometer, a wake probe position potentiometer, and a tunnel thermocouple. The data acquisition system included an IBM PC compatible 80486-based computer connected to a Pressure Systems Incorporated (PSI) data scanning system. The PSI system included a 780B Data Acquisition and Control Unit (DACU), 780B Pressure Calibration Unit (PCU), 81-IFC scanning module interface, two 2.5 psid pressure scanning modules (ESPs), one 20-in water column range pressure scanning module, and a 30 channel Remotely Addressed Millivolt Module (RAMM-30). Figure 7 shows the schematic of the data acquisition system.

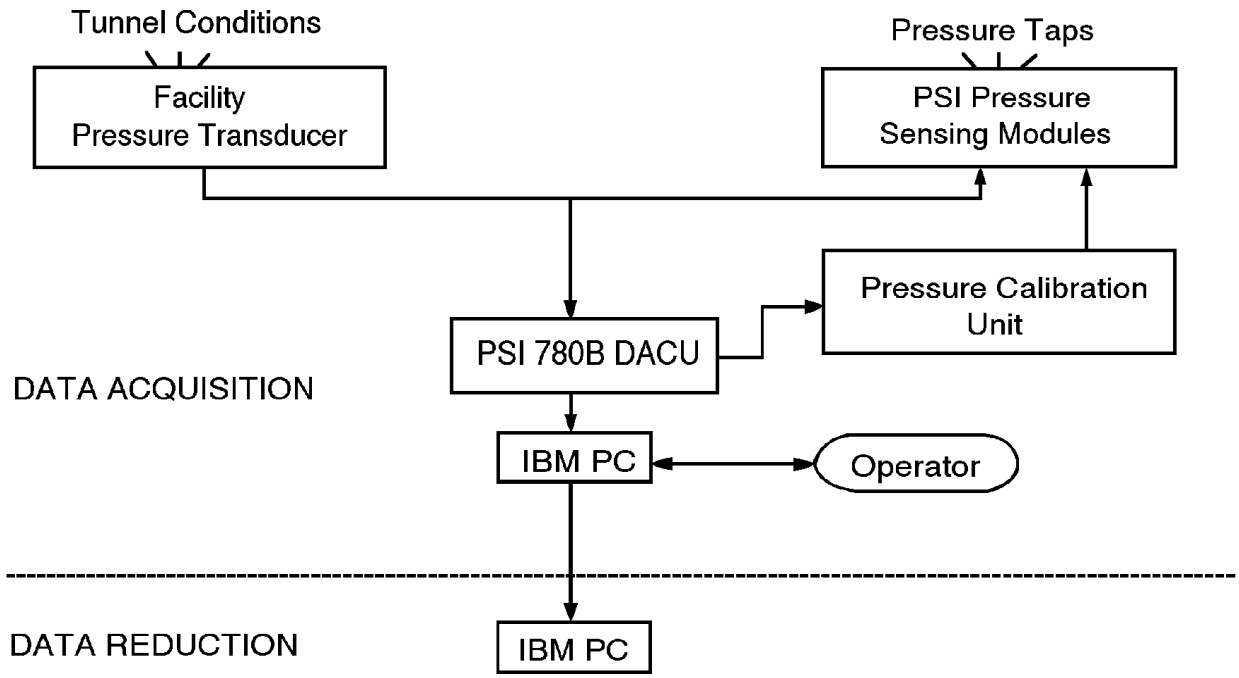

Figure 7. Data acquisition schematic.

Four individual pressure transducers read tunnel total pressure, tunnel north static pressure, tunnel south static pressure, and wake dynamic pressure. Before the test began, these transducers were bench calibrated using a water manometer to determine their sensitivities and offsets. Related values were entered into the data acquisition and reduction program so the transducers could be shunt resistor calibrated before each series of wind tunnel runs.

The rotary angle of attack potentiometer of 0.5% linearity was regularly calibrated during the tunnel pressure transducers shunt calibration. The angle of attack calibration was accomplished by taking voltage readings at known values of set angle of attack. This calibration method gave angle of attack readings within ±0.25° over the entire angle range. The wake probe position potentiometer was a linear potentiometer and it was also regularly calibrated during the shunt calibration of the tunnel pressure transducers.

Calibration of the three ESPs was done simultaneously by using the DACU and PCU. At operator request, the DACU commanded the PCU to apply known regulated pressures to the ESPs and read the output voltages from each integrated pressure sensor. From these values, the DACU calculated the calibration coefficients,

and stored them internally until the coefficients were requested by the controlling computer. This calibration was done several times during a run set because the ESPs were installed inside the model and their outputs tended to drift with temperature changes during a test sequence. Frequent on-line calibrations minimized the effect.

For steady state cases, the model was set to an angle of attack and the tunnel conditions adjusted. At operator request, pressure measurements from the airfoil surface taps and all other channels of information were acquired and stored by the DACU and subsequently passed to the controlling computer for final processing. The angles of attack were always set in the same progression - from 0° to -20° then from 0° to +40°.

For model oscillating cases, the tunnel conditions were set while the model was stationary at the desired mean angle of attack. The "shaker" was started, the model was allowed to oscillate through at least five cycles to establish the flow field, and then the model surface pressure and tunnel condition data were acquired. Generally, 120 data scans were acquired over three model oscillation cycles. Since surface pressures were scanned sequentially, the data rate was set so the model rotated through less than 0.50° during any data burst. Finally, due to the unsteady and complex nature of the pitch oscillation cases, model wake surveys (for drag) were not conducted.

Data Reduction

The data reduction routine was included as a section of the data acquisition program. This combination of data acquisition and reduction routines allowed data to be reduced on-line during a test. By quickly reducing selected runs, integrity checks could be made to insure the equipment was working properly and to allow timely decisions about the test matrix.

The ambient pressure was manually input into the computer and was updated regularly. This value, as well as the measurements from the tunnel pressure transducers and the tunnel thermocouple, were used to calculate tunnel airspeed. As a continuous check of readings, the tunnel total and static pressures were read by both the tunnel individual pressure transducers and the 20-inch water column ESP.

A typical steady state data point was derived by acquiring 10 data scans of all channels over a 10 second window at each angle of attack and tunnel condition. The reduction portion of the program processed each data scan to coefficient (C_p, C_l, $C_{m¼}$, and C_{dp}) using the measured surface pressure voltages, calibration coefficients, tap locations and wind tunnel conditions. Then, all scan sets for a given condition were ensemble averaged to provide one data set and that data set was then corrected for the effects of solid tunnel walls. All data was saved in electronic form.

Corrections due to solid tunnel sidewalls were applied to the wind tunnel data. As described by Pope and Harper (1966), tunnel conditions are represented by the following equations:

$$q = q_u(1 + 2\epsilon)$$

$$V = V_u(1 + \epsilon)$$

$$R_e = R_{e_u}(1 + \epsilon)$$

Airfoil aerodynamic characteristics are corrected by:

$$\alpha = \alpha_u + \frac{57.3\sigma}{2\pi}(C_{l_u} + 4C_{m\frac{1}{4}_u})$$

$$C_l = C_{l_u}(1 - \sigma - 2\epsilon)$$

$$C_{m_{\frac{1}{4}}} = C_{m_{\frac{1}{4}_u}}(1-2\epsilon) + \frac{\sigma\, C_l}{4}$$

$$C_d = C_{d_u}(1-3\epsilon_{sb}-2\epsilon_{wb})$$

where

$$\sigma = \frac{\pi^2}{48}\left(\frac{c}{h}\right)^2$$

$$\epsilon = \epsilon_{sb} + \epsilon_{wb}$$

$$\epsilon_{sb} = \Lambda\sigma$$

$$\epsilon_{wb} = \frac{c}{h4} C_{d_u}$$

Model wake data were taken for steady state cases when the wake could be completely traversed. Pressures were acquired from a pitot-static probe which was connected to measure incompressible dynamic pressure through the wake. These pressure measurements were used to calculate drag coefficient using a form of the Jones equation derived from Schlichting (1979).

$$C_{dw} = \frac{2}{c}\int \sqrt{\frac{q_w}{q_\infty}}\left(1-\sqrt{\frac{q_w}{q_\infty}}\right)\, dy$$

This usage assumes static pressure at the measurement site is the free-stream value. The integration was done automatically except the computer operator chose the end points of the integration from a plot of the wake survey displayed on the computer screen.

For pitch oscillation cases, model surface pressures were reduced to pressure coefficient form with subsequent integrations and angle of attack considerations giving lift, moment and pressure drag coefficients. There was no calibration available for unsteady model pitch conditions; therefore, the unsteady pressure data were not corrected for any possible effects due to time dependent pitching or solid tunnel walls. Also for these cases, the wind tunnel contraction pressures (used for steady state cases) could not be used to calculate instantaneous free stream conditions due to slow response. The tunnel conditions were obtained from a total pressure probe, and the average of opposing static taps in the test section entrance; thereby giving near instantaneous flow pressure conditions for the pitching frequencies used.

Test Matrix

The test was designed to study steady state and unsteady pitch oscillation data. Steady state data were acquired at Reynolds numbers of 0.75, 1, and 1.25 million with and without LEGR. Refer to the tabular data in Appendix B for the actual Reynolds number for each angle of attack for the steady state data. The angle of attack increment was two degrees when $-20° < \alpha < +10°$ or $+20° < \alpha < +40°$ ($+30°$ for the LEGR) and one degree when $+10° < \alpha < +20°$. Wake surveys were conducted to find total airfoil drag over an angle of attack range of $-10°$ to $+10°$ for clean and LEGR cases. The wake data was not taken for the Re=0.75 million case with LEGR applied since an accurate drag measurement was not possible due to the increased turbulence

from the grit. Unsteady data were taken for Reynolds numbers of 0.75, 1, and 1.25 million. Sine wave cams having amplitudes ±5.5° and ±10° were used for pitch oscillations, and the mean angles for both these amplitudes were 7°, 13°, and 19°. For all these conditions, the frequencies were varied to 0.6, 1.2, and 1.8 Hz. All data points for the unsteady cases were acquired for both clean and LEGR cases.

Results and Discussion

An L303 airfoil model was tested under steady state and pitch oscillation conditions. A brief discussion of a portion of the steady and unsteady results follows, including a comparison of steady experimental data and computational predictions.

Comparison With Theory

The wind tunnel steady state data were compared with the computed predictions made using the FUN2D program , a finite unstructured two dimensional Navier-Stokes solver. The North Carolina State Airfoil Analysis Code usually used for these comparisons could not be used since it cannot handle such a blunt trailing edge. FUN2D predicted the correct trend in both the lift and moment coefficients for the low angles of attack. The analysis code did estimate the lift coefficient in the range of -5° to 7° angle of attack quite accurately.

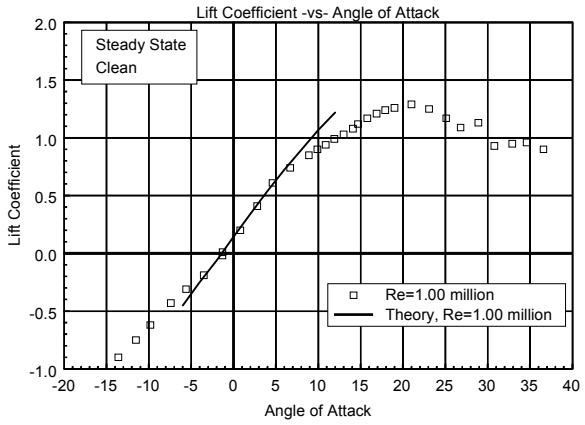

Figure 8. Comparison with theory, C_l vs α.

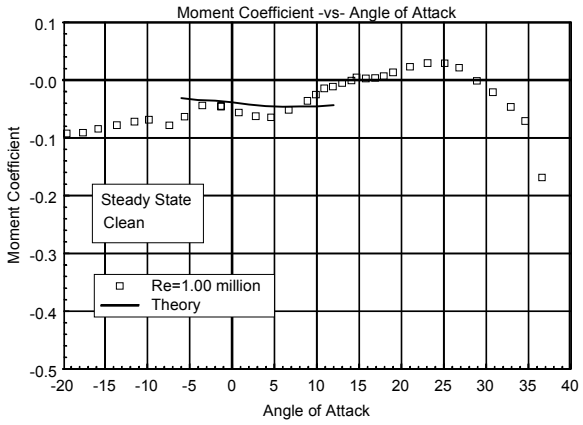

Figure 9. Comparison with theory, C_m vs α.

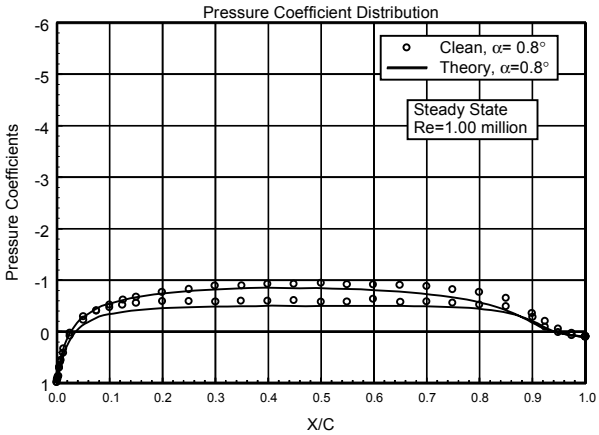

Figure 10. Comparison with theory, C_p vs x/c, α=0.8°.

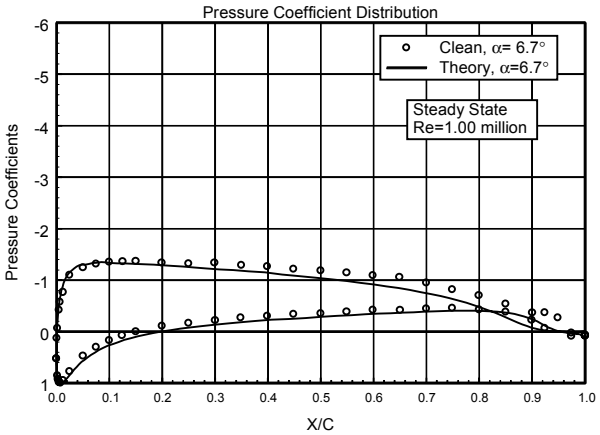

Figure 11. Comparison with theory, C_p vs x/c, α=6.7°.

Figure 8 shows the lift coefficient versus angle of attack for the 1 million Reynolds number case and for moderate angles of attack the comparison showed reasonable agreement. The pitching moment about the quarter chord, figure 9, showed adequate agreement for angles of attack from -4° to +7°. The pressure distributions shown in figures 10 and 11 are for angles of attack of 0.8° and 6.7°, respectively, and include clean wind tunnel data as compared to computed pressure distributions. For both angles of attack, there was good correlation between the clean experimental and predicted values.

Steady State Data

The L303 airfoil model was tested at three Reynolds numbers at nominal angles of attack from -20° to +40°. Figures 12 and 13 show lift coefficients for all the test Reynolds numbers both for model clean and with LEGR applied, respectively. The maximum positive lift coefficient, found at 1.00 million Reynolds number, was 1.29 for the clean cases and 0.84 for the LEGR cases, a 35% reduction due to the application of LEGR. The clean cases had positive stall near 21.0° while the LEGR cases stalled near 16.9° angle of attack. The average lift curve slope through the linear portion of the lift curve for clean data was 0.070 and about 0.058 for the LEGR case. The associated average lift coefficients at zero angle of attack were 0.14 for the clean case and -0.04 for the LEGR case.

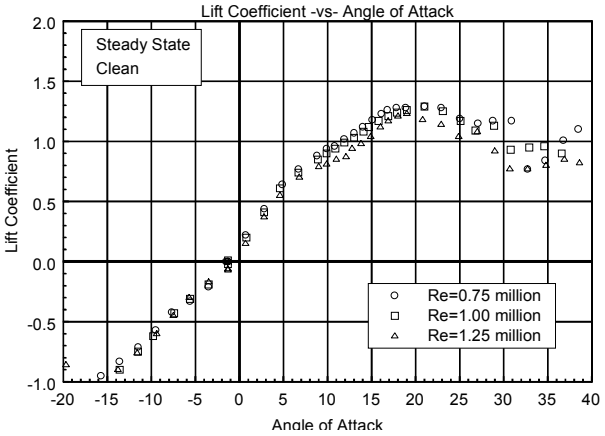

Figure 12. C_l vs α, clean.

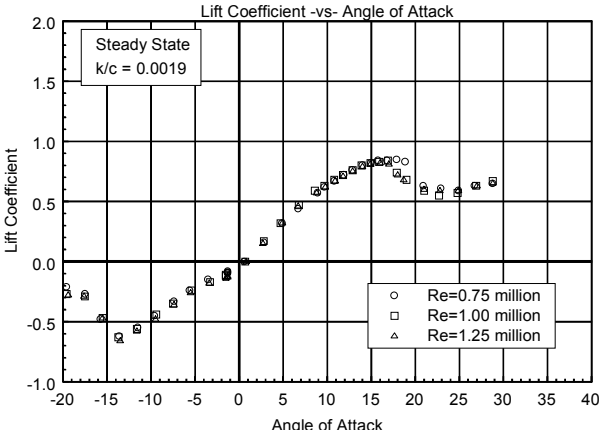

Figure 13. C_l vs α, LEGR, k/c=0.0019.

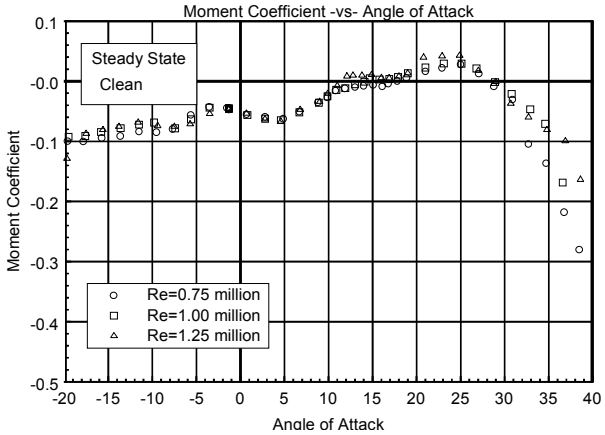

Figure 14. C_m vs α, clean.

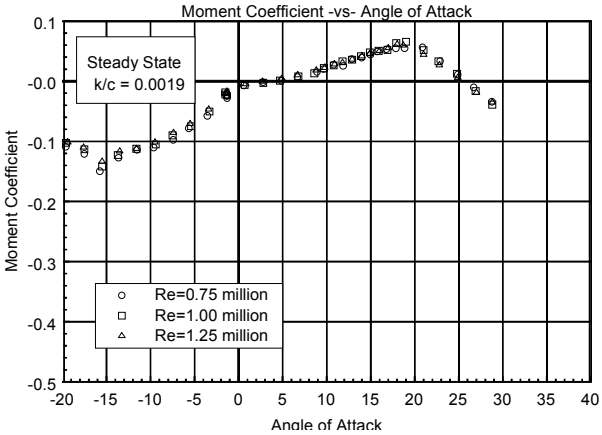

Figure 15. C_m vs α, LEGR, k/c=0.0019.

Figure 14 shows the pitching moment about the quarter chord for the clean cases and figure 15 shows the LEGR cases. The magnitude of the zero lift pitching moment was affected by the application of LEGR, there was over a 9% decrease in the zero lift pitching moment from the clean to the LEGR case throughout the range of Reynolds numbers tested. The zero lift pitching moment coefficient about the quarter chord for the 1 million Reynolds number was -0.0449 for the clean case and -0.0058 for the LEGR case. For moderate angles of attack 0° to +5° the pitching moment was nearly constant at 0.0 for the LEGR cases.

Wake drag data were obtained over an angle of attack range of -10° to 10°. Early testing of the airfoil showed that the wake was somewhat unsteady to the extent that the acquisition of suitable data for the drag

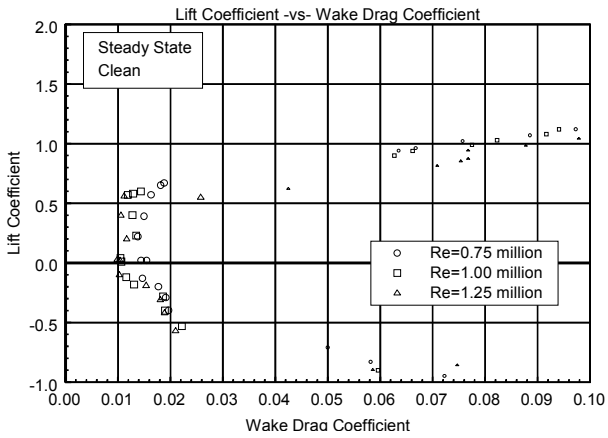

Figure 16. Clean, drag polar.

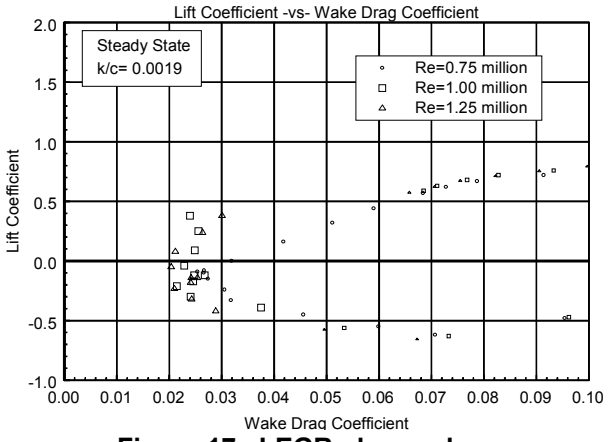

Figure 17. LEGR, drag polar.

calculation was not possible. This feature was not unexpected since it has been observed in wind tunnel tests on other airfoils having thick or blunt trailing edges. The source of the usteadiness has been speculated as originating with a vortex in the base region or a separated zone; the vortex periodically sheds and reverses rotation. A T-shaped flap was attached to the base for the purpose of establishing a symmetric vortex formation and the wake was stabilized over a moderate range of angles of attack.A series of tests was conducted to optimize the flap configuration, i.e. to enable the acquisition of realistic drag data with a minimum of interference on the pressure distribution (and, hence, lift and pitching moment), However, all of the reported pressure distributions, lifts and pitching moment coefficients were obtained without the trailing-edge flap. Since the drag was essentially unaltered for a series of changes in the length of the flap, it is concluded that the reported drags are truly representative for the clean airfoil. As might be expected, the onset of separation on the airfoil (as promoted by high angles of attack and/or excessive roughness) overrode the stabilizing influence of the flap with the result that wake based drag could not be obtained; as usual, the integrated pressure drag is used for such cases. A pitot-static probe was used to describe the wake profile. This method is reliable when there is relatively low turbulence in the wake flow; therefore, only moderate angles of attack have reliable total drag coefficient data. At angles of attack other than those where the wake data were acquired, surface pressure data were integrated to give C_{dp} and are shown in the drag polars as small symbols. The model clean drag data are shown in figure 13 and the LEGR case is shown in figure 15. At 1 million Reynolds number, minimum drag coefficient for the clean cases was measured as 0.0105, and 0.0215 for LEGR; a 105% increase. The general effect of LEGR was to increase drag consistently through most angles of attack.

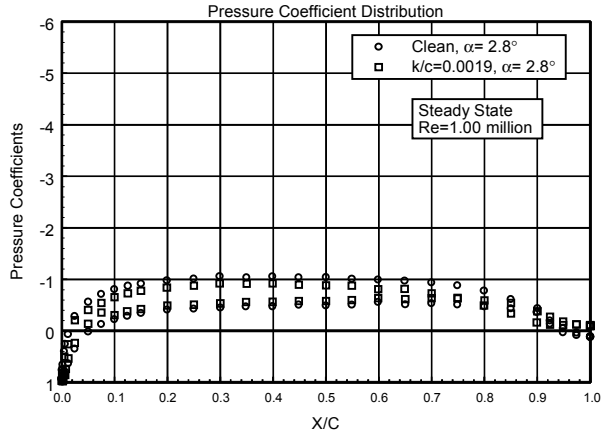

Figure 18. Pressure distribution, α=2.8°.

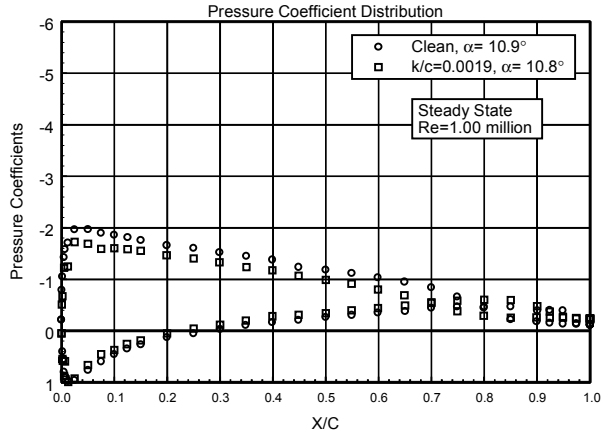

Figure 19. Pressure distribution, α=10.9°.

Two examples of the surface pressure distributions are shown in figures 18 and 19 for 2.8° and 10.9°, respectively, for 1 million Reynolds number. At angles of attack close to zero degrees, the effect of LEGR did not appear to significantly affect the pressure distribution in comparison with the clean case distribution; however, the effect was apparent in the lift coefficient where for the LEGR case it was 0.17 and 0.41 for the clean case at 2.8°. For the higher angle of attack case, figure 19, the effect of LEGR was to reduce the magnitude of the pressure peak from -2 to -1.8 and increase the pressures on the upper (suction) surface over the forward 70% of the chord. The net effect was a reduction in lift coefficient from 0.94 to 0.68, a 28% decrease.

Unsteady Data

Unsteady experimental data were obtained for the L303 airfoil model undergoing sinusoidal pitch oscillations. As mentioned earlier, no calibration was available for the unsteady oscillating model conditions; the steady state tunnel calibration was used to set the flow conditions while the model was stationary at its mean angle of attack. A comprehensive set of test conditions was used to describe unsteady behavior of the airfoil including: two angle of attack amplitudes, ±5.5° and ±10°; three Reynolds numbers, 0.75, 1, and 1.25 million; three pitch oscillation frequencies, 0.6, 1.2, and 1.8; and three mean angles of attack, 7°, 13°, and 19°.

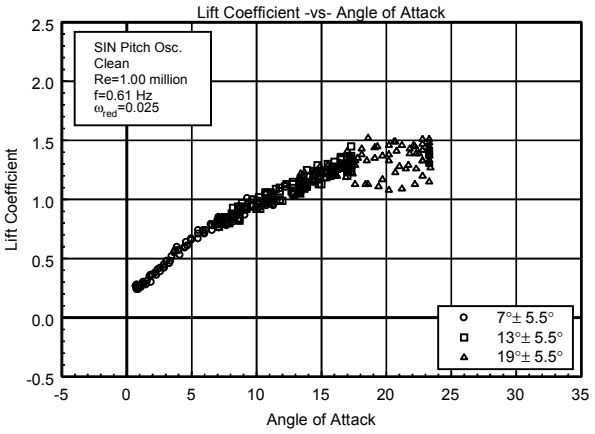

Figure 20. Clean, C_l vs α, ω_{red}=0.025, ±5.5°.

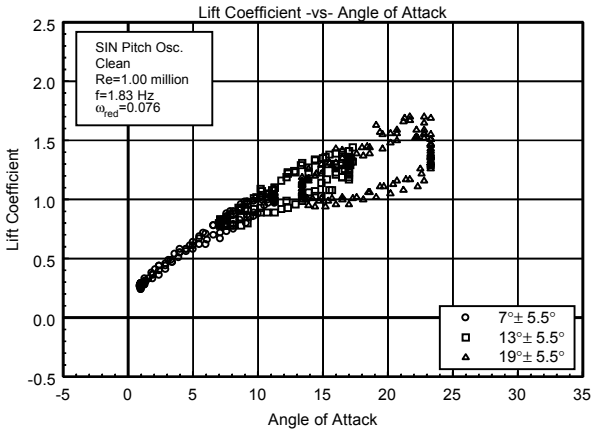

Figure 21. Clean, C_l vs α, ω_{red}=0.076, ±5.5°.

Figure 20 shows the lift coefficient versus angle of attack for the ±5.5° amplitude model clean case, at reduced frequency of 0.025 and 1 million Reynolds number. Note that all three mean angles of attack are plotted on the same figure. The maximum pre-stall lift coefficient for this case was near 1.49 and occurred when the airfoil was traveling with the angle of attack increasing. In contrast, when the model was traveling through decreasing angles of attack, the stall recovery was delayed and a hysteresis behavior was exhibited in the lift coefficient that can be seen throughout all of the unsteady data. In order to obtain some measure of this hysteresis behavior, the lift coefficient on the "return" portion of the curve, at the angle of attack where maximum lift coefficient occurs, can be used. For the case discussed here, the hysteresis lift coefficient was 1.23, a 18% decrease from the 1.49 unsteady maximum value. In comparison, the steady state maximum lift coefficient was 1.29. At higher reduced frequency of 0.076, the hysteresis behavior was more pronounced as seen in figure 21. In addition to greater hysteresis, the maximum lift coefficient was increased to about 1.70, which was a 32% increase over the steady state value. The corresponding hysteresis lift coefficient was 1.17. This difference between steady state behavior and unsteady hysteresis behavior demonstrates the need for unsteady testing of airfoils used in wind turbine applications.

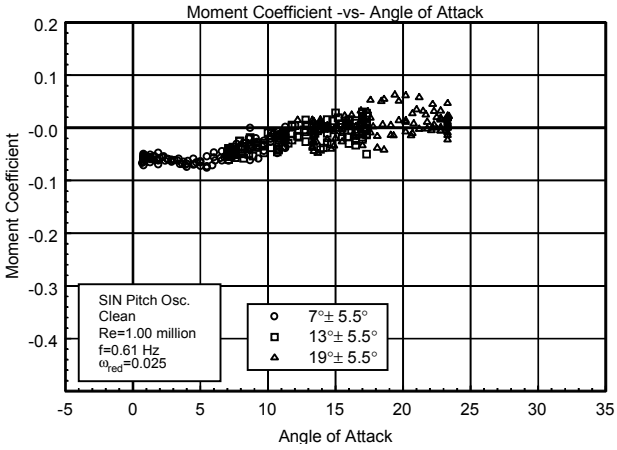

Figure 22. Clean, C_m vs α, ω_{red}=0.025, ±5.5°.

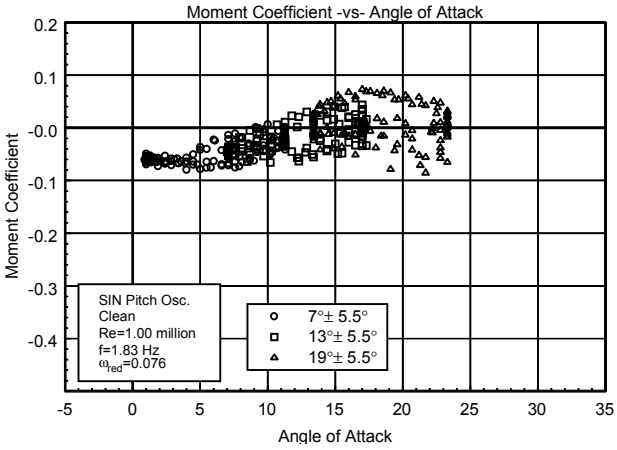

Figure 23. Clean, C_m vs α, ω_{red}=0.076, ±5.5°.

The pitching moment in figures 22 and 23 corresponds to the same conditions as the two lift coefficient plots previously discussed. There was an indication that the hysteresis behavior was present but it was not as apparent as in the lift coefficient plots; but the higher reduced frequency case did show hysteresis more than the lower reduced frequency case. For reference, the steady state maximum lift occurred near 21° angle of attack and the steady state pitching moment at this maximum lift point was 0.0230. In comparison, when the airfoil was undergoing pitch oscillation for the lower frequency, pitching moment varied from -0.0142 to 0.0274 (at the angle of attack where maximum lift occurred). At the higher frequency, shown in figure 23, the pitching moment where maximum lift coefficient occurred was in the range of -0.0852 to 0.0426. For most cases the pitching moment coefficient was fairly close to zero. Note the angle of attack where the maximum lift coefficient occurred does not necessarily show the "greatest" hysteresis behavior but does give a relative indication of the effect.

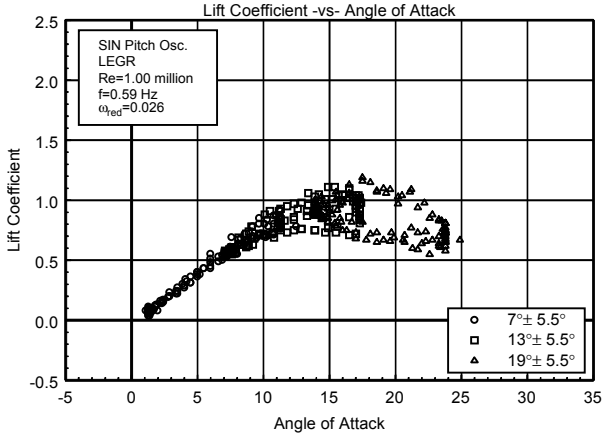

Figure 24. LEGR, C_l vs α, ω_{red}=0.026, ±5.5°.

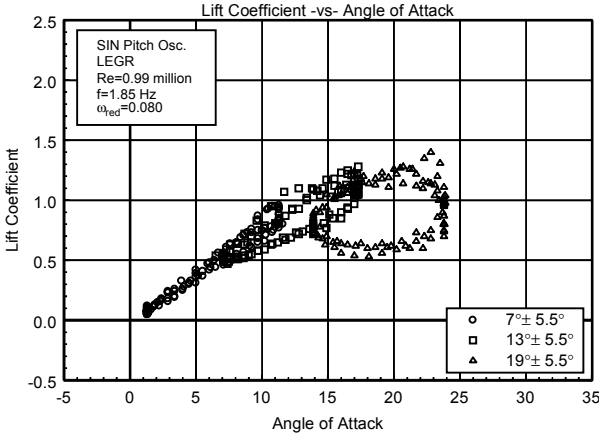

Figure 25. LEGR, C_l vs α, ω_{red}=0.080, ±5.5°.

In comparison to the clean data, the application of LEGR reduced the maximum lift coefficient in the pitch oscillation cases. Lift coefficient versus angle of attack with LEGR applied is shown in figure 24 for the 0.026 reduced frequency case. The 0.080 reduced frequency case is in figure 25. Both correspond to the same run conditions which were described earlier for the clean cases. For the lower reduced frequency, the maximum unsteady lift coefficient was reduced to 1.19 from the corresponding clean case of 1.49, a 20% decrease. Hysteresis behavior was apparent at this frequency but it was of slightly larger order than the clean case; the corresponding hysteresis lift coefficient was 0.82 when LEGR was applied. In contrast, the higher frequency LEGR case had a maximum lift coefficient of 1.28 while the model was increasing in angle of

attack and the corresponding decreasing angle of attack lift coefficient was 1.10. Again, the application of LEGR slightly changed the hysteresis loop behavior for larger angles of attack in comparison with the clean case.

The pitching moment coefficient shown in figure 26 is for 0.026 reduced frequency with LEGR applied. At the angle of unsteady maximum lift, the pitching moment ranges from 0.0065 to 0.0613, while the steady state LEGR pitching moment is 0.0523 at the steady state stall angle of attack (16.9°). The higher reduced frequency of 0.080 with LEGR application is shown in figure 27. As was seen with the lift coefficient, pitching moment hysteresis is more apparent at the higher reduced frequency than the corresponding low reduced frequency case. Unsteady maximum lift angle of attack for this reduced frequency occurs at 17.3° and the pitching moment ranges from -0.0267 to 0.0280 at that angle. Throughout the higher angle of attack range, the magnitude of the unsteady pitching moment can be very different than the steady state clean case (clean steady state pitching moment at maximum lift is 0.0230). These differences may have an impact on the fatigue life predictions of a wind turbine system.

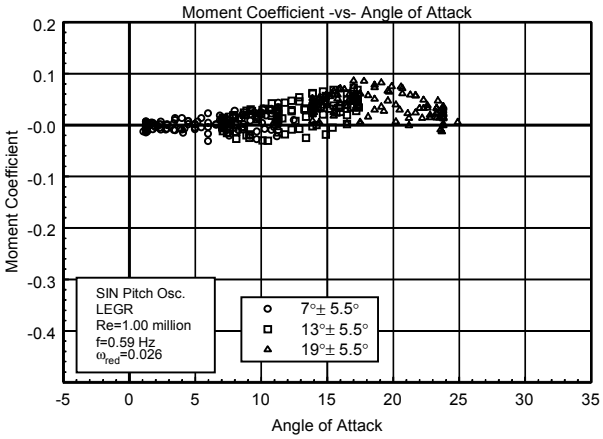

Figure 26. LEGR, C_m vs α, ω_{red}=0.026, ±5.5°.

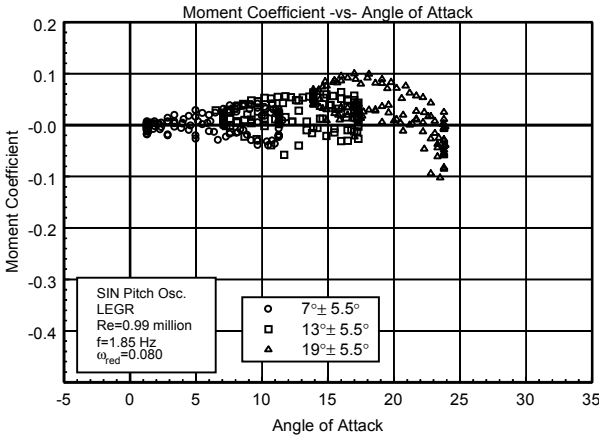

Figure 27. LEGR, C_m vs α, ω_{red}=0.080,±5.5°.

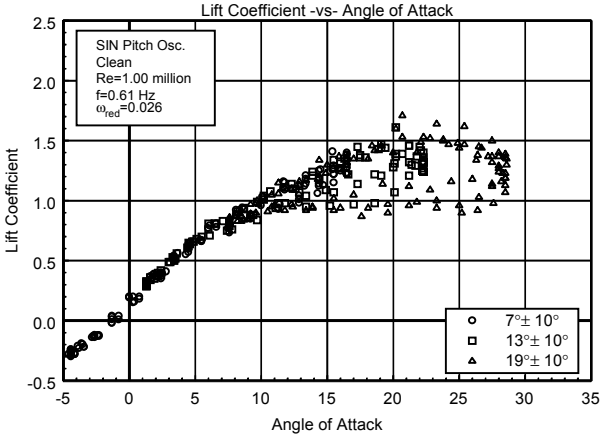

Figure 28. Clean, C_l vs α, ω_{red}=0.026, ±10°.

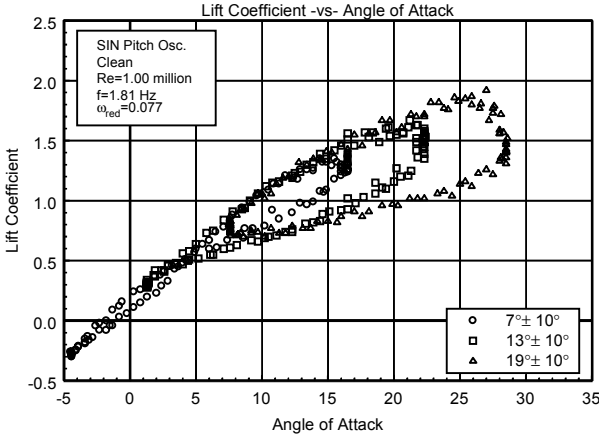

Figure 29. Clean, C_l vs α, ω_{red}=0.077, ±10°.

In addition to the ±5.5° unsteady experimental data, ±10° unsteady data were obtained with and without LEGR. The data shown were taken at 1 million Reynolds number using the same mean angles and frequencies as the 5.5° amplitude cases. Figures 28 and 29 show the ±10°, unsteady, clean, lift coefficient for the reduced frequencies of 0.026 and 0.077, respectively. The maximum lift coefficient for the lower frequency is 1.61 and occurs, as expected, when the airfoil is traveling through increasing angle of attack.

The hysteresis lift coefficient (at 20.2°) is 1.07. At the higher reduced frequency, the maximum lift coefficient occurs at a higher angle of attack, 25.9°, and is 1.87. The corresponding hysteresis lift coefficient is 1.12. The difference between the maximum lift coefficient and the hysteresis lift coefficient indicates a much greater hysteresis response than experienced for the lower reduced frequency. The steady state, clean, maximum lift coefficient is 1.29; therefore, the unsteady behavior created lift coefficients up to 45% higher than the steady state values under these conditions.

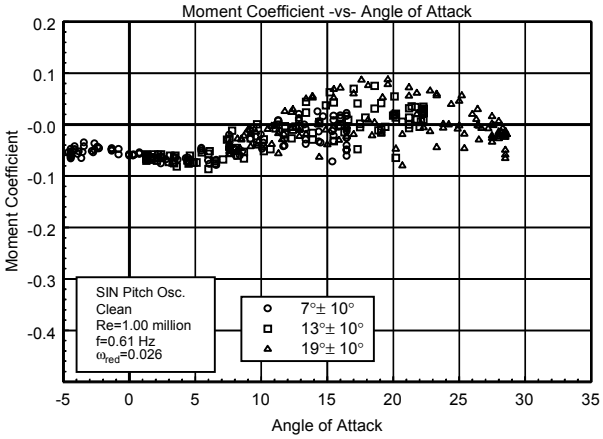

Figure 30. Clean, C_m vs α, ω_{red}=0.026, ±10°.

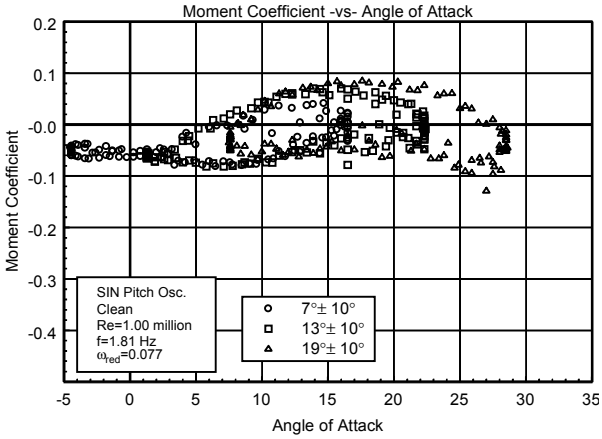

Figure 31. Clean, C_m vs α, ω_{red}=0.077, ±10°.

The quarter chord pitching moments having the same reduced frequencies as the lift coefficient cases are shown in figures 30 and 31. The hysteresis behavior observed in the lift coefficient plots is also reflected in this pitching moment data. Near the maximum lift angle, 20.2° for the lower frequency, the pitching moment coefficient ranged from -0.0644 to 0.0548; whereas the 0.077 reduced frequency case had maximum lift near 25.9° and pitching moment ranged from -0.0939 to 0.0311. In comparison, the steady state pitching moment was 0.0230 near the steady state maximum lift coefficient angle of attack of 21.0°. The higher reduced frequency again showed large hysteresis loops for all three mean angles of attack.

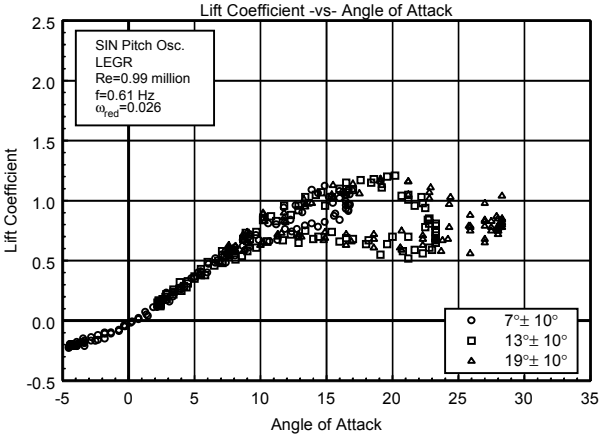

Figure 32. LEGR, C_l vs α, ω_{red}=0.026, ±10°.

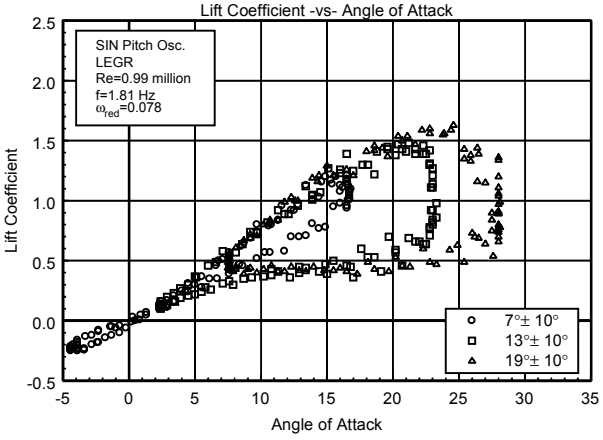

Figure 33. LEGR, C_l vs α, ω_{red}=0.078, ±10°.

The application of LEGR degraded the lift performance of the airfoil as would be expected from the results discussed previously. The LEGR lift coefficient data for reduced frequencies of 0.026 and 0.078 are shown in figures 32 and 33, respectively. The maximum lift coefficient was reduced to 1.21 from 1.61 for the low frequency clean case. Although there was a reduction, this value was still higher than the LEGR steady state case which had a maximum lift coefficient of 0.84 at 16.9° angle of attack. The higher reduced frequency

had a maximum lift coefficient of 1.63 which occurred near 25° angle of attack. The corresponding lift coefficient at 24.6° for the airfoil traveling with decreasing angle of attack was 0.63, a 61% reduction from the maximum.

Figures 34 and 35 show the corresponding pitching moment coefficients for the reduced frequencies of 0.026 and 0.078. For the 0.026 reduced frequency case, the pitching moment varied from 0.0016 to 0.0682 at 20.2° (where the maximum lift occurred). The hysteresis behavior was more pronounced for the higher reduced frequency case, where the range of pitching moments at the maximum lift angle of 24.6° was from -0.1381 to 0.0210. These values can then be compared to the steady state LEGR value of 0.0523.

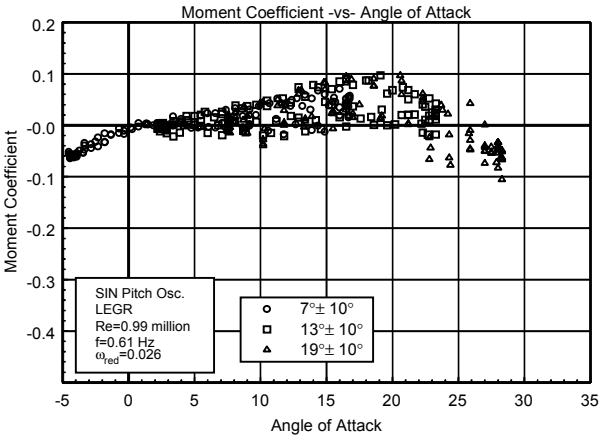

Figure 34. LEGR, C_m vs α, ω_{red}=0.026, ±10°.

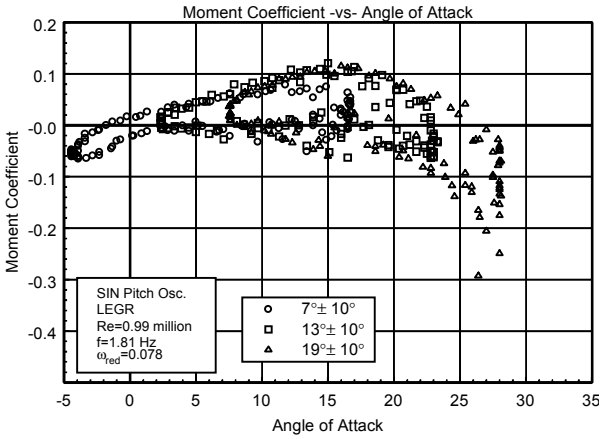

Figure 35. LEGR, C_m vs α, ω_{red}=0.078, ±10°.

Although all the unsteady data were not discussed here, the previous discussion included typical examples of the wind tunnel data. The remaining cases of the ±5.5° and ±10° oscillation data for all the Reynolds numbers are included in Appendix C.

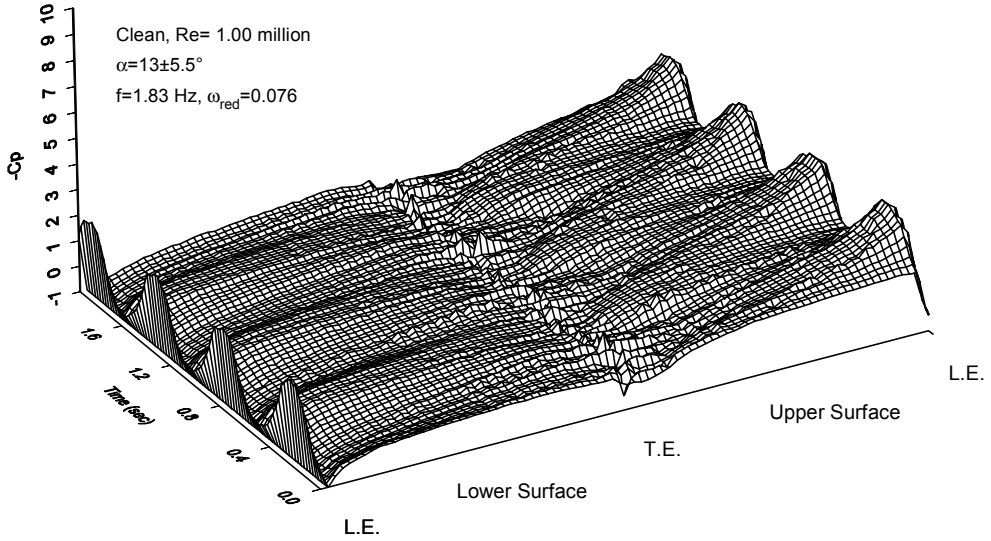

Figure 36. Unsteady pressure distribution, clean, ω_{red}=0.076, 13±5.5°.

The unsteady pressure distributions show examples of the data used to calculate the lift, pressure drag, and the pitching moment coefficients. Figure 36 shows the distribution for a clean model, with a reduced

frequency of 0.076, a mean angle of attack of 13°, and a ±5.5° pitch oscillation. For plotting clarity, the model pressures were "unwrapped" about the trailing edge. The upper surface pressures are depicted on the right of the surface plot, lower surface values on the left. The trailing edge is then at the midpoint of the x-axis with the leading edge at each extreme. The time scale corresponds to angle of attack. For this case, the negative pressure peak was at approximately -3.5. Figure 37 shows the LEGR case for the same test conditions as the previous figure. The application of LEGR reduced the pressure peak only slightly. Separated flow is defined as the irregular, "rough" areas on the upper surface. Also note that the lower surface stayed attached through the airfoil travel.

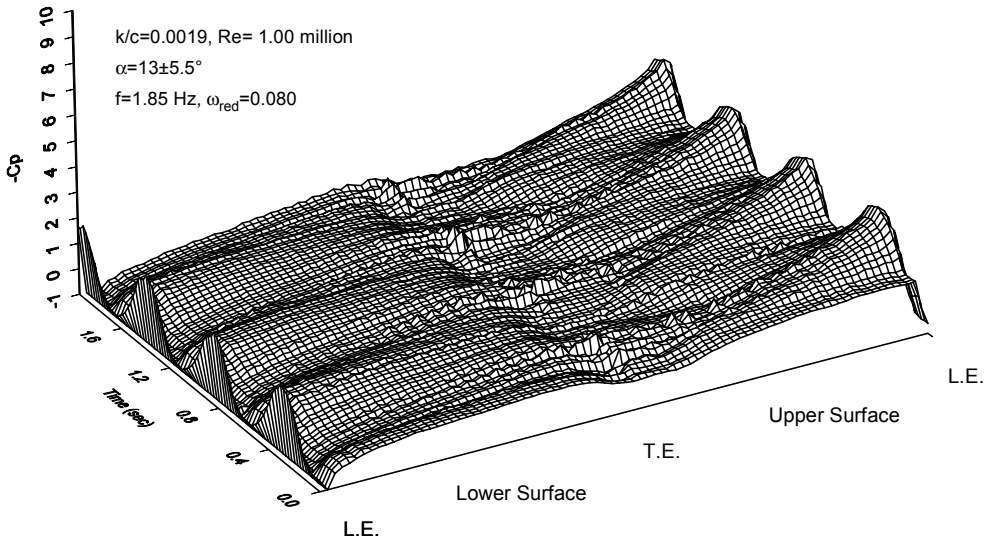

Figure 37. Unsteady pressure distribution, LEGR, ω_{red}=0.080, 13±5.5°.

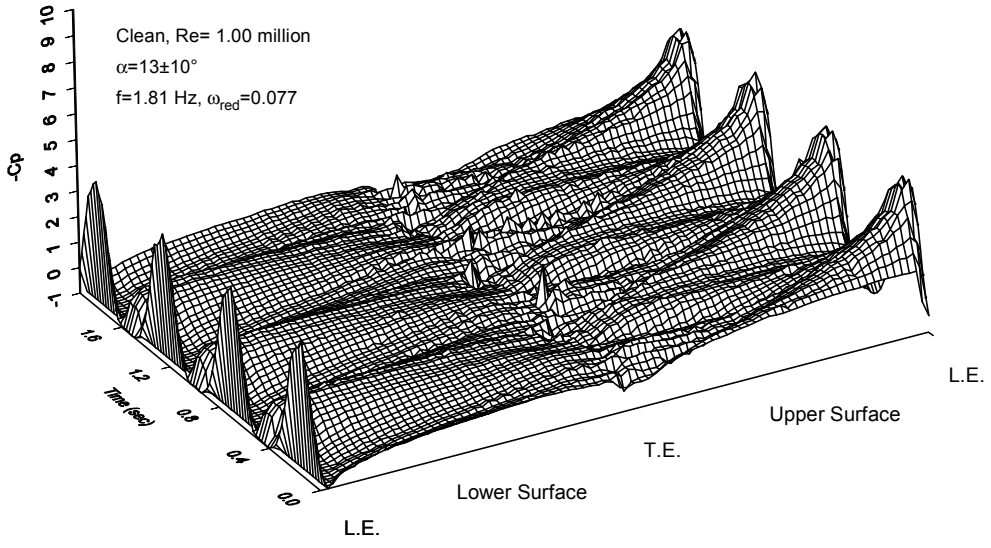

Figure 38. Unsteady pressure distribution, clean, ω_{red}=0.077, 13±10°.

Figure 38 shows the same clean run conditions as above except with the ±10° amplitude oscillation. This case was characterized by significant portions of the upper surface in stall and high pressure peaks. The negative pressure coefficient peaks were about -5.0 for this case while it was near -3.5 for the previous clean,

13° mean angle of attack case. The secondary peaks apparent on the upper surface correspond to a region of partial stall recovery while the model was traveling through decreasing angle of attack.

Summary of Results

An L303 airfoil model was tested under steady state and pitch oscillation conditions. Baseline tests were made while the model was clean, and then corresponding tests were conducted with leading edge grit roughness (LEGR) applied.

A summary of the steady state aerodynamic parameters is shown in table 1. As observed, the application of LEGR reduced the maximum lift of the airfoil 35% and the minimum drag coefficient increased by 11%. The magnitude of the zero lift pitching moment coefficient was reduced 9% by application of LEGR.

Table 1. L303 Steady State Parameters Summary

Grit Pattern	Re x 10^{-6}	C_{lmax}	C_{dmin}	C_{mo}
Clean	0.75	1.28 @ 17.8°	0.0139	-0.0471
k/c=0.0019	0.75	0.84 @ 15.8°	--	-0.0074
Clean	1.00	1.29 @ 21.0	0.0105	-0.0449
k/c=0.0019	1.00	0.84 @ 16.9°	0.0215	-0.0058
Clean	1.25	1.23 @ 19.0°	0.0099	-0.0463
k/c=0.0019	1.25	0.82 @ 16.0°	0.0204	-0.0042

The pitch oscillation data can be divided into two groups, the ±5.5° amplitude and ±10° amplitude oscillations which show similar trends. For both ±5.5° and ±10°, the unsteady test conditions and some parameters are in listed tables 2, 3, 4, and 5. Looking at the reduced frequency, which takes oscillation and tunnel speed into account, as this value increased, the maximum lift coefficient also increased. The increase in maximum lift coefficient with reduced frequency was nearly linear for the cases tested as shown in figures 39 and 40. In addition, the hysteresis behavior became increasingly apparent with increased reduced frequency.

Table 2. L303, Unsteady, Clean, ±5.5°

ω_{red}	Re x 10^{-6}	f	C_{lmax}	α_{max}	$C_{l\,dec}$	$C_{m\,inc}$	$C_{m\,dec}$
0.033	0.76	0.60	1.52	19.7	1.29	-0.0502	0.0333
0.067	0.76	1.21	1.68	19.6	1.13	-0.0821	0.0524
0.101	0.76	1.83	1.81	22.2	1.26	-0.0997	0.0301
0.025	1.00	0.61	1.49	20.6	1.23	-0.0142	0.0274
0.050	1.00	1.19	1.64	20.7	1.19	-0.0746	0.0469
0.076	1.00	1.83	1.70	21.7	1.17	-0.0852	0.0426
0.020	1.25	0.60	1.44	19.1	0.98	-0.0123	0.0622
0.041	1.25	1.21	1.46	18.6	0.93	-0.0306	0.0649
0.062	1.25	1.85	1.52	20.2	1.17	-0.0233	0.0370

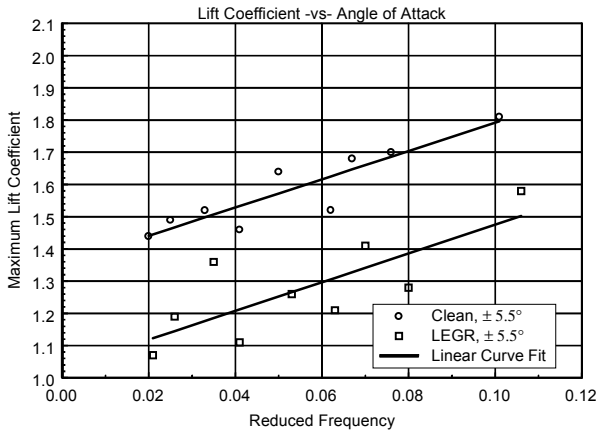

Figure 39. ±5.5°, unsteady C_{lmax} vs ω_{red}.

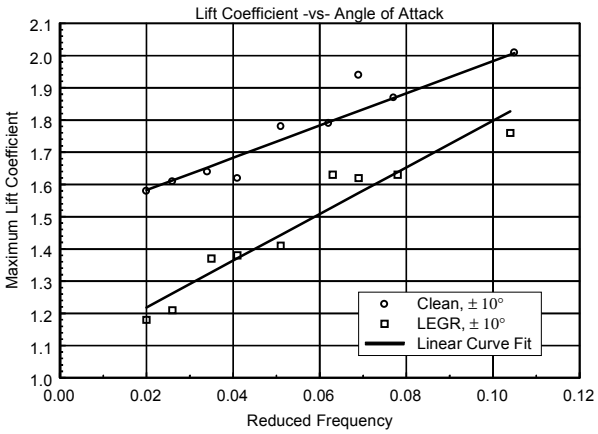

Figure 40. ±10°, unsteady C_{lmax} vs ω_{red}.

Table 3. L303, Unsteady, LEGR, ±5.5°

ω_{red}	Re x 10^{-6}	f	C_{lmax}	α_{max}	$C_{l\,dec}$	$C_{m\,inc}$	$C_{m\,dec}$
0.035	0.75	0.61	1.36	18.6	0.62	-0.0322	0.0859
0.070	0.74	1.21	1.41	19.7	0.70	-0.0251	0.0848
0.106	0.74	1.83	1.58	20.7	0.52	-0.0724	0.0644
0.026	1.00	0.59	1.19	17.5	0.82	0.0065	0.0613
0.053	1.00	1.22	1.26	15.7	0.90	-0.0289	0.0470
0.080	0.99	1.85	1.28	17.3	1.10	-0.0267	0.0280
0.021	1.25	0.61	1.07	15.5	0.78	0.0276	0.0654
0.041	1.25	1.19	1.11	14.7	0.83	-0.0095	0.0520
0.063	1.25	1.83	1.21	16.0	0.89	-0.0227	0.0519

Table 4. L303, Unsteady, Clean, ±10°

ω_{red}	Re x 10^{-6}	f	C_{lmax}	α_{max}	$C_{l\,dec}$	$C_{m\,inc}$	$C_{m\,dec}$
0.034	0.75	0.60	1.64	19.1	1.22	-0.0837	0.0293
0.069	0.76	1.22	1.94	24.9	1.13	-0.0895	0.0350
0.105	0.75	1.85	2.01	25.9	1.19	-0.0920	0.0196
0.026	1.00	0.61	1.61	20.2	1.07	-0.0644	0.0548
0.051	1.00	1.19	1.78	25.0	1.17	-0.0825	0.0242
0.077	1.00	1.81	1.87	25.9	1.12	-0.0939	0.0311
0.020	1.24	0.60	1.58	20.5	0.92	0.0013	0.0723
0.041	1.24	1.19	1.62	24.4	0.82	-0.0208	0.0304
0.062	1.25	1.83	1.79	23.9	1.08	-0.0601	0.0487

As expected, the application of LEGR reduced the aerodynamic performance of the airfoil. The unsteady maximum lift coefficient was reduced beteween 9% and 26% for both the ±5.5° case and the ±10° case with the application of LEGR. As well as following the same trends as the clean, unsteady data discussed

previously, the LEGR caused the hysteresis behavior to persist into lower angles of attack than did the clean cases. Overall, the unsteady wind tunnel data showed hysteresis behavior that became more apparent with increased, reduced frequency. The maximum unsteady lift coefficients could be up to 88% higher for the ±5.5° amplitude and up to 110% higher for the ±10° amplitude than the steady state maximum lift coefficients. In addition, variation in the quarter chord pitching moment coefficient was slight with the pitching moment coefficient close to zero. These findings indicate that it is very important to consider the unsteady loading that will occur in wind turbine operation because use of steady state results can greatly underestimate the forces.

Table 5. L303, Unsteady, LEGR, ±10°

ω_{red}	Re x 10^{-6}	ω	C_{lmax}	α_{max}	$C_{l\,dec}$	$C_{m\,inc}$	$C_{m\,dec}$
0.035	0.74	0.61	1.37	19.6	0.49	-0.0249	0.1045
0.069	0.74	1.18	1.62	20.7	0.61	-0.0719	0.0415
0.104	0.74	1.79	1.76	24.9	0.68	-0.1252	0.0022
0.026	0.99	0.61	1.21	20.2	0.70	0.0016	0.0682
0.051	1.00	1.18	1.41	21.2	0.54	-0.0496	0.0692
0.078	0.99	1.81	1.63	24.6	0.63	-0.1381	0.0210
0.020	1.25	0.60	1.18	18.5	0.69	0.0042	0.0752
0.041	1.24	1.21	1.38	20.0	0.60	-0.0387	0.0603
0.063	1.24	1.83	1.63	22.3	0.53	-0.1041	0.0573

References

Pope, A.; Harper, J.J. 1966. *Low Speed Wind Tunnel Testing*. New York, NY: John Wiley & Sons, Inc.

Schlichting, H. 1979. *Boundary Layer Theory*. New York, NY: McGraw-Hill Inc.

Smetana, F., Summey, D. et-al. 1975. *Light Aircraft Lift, Drag, and Moment Prediction - a Review and Analysis*. North Carolina State University. NASA CR-2523.

FUN2D (Finite Unstructured Two Dimensional Navier Stokes Code) provided by NASA-Langley

Appendix A: Model and Surface Pressure Tap Coordinates

List Of Tables Page

Table A1. L303 Measured Model Coordinates, 18 inch desired chord				
Chord Station (in)	Upper Ordinate (in)		Chord Station (in)	Lower Ordinate (in)
0.000000	0.005000		0.000000	0.005000
0.004179	0.057311		0.004350	-0.038970
0.008042	0.089272		0.009469	-0.070332
0.013800	0.123559		0.014263	-0.094873
0.015864	0.134234		0.019162	-0.117024
0.019615	0.152366		0.024232	-0.139216
0.023546	0.170077		0.028949	-0.157866
0.028995	0.191884		0.033631	-0.174917
0.032768	0.206406		0.038264	-0.190968
0.038342	0.225363		0.043148	-0.206999
0.043953	0.243391		0.048023	-0.222240
0.047133	0.252443		0.052702	-0.236001
0.052983	0.269900		0.057441	-0.249621
0.056273	0.278533		0.062103	-0.262002
0.062450	0.295069		0.067113	-0.275153
0.066614	0.305319		0.071786	-0.286824
0.071792	0.317647		0.076421	-0.297785
0.077703	0.331604		0.081136	-0.308755
0.081190	0.339046		0.085892	-0.319556
0.084697	0.346348		0.090659	-0.329717
0.090224	0.358326		0.095664	-0.340479
0.095851	0.370023		0.100312	-0.350019
0.099026	0.376656		0.105230	-0.359910
0.105625	0.389461		0.110307	-0.370122
0.111401	0.400658		0.115214	-0.379903
0.114373	0.406251		0.119636	-0.387963

Table A1. L303 Measured Model Coordinates, 18 inch desired chord				
Chord Station (in)	Upper Ordinate (in)		Chord Station (in)	Lower Ordinate (in)
0.120700	0.418056		0.124724	-0.397545
0.124596	0.425018		0.129465	-0.406036
0.128552	0.431979		0.134574	-0.415407
0.134416	0.442375		0.139096	-0.423108
0.140560	0.452991		0.144206	-0.432059
0.144164	0.459073		0.148709	-0.439560
0.148149	0.465934		0.153690	-0.447611
0.153771	0.475281		0.158861	-0.456163
0.160014	0.485357		0.163255	-0.463093
0.163657	0.491339		0.167900	-0.469843
0.168203	0.498298		0.173519	-0.478826
0.173502	0.506837		0.177576	-0.484705
0.177477	0.513107		0.182819	-0.492347
0.183708	0.522543		0.187643	-0.499328
0.186358	0.526807		0.192368	-0.505959
0.192137	0.534994		0.197601	-0.513271
0.196994	0.542643		0.202614	-0.520602
0.201178	0.548884		0.206593	-0.525622
0.207068	0.557430		0.212006	-0.532924
0.212646	0.565608		0.216324	-0.538354
0.216489	0.570969		0.221708	-0.545356
0.222618	0.579715		0.226275	-0.551146
0.226460	0.584916		0.323576	-0.660598
0.335201	0.721329		0.421736	-0.753002
0.433327	0.825086		0.520626	-0.836447
0.532138	0.917741		0.619357	-0.911272

Table A1. L303 Measured Model Coordinates, 18 inch desired chord				
Chord Station (in)	Upper Ordinate (in)		Chord Station (in)	Lower Ordinate (in)
0.631501	1.002176		0.718013	-0.978777
0.730778	1.079720		0.817113	-1.040622
0.830161	1.151604		0.916152	-1.098148
0.929605	1.219058		1.114030	-1.200268
1.128619	1.343315		1.312665	-1.290460
1.327856	1.456112		1.511707	-1.373274
1.527153	1.560059		1.710747	-1.448287
1.726651	1.655765		1.910021	-1.517231
1.926234	1.744701		2.109554	-1.582055
2.125805	1.828207		2.309019	-1.641649
2.325653	1.906223		2.508574	-1.696703
2.525420	1.979808		2.708267	-1.748408
2.725108	2.048684		2.907778	-1.796402
2.925096	2.113419		3.107438	-1.840716
3.124995	2.174695		3.307374	-1.882171
3.324919	2.233089		3.507275	-1.921346
3.524985	2.288274		3.707042	-1.958221
3.724905	2.340490		3.906885	-1.992496
3.924968	2.390124		4.106802	-2.024481
4.125046	2.437369		4.306814	-2.054586
4.324919	2.482215		4.506860	-2.083201
4.524956	2.524659		4.706779	-2.110116
4.724987	2.564514		4.906712	-2.135432
4.924803	2.602290		5.106688	-2.159157
5.124995	2.637954		5.306747	-2.181892
5.325073	2.671739		5.506849	-2.203317

Table A1. L303 Measured Model Coordinates, 18 inch desired chord				
Chord Station (in)	Upper Ordinate (in)		Chord Station (in)	Lower Ordinate (in)
5.524663	2.702815		5.706943	-2.223653
5.724881	2.732009		5.906742	-2.242077
5.924973	2.759284		6.106934	-2.259113
6.124741	2.784490		6.306909	-2.274528
6.324825	2.807784		6.506837	-2.288883
6.524704	2.829200		6.707119	-2.301509
6.724768	2.848584		6.907113	-2.313364
6.924880	2.866229		7.107090	-2.323609
7.124786	2.882214		7.307469	-2.332825
7.324849	2.896349		7.507431	-2.340890
7.525048	2.908763		7.707605	-2.347946
7.724932	2.919408		7.907743	-2.353711
7.925043	2.928313		8.107852	-2.358437
8.124991	2.935928		8.307954	-2.362262
8.324906	2.942103		8.508249	-2.365058
8.524985	2.946537		8.708294	-2.367003
8.725233	2.949572		8.908382	-2.368088
8.925058	2.951217		9.108673	-2.368044
9.125389	2.951462		9.308726	-2.367140
9.325287	2.950277		9.508931	-2.365255
9.525171	2.947562		9.709318	-2.362341
9.725441	2.943206		9.909228	-2.358396
9.925199	2.937251		10.109539	-2.353382
10.125061	2.929636		10.309844	-2.347368
10.325091	2.920331		10.509930	-2.340223
10.524906	2.909257		10.710340	-2.331919

Table A1. L303 Measured Model Coordinates, 18 inch desired chord				
Chord Station (in)	Upper Ordinate (in)		Chord Station (in)	Lower Ordinate (in)
10.724927	2.896311		10.910772	-2.322705
10.925055	2.881586		11.110956	-2.312421
11.124957	2.865121		11.311452	-2.300827
11.324857	2.846836		11.511642	-2.288082
11.524951	2.826621		11.711884	-2.273888
11.724831	2.804576		11.912371	-2.258324
11.924967	2.780550		12.112539	-2.241500
12.124928	2.754435		12.312872	-2.223176
12.324905	2.726470		12.513297	-2.203262
12.524938	2.696525		12.713437	-2.181707
12.724964	2.664359		12.913690	-2.158543
12.924877	2.630124		13.114037	-2.133838
13.124975	2.593669		13.314277	-2.107474
13.325068	2.554983		13.514441	-2.079459
13.524795	2.514109		13.714869	-2.049806
13.724817	2.471174		13.915071	-2.018371
13.924886	2.426098		14.115328	-1.984837
14.124819	2.378653		14.315470	-1.949052
14.324824	2.328558		14.515528	-1.910877
14.524725	2.275803		14.715840	-1.870263
14.724390	2.220368		14.915760	-1.827128
14.924267	2.161823		15.115834	-1.781183
15.123956	2.099719		15.316027	-1.732198
15.323626	2.033554		15.515766	-1.679673
15.523126	1.963240		15.715556	-1.623097
15.722697	1.888385		15.915606	-1.562063

Table A1. L303 Measured Model Coordinates, 18 inch desired chord				
Chord Station (in)	Upper Ordinate (in)		Chord Station (in)	Lower Ordinate (in)
15.922116	1.808661		16.115374	-1.496607
16.121721	1.723767		16.315493	-1.427222
16.321609	1.633872		16.515726	-1.355108
16.520916	1.540618		16.716295	-1.281474
16.721352	1.445022		16.916893	-1.207970
16.921392	1.349176		17.117828	-1.135837
17.121531	1.255381		17.318918	-1.066305
17.322451	1.163353		17.519669	-0.999711
17.522718	1.073727		17.720760	-0.933789
17.723305	0.984820		17.920994	-0.870094
17.920057	0.897823		17.925709	-0.868655
17.924864	0.895671		17.931171	-0.866987
17.930017	0.893420		17.935797	-0.865558
17.934963	0.891178		17.940487	-0.864069
17.939909	0.888967		17.945591	-0.862440
17.944742	0.886786		17.950485	-0.860851
17.949726	0.884515		17.955318	-0.859302
17.954302	0.882415		17.960285	-0.857694
17.959187	0.880163			
17.964113	0.877822			
17.968828	0.875581			
End of Table A1				

Table A2. L303 Surface Pressure Taps, Non-Dimensional Coordinates		
Tap Number	Chord Station	Ordinate
1	1.0000	0.0000
2	1.0000	-0.0333
3	0.9743	-0.0573
4	0.9490	-0.0659
5	0.9244	-0.0749
6	0.8995	-0.0839
7	0.8495	-0.0987
8	0.7997	-0.1096
9	0.7495	-0.1180
10	0..6995	-0.1241
11	0.6495	-0.1287
12	0.5993	-0.1317
13	0.5492	-0.1334
14	0.4995	-0.1339
15	0.4491	-0.1334
16	0.3993	-0.1317
17	0.3494	-0.1287
18	0.2997	-0.1240
19	0.2496	-0.1179
20	0.1996	-0.1099
21	0.1497	-0.0992
22	0.1244	-0.0924
23	0.0996	-0.0844
24	0.0747	-0.0747
25	0.0504	-0.0630
26	0.0253	-0.0456
27	0.0126	-0.0328
28	0.0080	-0.0255
29	0.0055	-0.0210
30	0.0026	-0.0135
31	0.0015	-0.0096
32	0.0000	0.0014

Table A2. L303 Surface Pressure Taps, Non-Dimensional Coordinates		
Tap Number	Chord Station	Ordinate
33	0.0008	0.0093
34	0.0018	0.0136
35	0.0048	0.0217
36	0.0074	0.0265
37	0.0122	0.0341
38	0.0249	0.0490
39	0.0497	0.0686
40	0.0750	0.0838
41	0.0998	0.0960
42	0.1246	0.1064
43	0.1497	0.1155
44	0.1992	0.1301
45	0.2496	0.1419
46	0.2992	0.1511
47	0.3495	0.1579
48	0.3993	0.1625
49	0.4494	0.1652
50	0.4995	0.1661
51	0.5493	0.1653
52	0.5993	0.1628
53	0.6492	0.1582
54	0.6997	0.1515
55	0.7493	0.1423
56	0.7993	0.1306
57	0.8495	0.1157
58	0.8992	0.0965
59	0.9236	0.0853
60	0.9493	0.0729
61	0.9740	0.0618
62	1.0000	0.0333
End of Table A2		

Appendix B: Steady State Data
Integrated Coefficients and Pressure Distributions

List of Figures Page

List of Tables Page

Table B1. L303, Clean, Re=0.75 x 10^6						
Run	AOA	C_l	C_{dp}	$C_{m¼}$	Rex10^{-6}	C_{dw}
49	-21.5	-1.03	0.1603	-0.1013	0.75	—
48	-19.6	-1.05	0.1228	-0.0997	0.75	—
47	-17.8	-1.04	0.0916	-0.1002	0.75	—
46	-15.7	-0.95	0.0723	-0.0946	0.75	—
45	-13.6	-0.83	0.0582	-0.0916	0.75	—
44	-11.5	-0.71	0.0500	-0.0840	0.75	—
43	-9.5	-0.57	0.0365	-0.0850	0.75	0.0197
42	-7.7	-0.42	0.0282	-0.0798	0.75	0.0192
41	-5.6	-0.33	0.0222	-0.0560	0.76	0.0178
40	-3.5	-0.21	0.0204	-0.0432	0.75	0.0147
50	-1.5	0.00	0.0235	-0.0444	0.74	0.0145
39	-1.3	0.00	0.0271	-0.0471	0.75	0.0155
76	-1.3	0.00	0.0233	-0.0446	0.75	—
51	0.7	0.22	0.0277	-0.0549	0.75	0.0139
52	2.8	0.44	0.0303	-0.0594	0.75	0.0150
53	4.9	0.64	0.0362	-0.0629	0.75	0.0164
54	6.7	0.77	0.0383	-0.0509	0.76	0.0182
55	8.8	0.88	0.0574	-0.0352	0.75	0.0189
56	9.9	0.94	0.0636	-0.0270	0.75	—
57	10.8	0.96	0.0668	-0.0155	0.75	—
58	11.9	1.02	0.0758	-0.0122	0.75	—
59	13.0	1.07	0.0886	-0.0099	0.75	—
60	14.0	1.12	0.0973	-0.0078	0.75	—
61	15.1	1.18	0.1067	-0.0061	0.75	—
62	16.1	1.23	0.1232	-0.0086	0.75	—
63	16.8	1.26	0.1259	-0.0044	0.75	—
64	17.8	1.28	0.1389	0.0001	0.74	—
65	18.9	1.28	0.1537	0.0055	0.75	—

Table B1. L303, Clean, Re=0.75 x 10^6						
Run	AOA	C_l	C_{dp}	$C_{m¼}$	Rex10^{-6}	C_{dw}
66	21.0	1.29	0.1761	0.0163	0.75	—
67	22.9	1.28	0.1978	0.0219	0.74	—
68	25.0	1.19	0.2190	0.0280	0.73	—
69	27.1	1.15	0.2832	0.0125	0.72	—
70	28.8	1.17	0.3346	-0.0086	0.72	—
71	30.9	1.17	0.3951	-0.0307	0.72	—
72	32.7	0.77	0.7094	-0.1045	0.72	—
73	34.7	0.84	0.8077	-0.1363	0.72	—
74	36.8	1.01	1.0118	-0.2182	0.75	—
75	38.5	1.10	1.1483	-0.2800	0.75	—
End of Table B1						

Table B2. L303, Clean, Re=1.00 x 10^6						
Run	AOA	C_l	C_{dp}	$C_{m¼}$	Rex10^{-6}	C_{dw}
87	-21.6	-0.84	0.1061	-0.1211	0.99	—
86	-19.5	-1.08	0.1169	-0.0922	0.99	—
85	-17.6	-1.08	0.0828	-0.0908	0.99	—
84	-15.8	-1.01	0.0711	-0.0844	1.00	—
83	-13.6	-0.90	0.0596	-0.0778	1.00	—
82	-11.5	-0.75	0.0497	-0.0720	1.01	0.0222
81	-9.8	-0.62	0.0423	-0.0686	1.00	0.0190
80	-7.4	-0.43	0.0264	-0.0781	1.01	0.0186
79	-5.6	-0.31	0.0230	-0.0633	1.00	0.0131
78	-3.5	-0.19	0.0177	-0.0439	1.00	0.0116
77	-1.3	0.01	0.0259	-0.0457	1.00	0.0105
88	-1.3	-0.02	0.0245	-0.0449	1.01	0.0107
89	0.8	0.20	0.0275	-0.0561	1.01	0.0135
90	2.8	0.41	0.0303	-0.0622	1.00	0.0128
91	4.6	0.61	0.0318	-0.0645	1.01	0.0119
92	6.7	0.74	0.0410	-0.0516	1.00	—
93	8.9	0.85	0.0585	-0.0358	1.02	—
94	9.9	0.90	0.0627	-0.0248	1.00	—
95	10.9	0.94	0.0662	-0.0144	1.01	—
96	11.9	0.99	0.0775	-0.0113	1.01	—
97	13.0	1.03	0.0823	-0.0048	1.02	—
98	14.1	1.08	0.0917	-0.0007	1.02	—
99	14.7	1.12	0.0941	0.0049	1.01	—
100	15.8	1.17	0.1107	0.0028	1.00	—
101	16.9	1.21	0.1250	0.0038	1.00	—
102	17.9	1.24	0.1372	0.0071	1.01	—
103	19.0	1.26	0.1452	0.0135	1.02	—
104	21.0	1.29	0.1623	0.0230	1.02	—

Table B2. L303, Clean, Re=1.00 x 10^6						
Run	AOA	C_l	C_{dp}	$C_{m¼}$	Rex10^{-6}	C_{dw}
105	23.1	1.25	0.1714	0.0294	1.02	—
106	25.1	1.17	0.1987	0.0293	1.01	—
107	26.8	1.09	0.2285	0.0213	1.01	—
108	28.9	1.13	0.3039	-0.0012	1.01	—
109	30.8	0.93	0.3333	-0.0208	1.03	—
110	32.9	0.95	0.4052	-0.0464	1.01	—
111	34.6	0.96	0.4745	-0.0707	1.02	—
112	36.6	0.90	0.9013	-0.1686	1.09	—
End of Table B2						

Table B3. L303, Clean, Re=1.25 x 10^6						
Run	AOA	C_l	C_{dp}	$C_{m¼}$	Rex10^{-6}	C_{dw}
11	-21.4	-0.60	0.1470	-0.0913	1.23	—
10	-19.7	-0.86	0.0747	-0.1286	1.24	—
9	-17.5	-1.09	0.0840	-0.0867	1.25	—
8	-15.6	-1.02	0.0676	-0.0805	1.25	—
7	-13.8	-0.90	0.0586	-0.0753	1.25	—
6	-11.6	-0.76	0.0494	-0.0682	1.26	0.0210
5	-9.4	-0.60	0.0392	-0.0738	1.26	0.0189
4	-7.5	-0.45	0.0282	-0.0752	1.26	0.0181
3	-5.7	-0.30	0.0211	-0.0706	1.26	0.0154
2	-3.5	-0.17	0.0185	-0.0539	1.26	0.0103
1	-1.3	0.00	0.0247	-0.0463	1.25	0.0104
12	-1.3	-0.07	0.0213	-0.0446	1.26	0.0099
38	-1.3	-0.06	0.0226	-0.0457	1.26	—
13	0.7	0.15	0.0272	-0.0532	1.26	0.0117
14	2.8	0.37	0.0313	-0.0626	1.26	0.0106
15	4.6	0.55	0.0364	-0.0667	1.25	0.0112
16	6.8	0.70	0.0425	-0.0469	1.25	0.0258
17	9.0	0.79	0.0648	-0.0338	1.25	—
18	9.9	0.81	0.0709	-0.0202	1.26	—
19	11.0	0.85	0.0754	-0.0071	1.26	—
20	12.1	0.87	0.0768	0.0086	1.25	—
21	12.8	0.94	0.0768	0.0099	1.25	—
22	13.8	0.98	0.0878	0.0102	1.25	—
23	14.9	1.04	0.0979	0.0110	1.25	—
24	16.0	1.12	0.1140	0.0061	1.25	—
25	16.9	1.17	0.1251	0.0056	1.24	—
26	18.0	1.21	0.1371	0.0085	1.24	—
27	19.0	1.23	0.1481	0.0137	1.24	—

Table B3. L303, Clean, Re=1.25 x 10^6						
Run	AOA	C_l	C_{dp}	$C_{m¼}$	Rex10^{-6}	C_{dw}
28	20.8	1.18	0.1361	0.0401	1.25	—
29	22.9	1.14	0.1681	0.0423	1.26	—
30	24.9	1.04	0.1814	0.0432	1.25	—
31	27.0	1.08	0.2622	0.0179	1.23	—
32	29.0	0.92	0.2977	-0.0007	1.23	—
33	30.7	0.77	0.3784	-0.0367	1.22	—
34	32.7	0.77	0.4477	-0.0594	1.21	—
35	34.8	0.80	0.5177	-0.0804	1.22	—
36	36.9	0.85	0.5891	-0.0993	1.20	—
37	38.6	0.82	0.8743	-0.1632	1.23	—
End of Table B3						

Table B4. L303, k/c = 0.0019, Re=0.75 x 10^6						
Run	AOA	C_l	C_{dp}	$C_{m¼}$	Rex10^{-6}	C_{dw}
167	-21.4	-0.31	0.2864	-0.0891	0.75	—
166	-19.6	-0.21	0.2197	-0.1094	0.75	—
165	-17.5	-0.27	0.1737	-0.1214	0.76	—
164	-15.7	-0.48	0.0954	-0.1500	0.74	—
163	-13.6	-0.62	0.0707	-0.1272	0.76	—
162	-11.5	-0.55	0.0599	-0.1144	0.76	—
161	-9.6	-0.45	0.0456	-0.1107	0.75	—
160	-7.4	-0.33	0.0318	-0.0977	0.75	—
159	-5.6	-0.24	0.0306	-0.0786	0.75	—
158	-3.5	-0.15	0.0274	-0.0580	0.75	—
157	-1.3	-0.10	0.0266	-0.0285	0.75	—
168	-1.3	-0.08	0.0267	-0.0235	0.75	—
189	-1.3	-0.09	0.0254	-0.0249	0.74	—
169	0.6	0.00	0.0319	-0.0074	0.75	—
170	2.8	0.16	0.0418	-0.0017	0.75	—
171	4.9	0.32	0.0511	0.0006	0.75	—
172	6.7	0.44	0.0590	0.0065	0.75	—
173	8.9	0.57	0.0684	0.0152	0.75	—
174	9.7	0.62	0.0728	0.0202	0.75	—
175	10.8	0.67	0.0787	0.0270	0.77	—
176	11.9	0.72	0.0914	0.0255	0.75	—
177	12.9	0.76	0.1029	0.0363	0.75	—
178	14.0	0.80	0.1093	0.0389	0.76	—
179	15.0	0.82	0.1199	0.0438	0.75	—
180	15.8	0.84	0.1265	0.0492	0.75	—
181	16.8	0.84	0.1392	0.0529	0.75	—
182	17.9	0.85	0.1534	0.0544	0.75	—
183	18.9	0.83	0.1661	0.0546	0.75	—

Table B4. L303, k/c = 0.0019, Re=0.75 x 10^6						
Run	AOA	C_l	C_{dp}	$C_{m¼}$	Rex10^{-6}	C_{dw}
184	20.9	0.63	0.1969	0.0558	0.75	—
185	22.9	0.61	0.2590	0.0331	0.74	—
186	24.9	0.59	0.3276	0.0109	0.74	—
187	26.7	0.63	0.3939	-0.0105	0.73	—
188	28.8	0.65	0.4692	-0.0346	0.74	—
End of Table B4						

Table B5. L303, k/c = 0.0019, Re=1.00 x 10^6						
Run	AOA	C_l	C_{dp}	$C_{m¼}$	Rex10^{-6}	C_{dw}
200	-21.4	-0.33	0.2851	-0.0784	1.02	—
199	-19.6	-0.27	0.2218	-0.1024	1.03	—
198	-17.5	-0.29	0.1750	-0.1132	1.00	—
197	-15.5	-0.47	0.0962	-0.1418	1.00	—
196	-13.7	-0.63	0.0733	-0.1225	1.00	—
195	-11.6	-0.56	0.0534	-0.1121	1.02	—
194	-9.4	-0.44	0.0390	-0.1050	1.00	0.0375
193	-7.5	-0.35	0.0345	-0.0898	1.01	0.0241
192	-5.4	-0.24	0.0303	-0.0748	1.01	0.0215
191	-3.3	-0.17	0.0280	-0.0500	1.00	0.0246
190	-1.5	-0.11	0.0310	-0.0181	1.00	0.0248
201	-1.5	-0.12	0.0299	-0.0221	0.99	0.0268
222	-1.5	-0.11	0.0309	-0.0184	1.01	—
202	0.7	0.00	0.0355	-0.0058	1.00	0.0229
203	2.8	0.17	0.0454	-0.0025	1.00	0.0249
204	4.7	0.32	0.0503	0.0013	1.00	0.0256
205	6.8	0.47	0.0586	0.0083	1.00	0.0240
206	8.6	0.59	0.0685	0.0135	1.00	—
207	9.7	0.63	0.0711	0.0219	1.01	—
208	10.8	0.68	0.0768	0.0263	1.00	—
209	11.8	0.72	0.0828	0.0334	1.00	—
210	12.9	0.76	0.0933	0.0359	0.99	—
211	13.9	0.80	0.1011	0.0418	1.00	—
212	14.9	0.82	0.1089	0.0483	1.00	—
213	15.9	0.83	0.1211	0.0505	1.00	—
214	16.9	0.84	0.1310	0.0523	0.98	—
215	17.9	0.74	0.1398	0.0638	0.98	—
216	19.0	0.68	0.1547	0.0658	0.98	—

Table B5. L303, k/c = 0.0019, Re=1.00 x 10^6						
Run	AOA	C_l	C_{dp}	$C_{m¼}$	Rex10^{-6}	C_{dw}
217	21.0	0.59	0.2040	0.0521	0.99	—
218	22.7	0.55	0.2612	0.0334	0.98	—
219	24.8	0.57	0.3295	0.0124	0.98	—
220	26.9	0.63	0.4119	-0.0161	0.98	—
221	28.8	0.67	0.4806	-0.0389	0.98	—
End of Table B5						

Table B6. L303, k/c = 0.0019, Re=1.25 x 10^6						
Run	AOA	C_l	C_{dp}	$C_{m¼}$	Rex10^{-6}	C_{dw}
233	-21.5	-0.33	0.2960	-0.0761	1.30	—
232	-19.4	-0.28	0.2228	-0.1010	1.28	—
231	-17.6	-0.29	0.1791	-0.1098	1.26	—
230	-15.5	-0.47	0.1010	-0.1331	1.27	—
229	-13.5	-0.66	0.0673	-0.1162	1.25	—
228	-11.6	-0.58	0.0496	-0.1120	1.25	—
227	-9.5	-0.48	0.0372	-0.1014	1.25	0.0289
226	-7.4	-0.36	0.0330	-0.0852	1.25	0.0243
225	-5.5	-0.26	0.0307	-0.0703	1.25	0.0210
224	-3.4	-0.18	0.0285	-0.0464	1.25	0.0241
255	-1.5	-0.14	0.0269	-0.0197	1.26	0.0254
223	-1.3	-0.12	0.0310	-0.0165	1.25	0.0242
234	-1.3	-0.13	0.0303	-0.0192	1.27	—
235	0.8	0.00	0.0357	-0.0042	1.26	0.0204
236	2.7	0.15	0.0436	-0.0003	1.26	0.0212
237	4.9	0.32	0.0498	0.0046	1.25	0.0264
238	6.7	0.46	0.0562	0.0108	1.26	0.0301
239	8.8	0.57	0.0658	0.0187	1.26	—
240	9.8	0.62	0.0706	0.0231	1.26	—
241	10.9	0.67	0.0755	0.0288	1.26	—
242	11.8	0.71	0.0822	0.0313	1.26	—
243	12.9	0.75	0.0906	0.0364	1.26	—
244	14.0	0.79	0.0997	0.0421	1.25	—
245	14.9	0.81	0.1071	0.0460	1.28	—
246	16.0	0.82	0.1166	0.0512	1.28	—
247	17.0	0.81	0.1273	0.0560	1.28	—
248	18.0	0.72	0.1379	0.0618	1.28	—
249	18.7	0.68	0.1519	0.0601	1.27	—

Table B6. L303, k/c = 0.0019, Re=1.25 x 10^6						
Run	AOA	C_l	C_{dp}	$C_{m¼}$	Rex10^{-6}	C_{dw}
250	21.0	0.60	0.2088	0.0449	1.26	—
251	22.8	0.59	0.2667	0.0274	1.27	—
252	24.9	0.59	0.3364	0.0064	1.28	—
253	27.0	0.63	0.4161	-0.0187	1.26	—
254	28.8	0.65	0.4761	-0.0346	1.29	—
End of Table B6						

L303

Pressure Distributions, Steady State, Re = 0.75 million

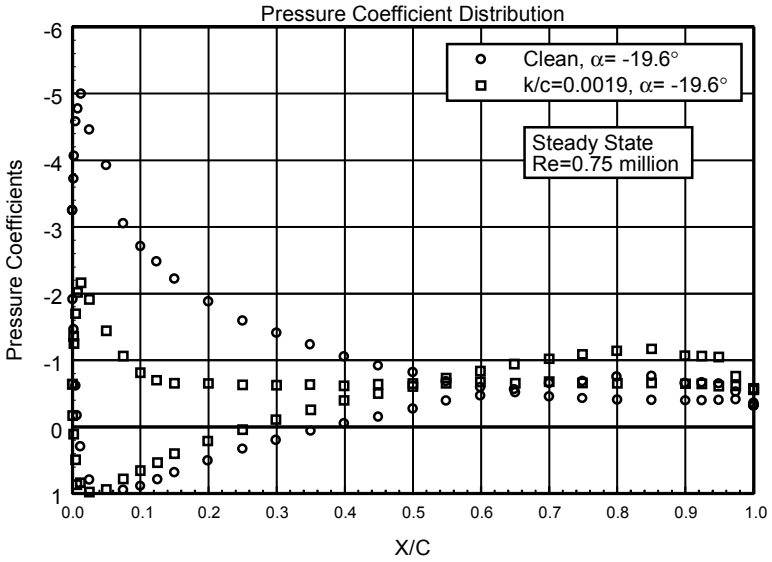

Figure 1. α = -19.6°

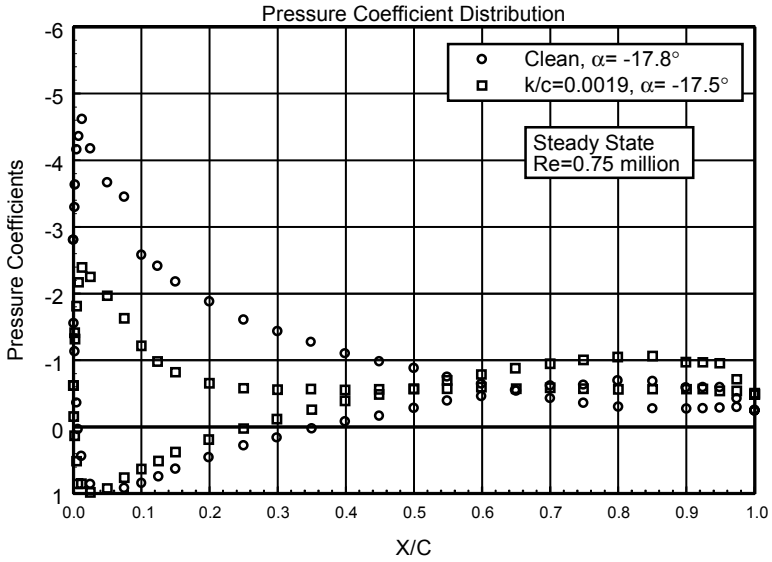

Figure 2. α = -17.8°

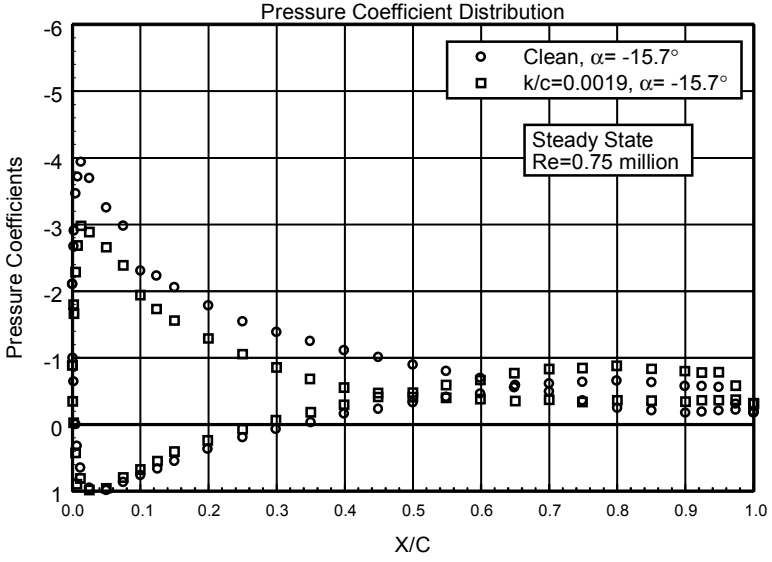

Figure 3. α = -15.7°

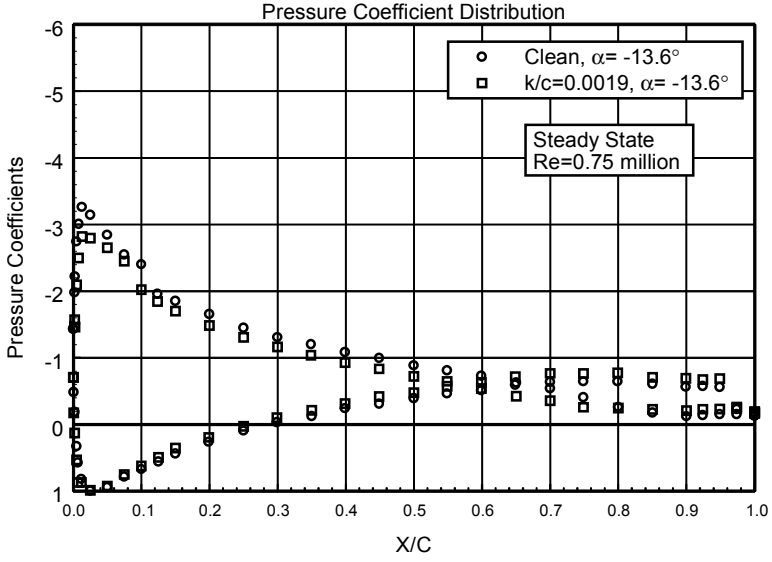

Figure 4. α = -13.6°

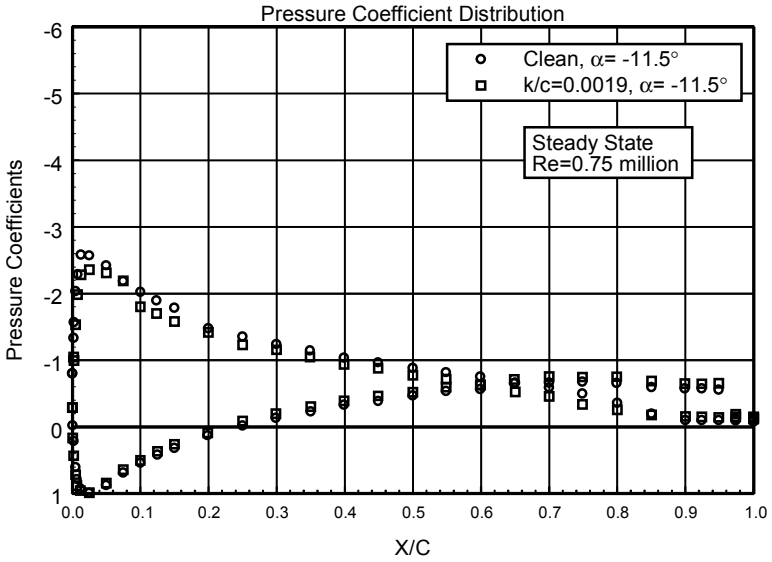

Figure 5. α = -11.5°

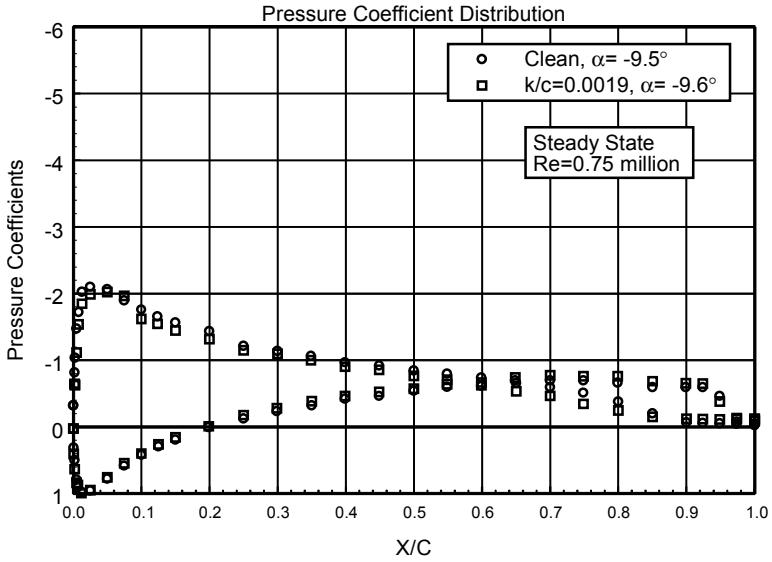

Figure 6. α = -9.5°

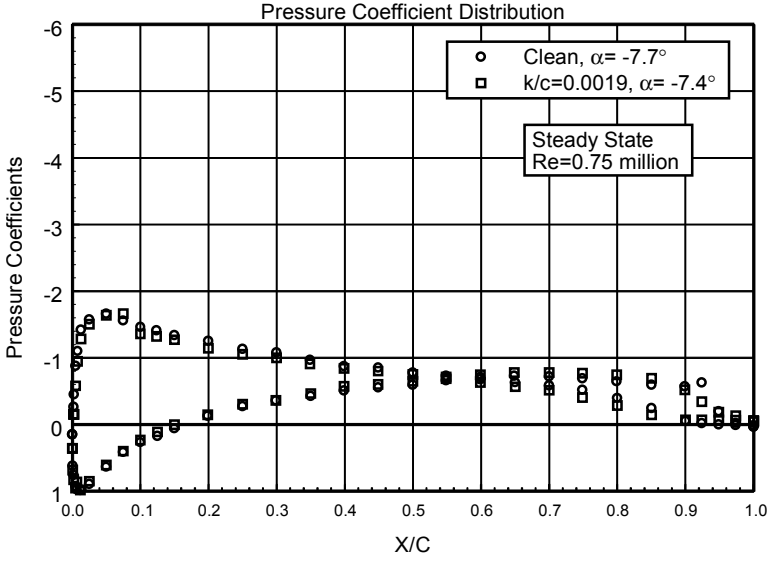

Figure 7. α = -7.7°

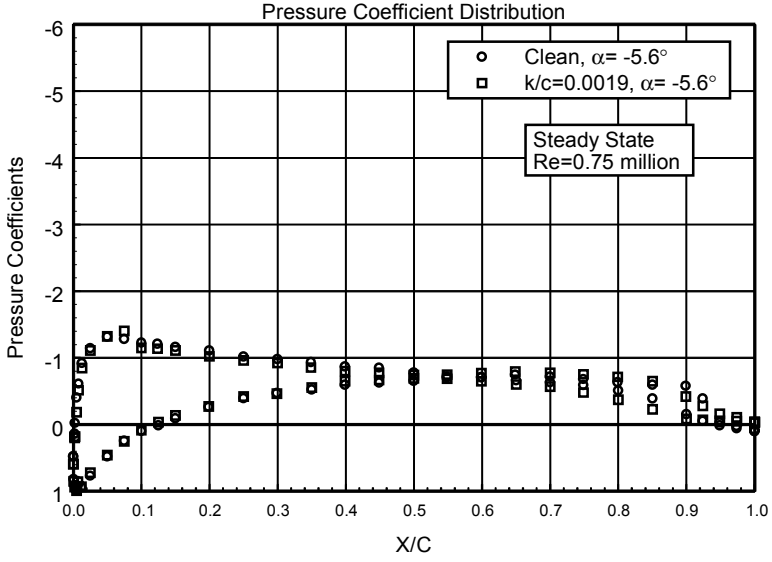

Figure 8. α = -5.6°

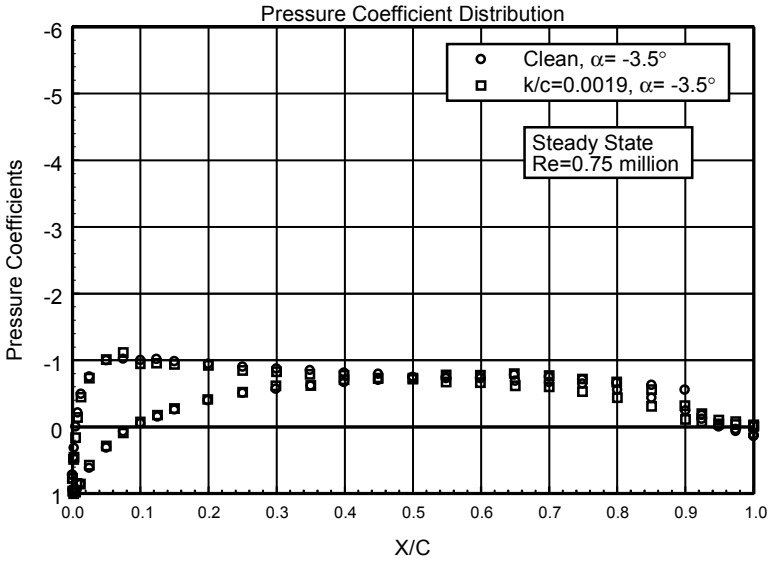

Figure 9. α = -3.5°

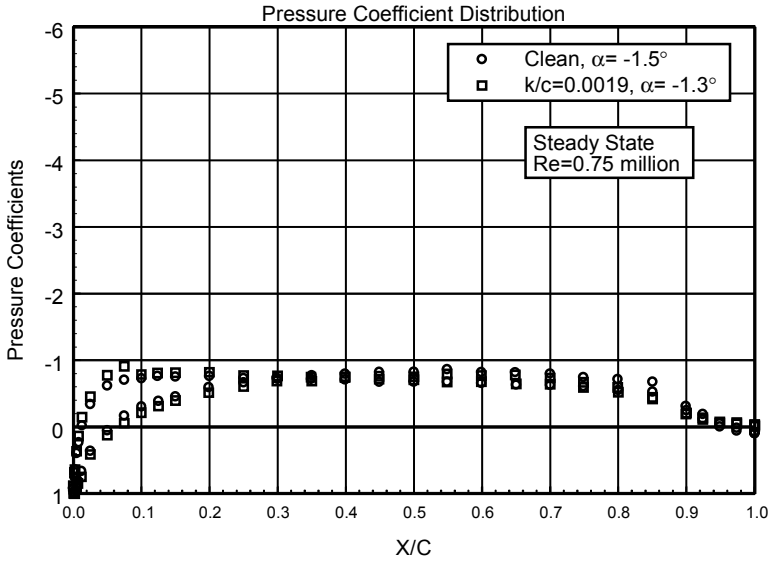

Figure 10. α = -1.5°

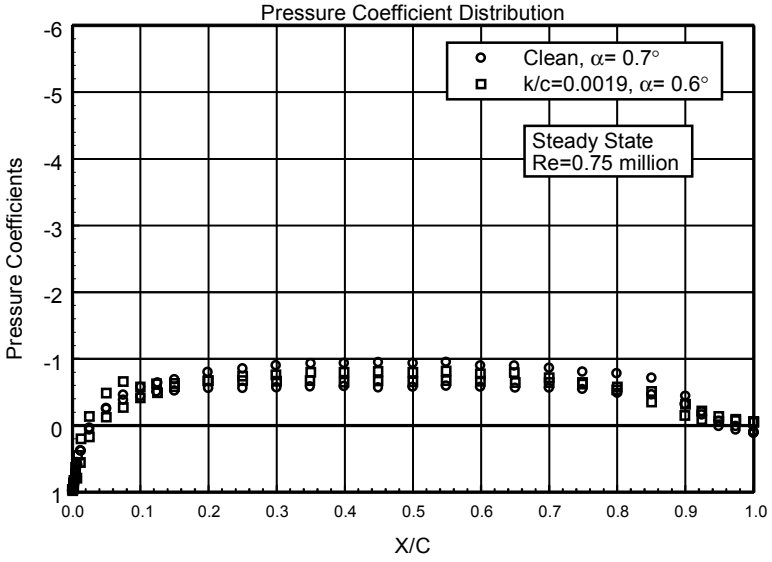

Figure 11. α = 0.7°

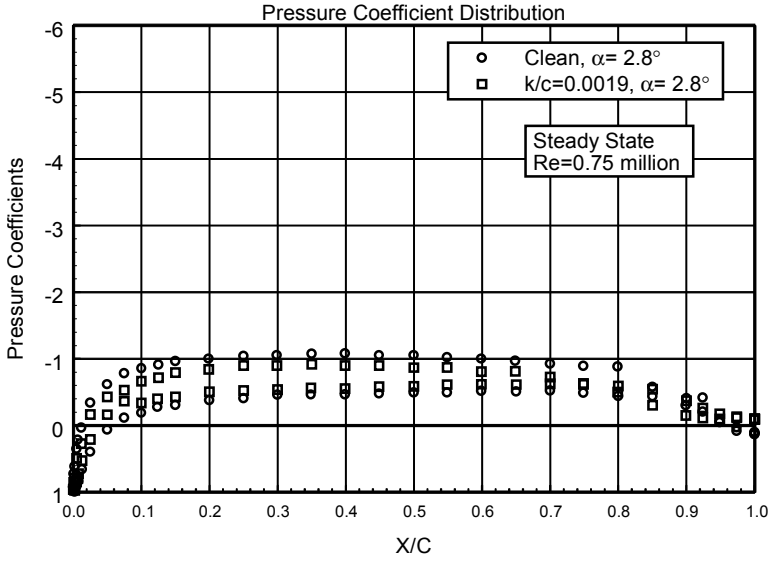

Figure 12. α = 2.8°

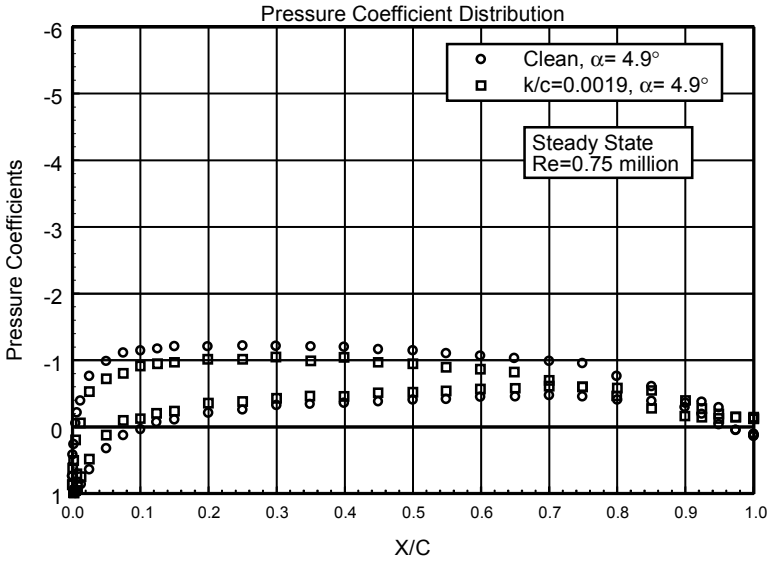

Figure 13. α = 4.9°

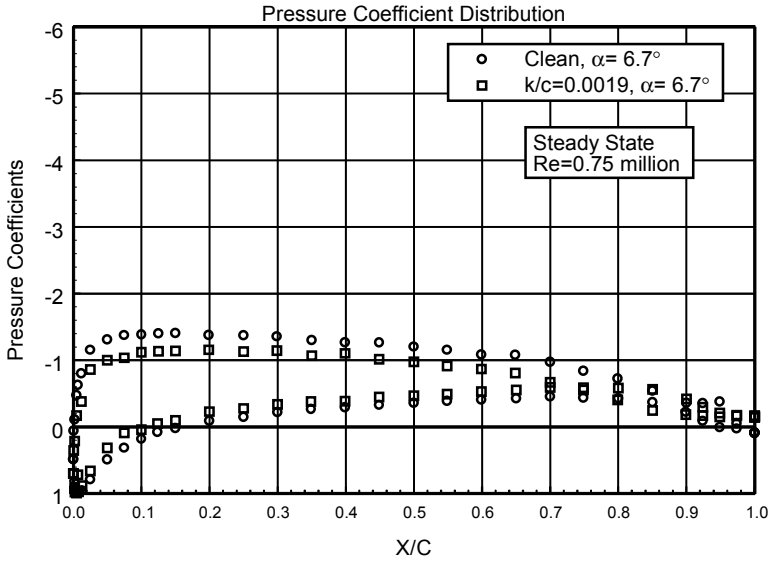

Figure 14. α = 6.7°

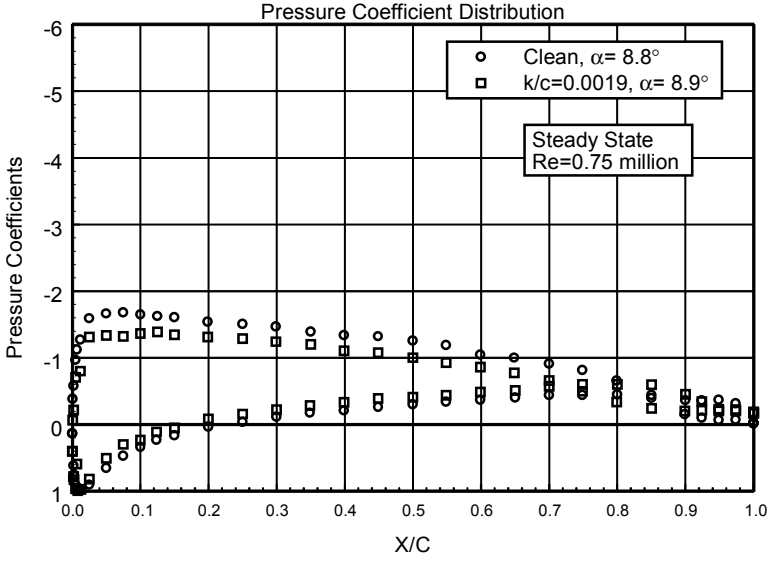

Figure 15. α = 8.8°

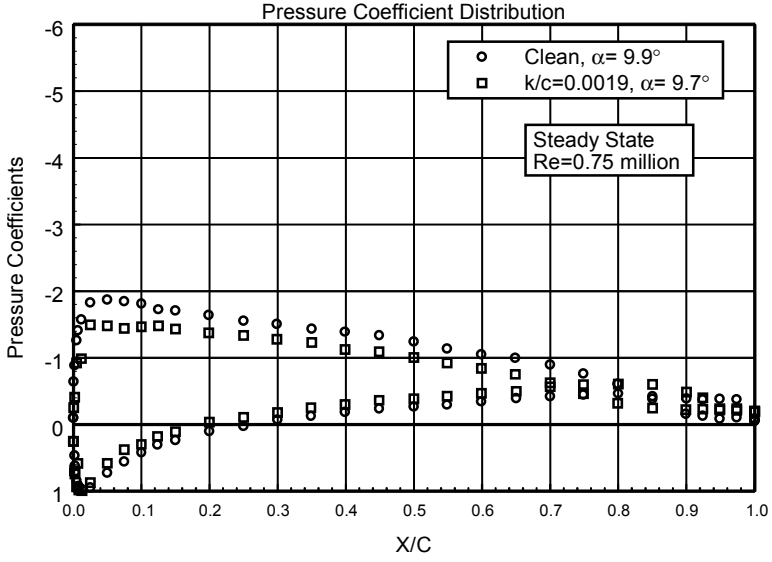

Figure 16. α = 9.9°

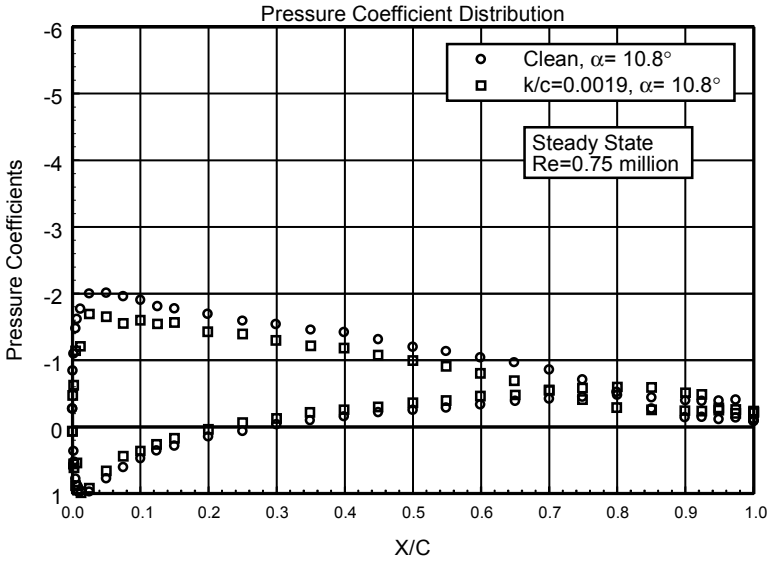

Figure 17. α = 10.8°

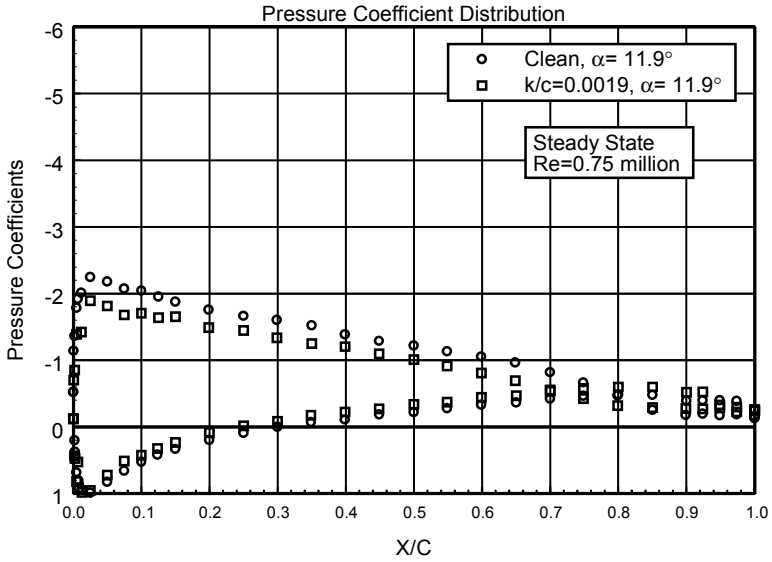

Figure 18. α = 11.9°

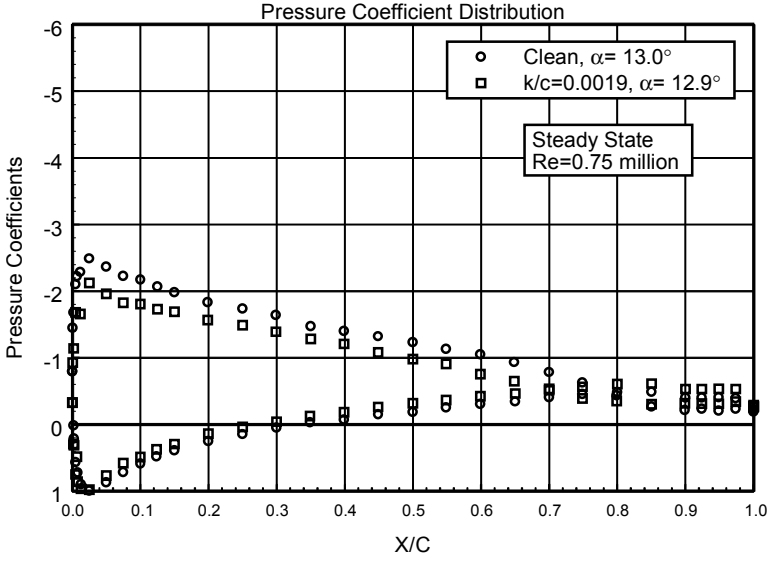

Figure 19. α = 13.0°

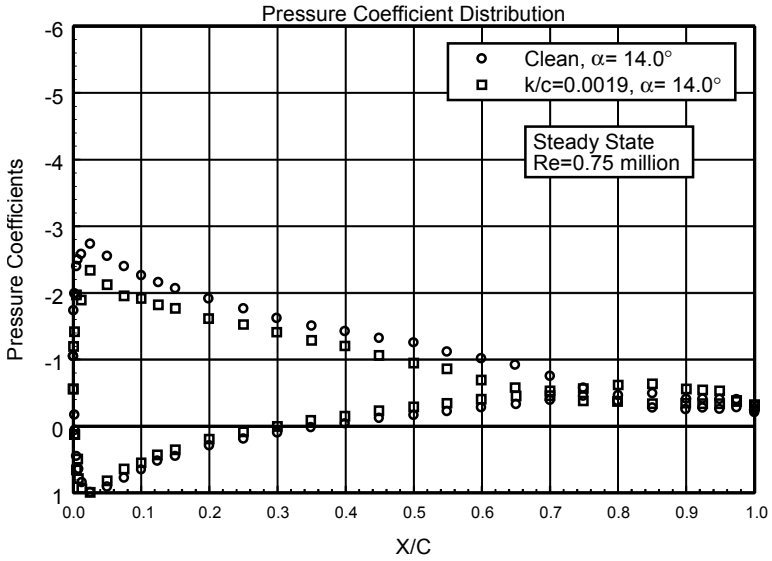

Figure 20. α = 14.0°

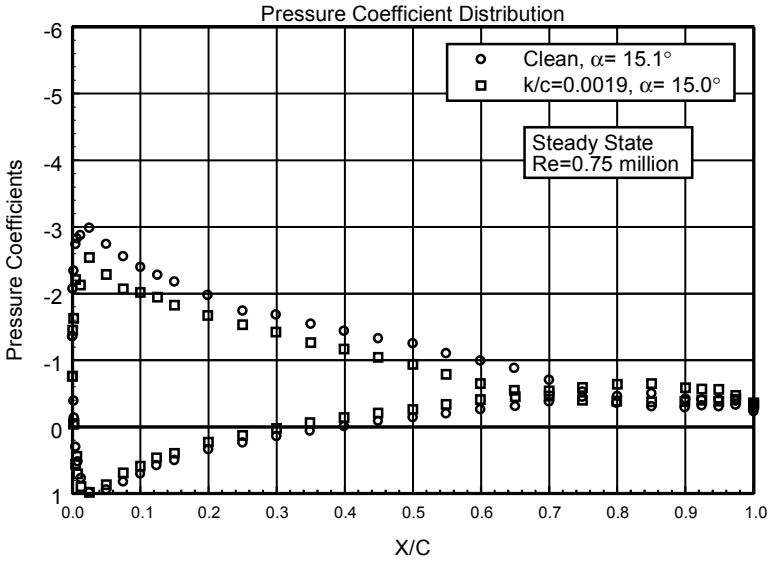

Figure 21. α = 15.1°

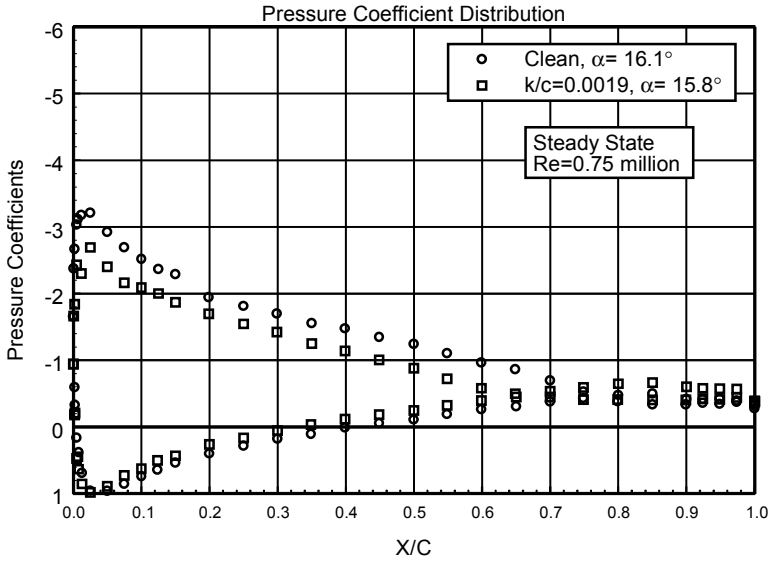

Figure 22. α = 16.1°

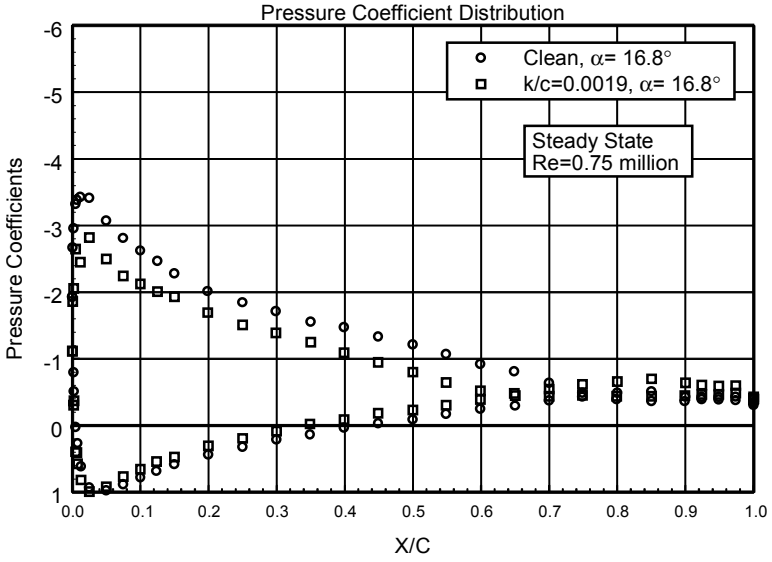

Figure 23. α = 16.8°

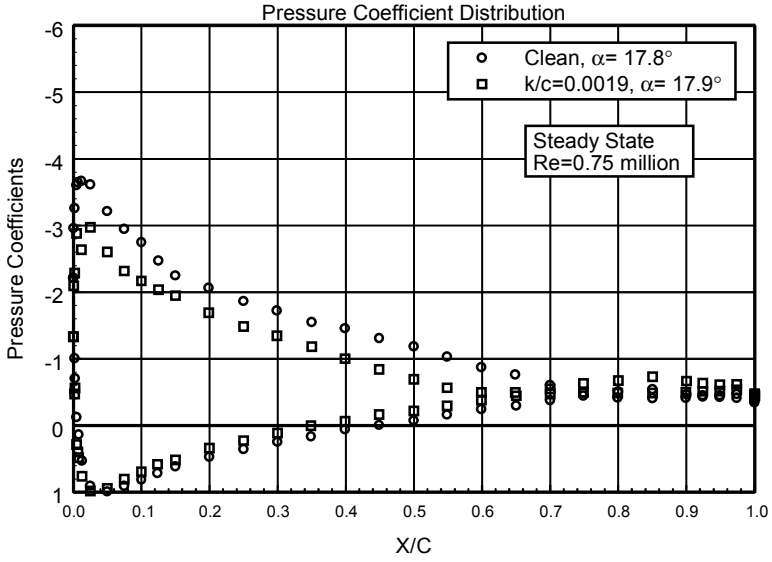

Figure 24. α = 17.8°

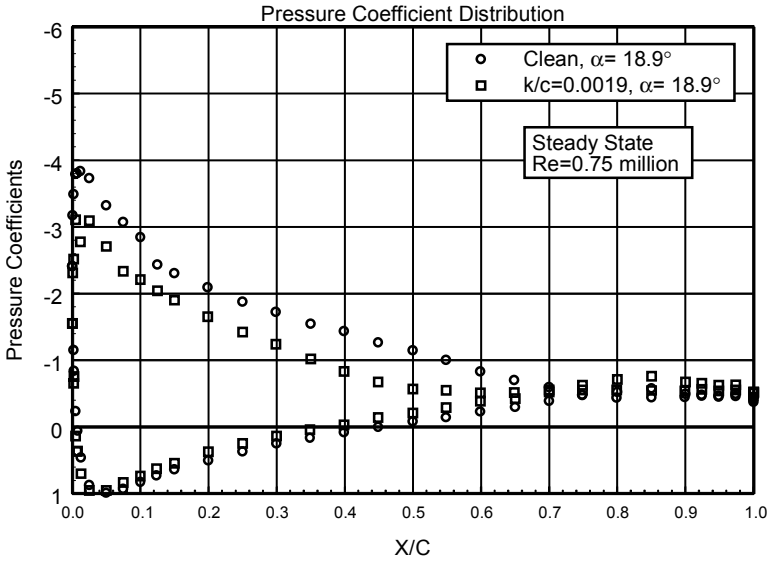

Figure 25. α = 18.9°

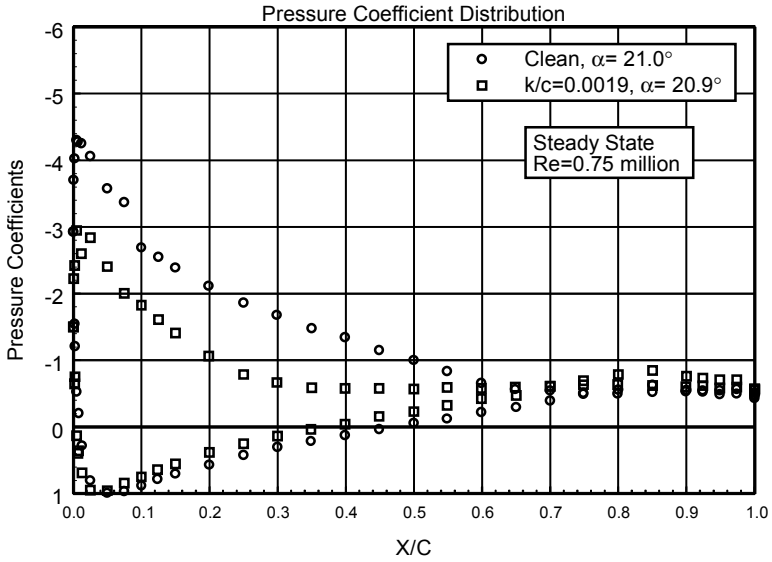

Figure 26. α = 21.0°

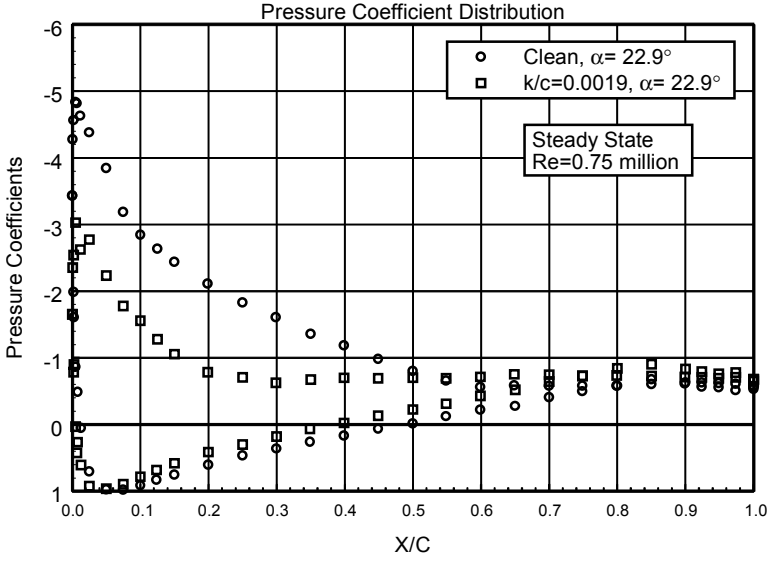

Figure 27. α = 22.9°

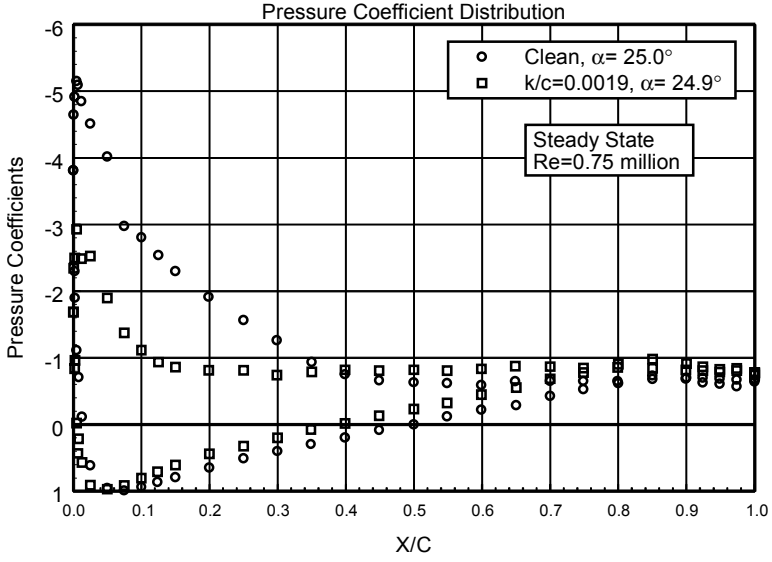

Figure 28. α = 25.0°

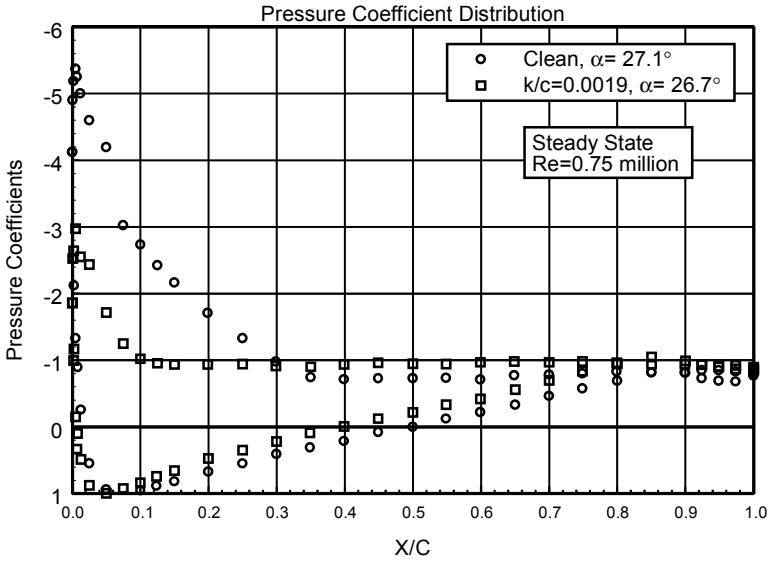

Figure 29. α = 27.1°

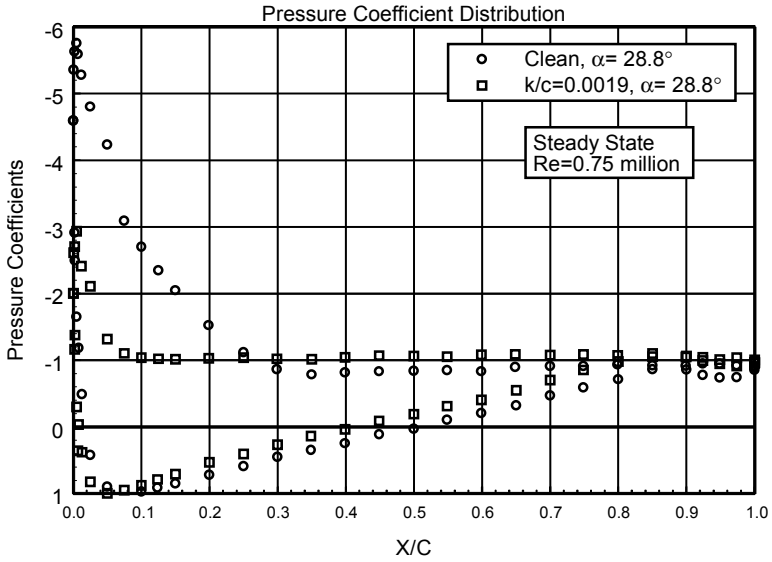

Figure 30. α = 28.8°

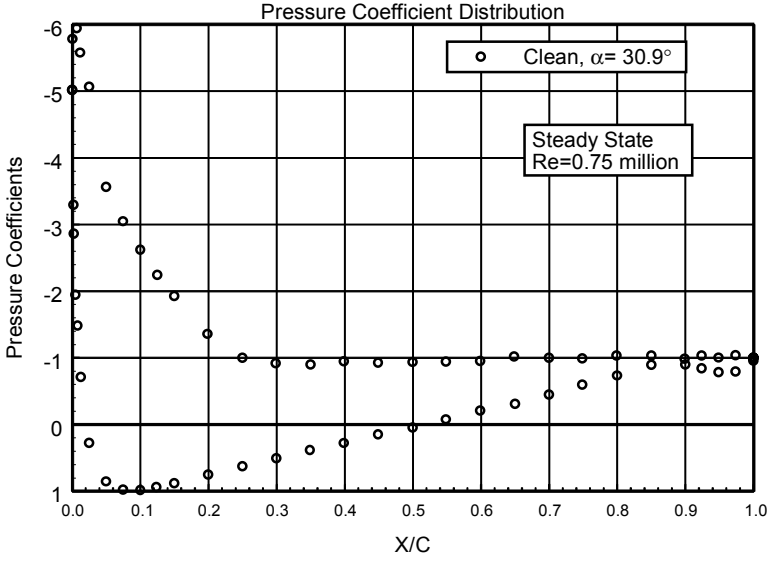

Figure 31. α = 30.9°

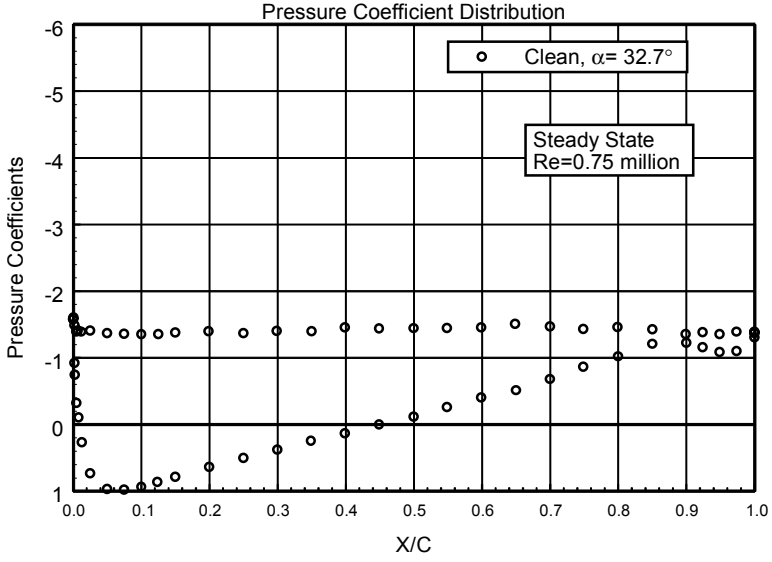

Figure 32. α = 32.7°

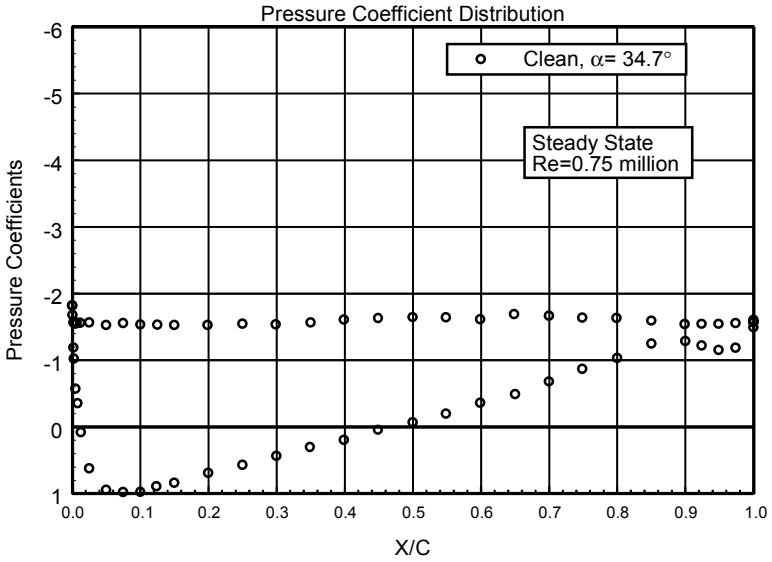

Figure 33. α = 34.7°

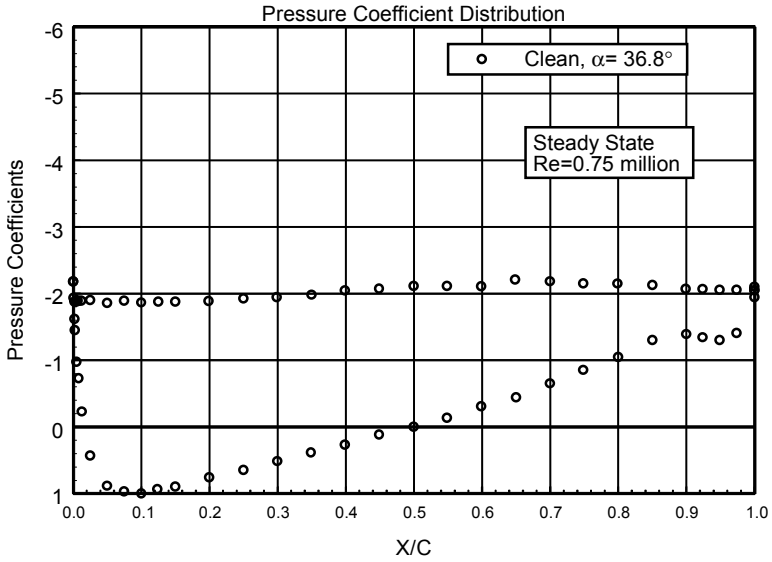

Figure 34. α = 36.8°

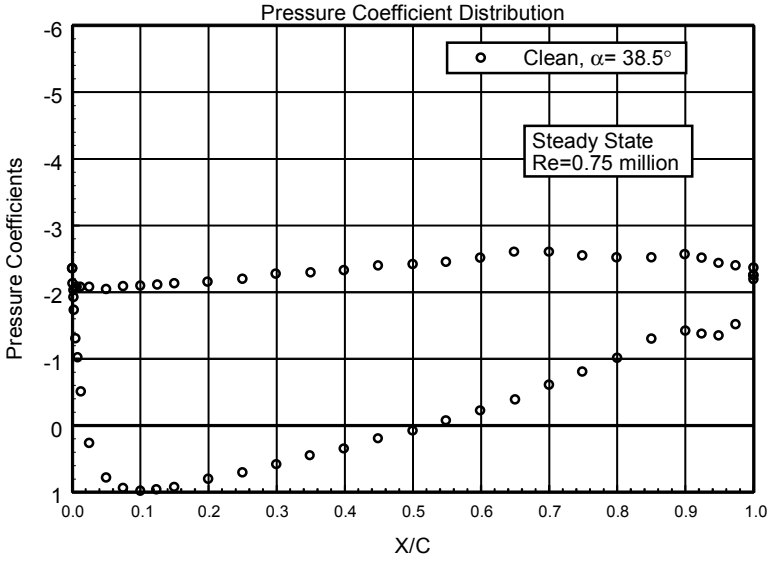

Figure 35. α = 38.5°

L303

Pressure Distributions, Steady State, Re = 1 million

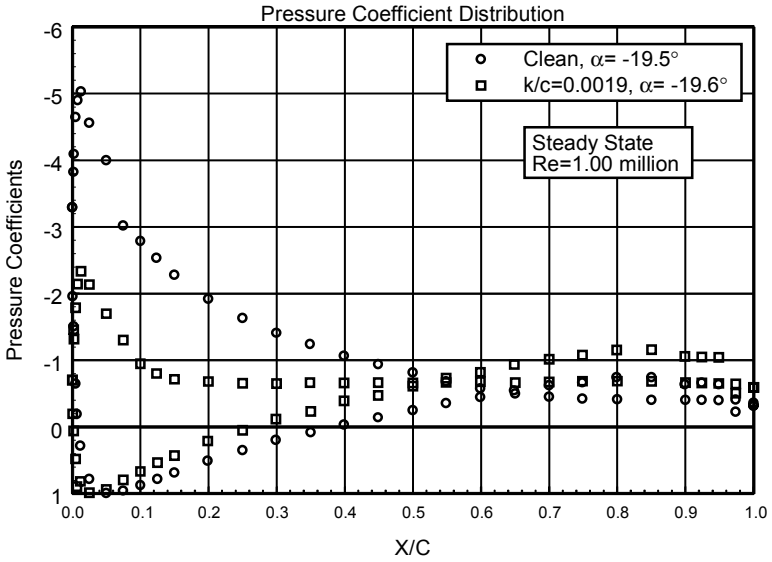

Figure 36. α = -19.5°

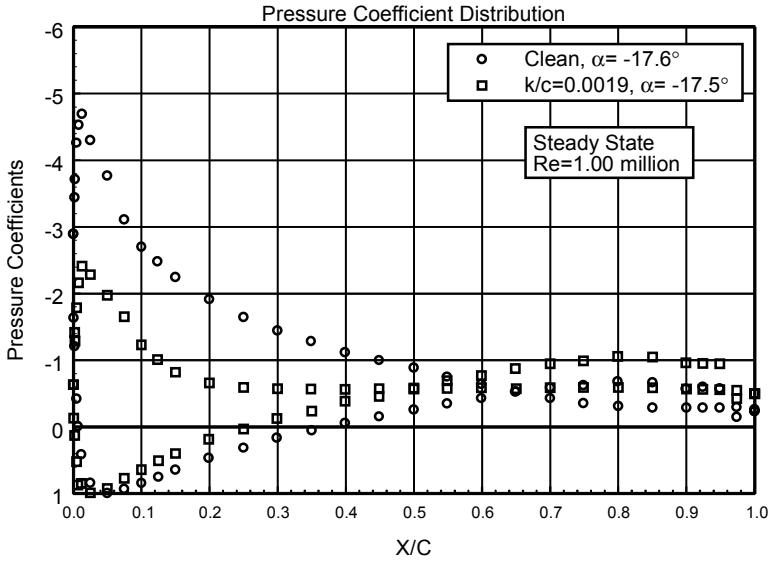

Figure 37. α = -17.6°

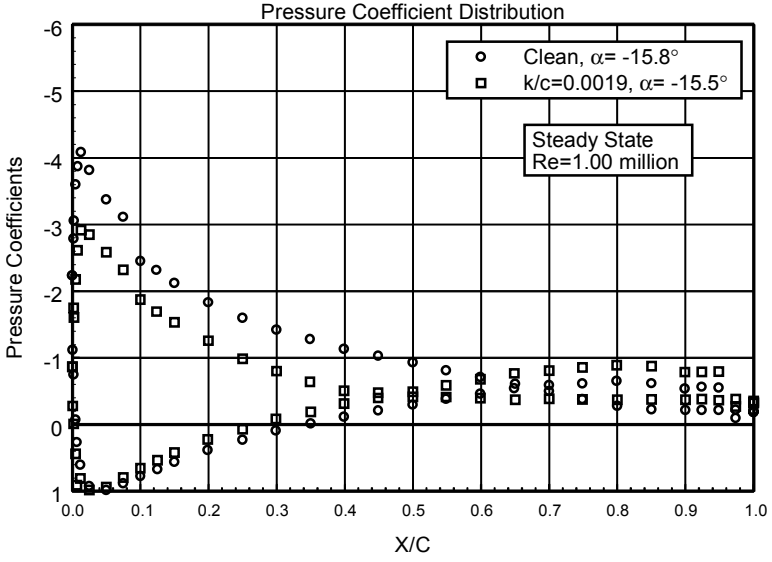

Figure 38. α = -15.8°

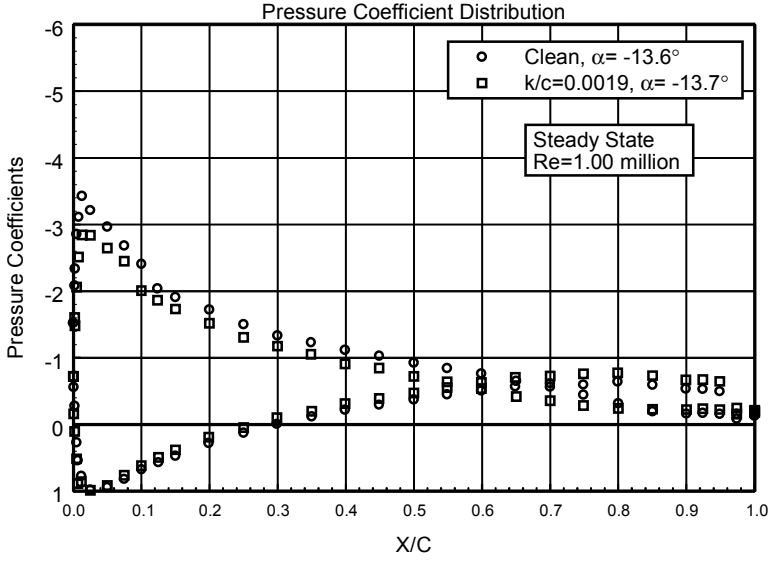

Figure 39. α = -13.6°

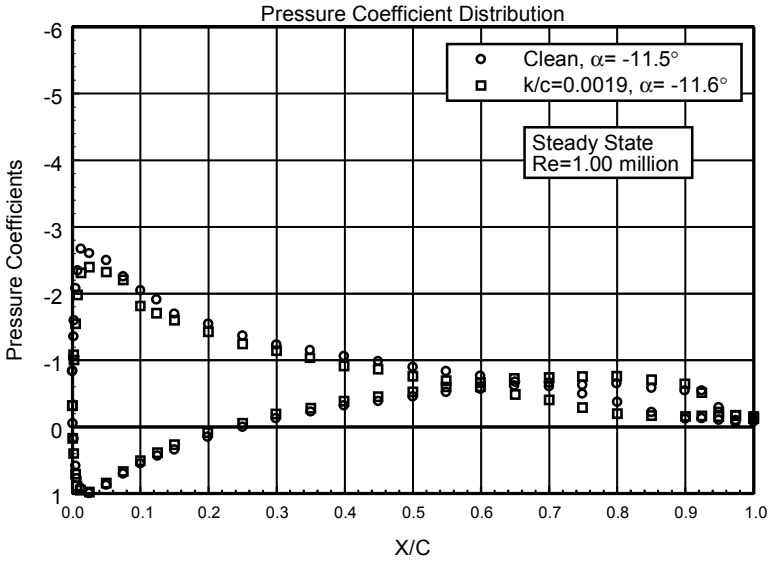

Figure 40. α = -11.5°

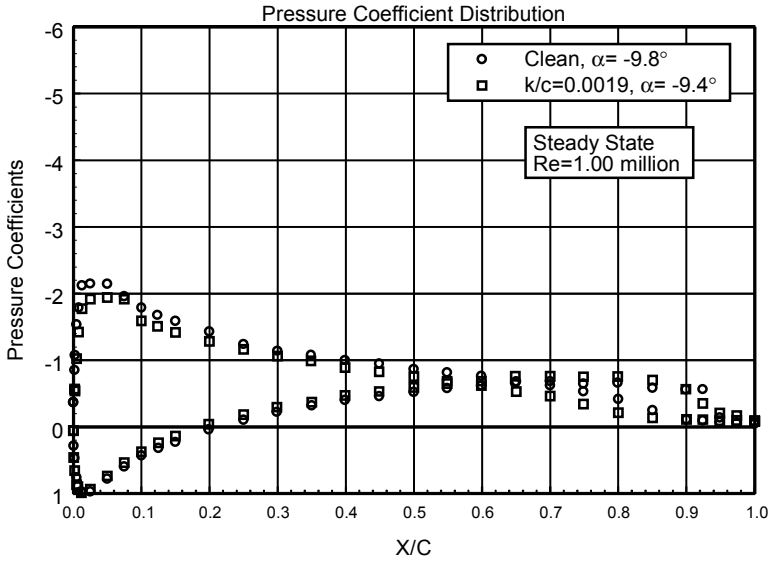

Figure 41. α = -9.8°

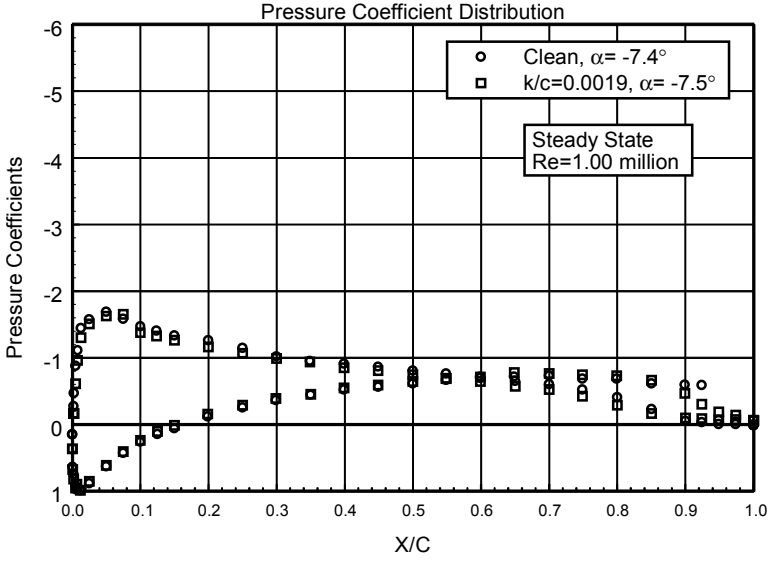

Figure 42. α = -7.4°

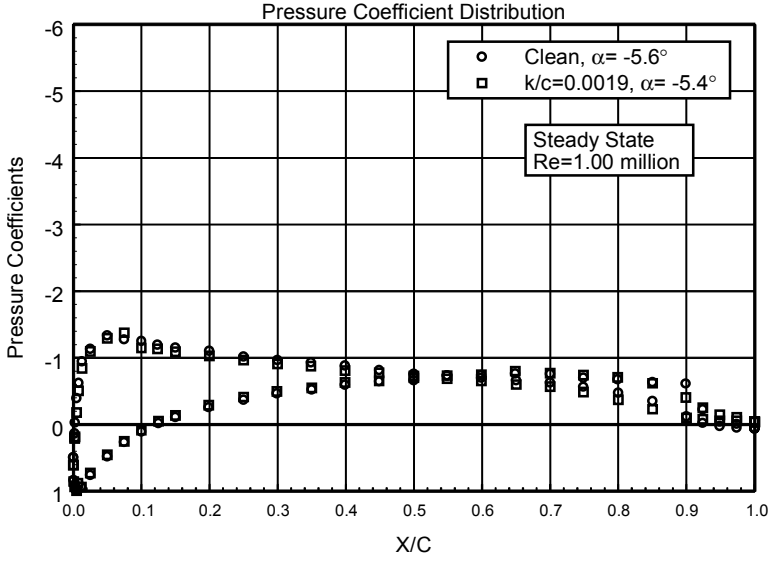

Figure 43. α = -5.6°

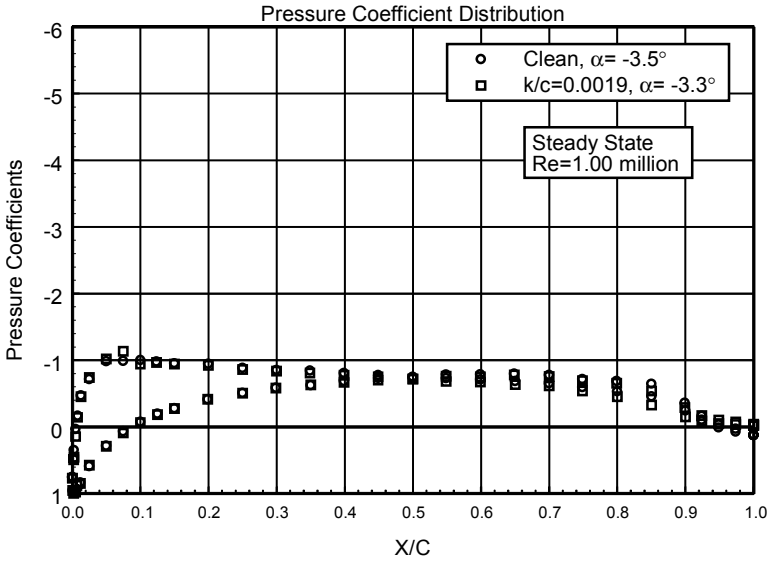

Figure 44. α = -3.5°

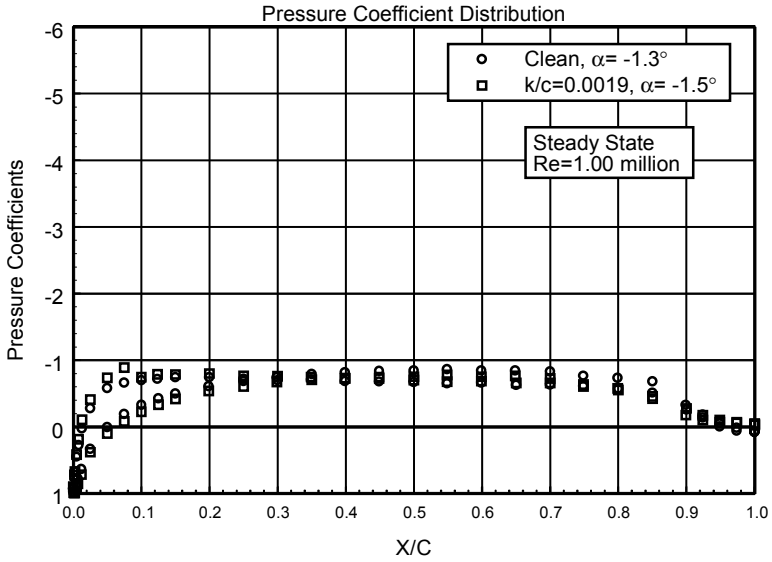

Figure 45. α = -1.3°

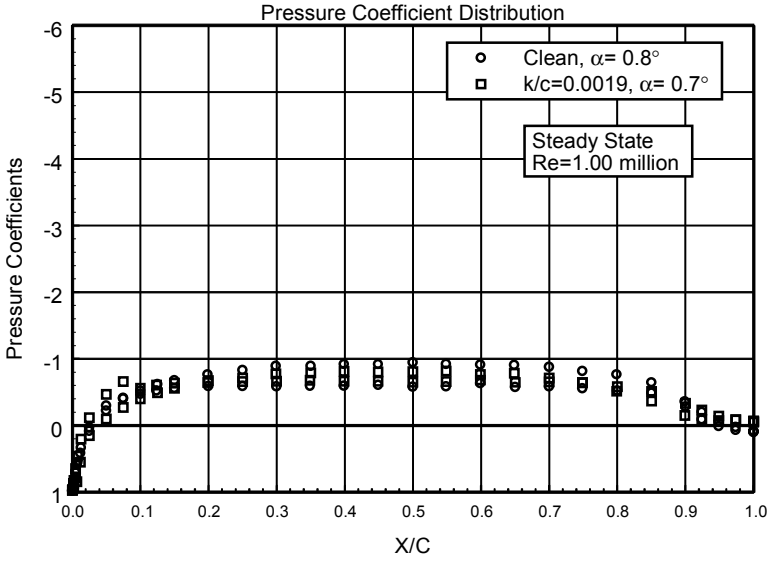

Figure 46. α = 0.8°

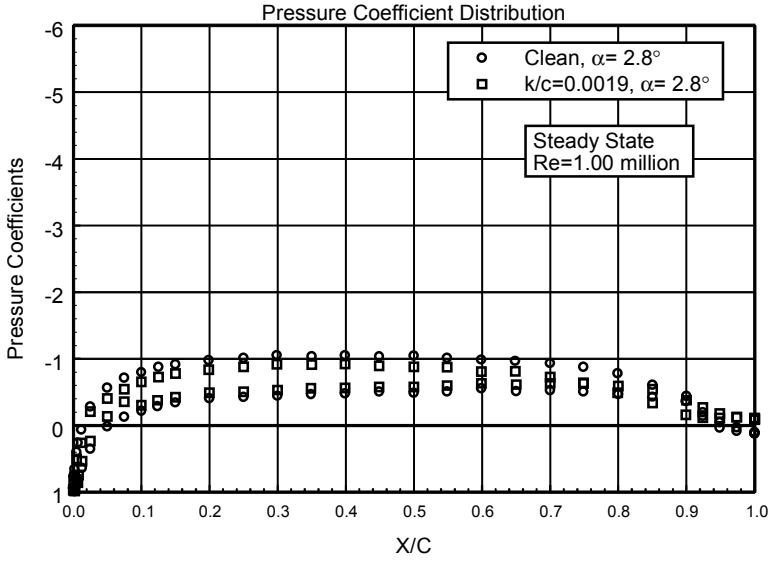

Figure 47. α = 2.8°

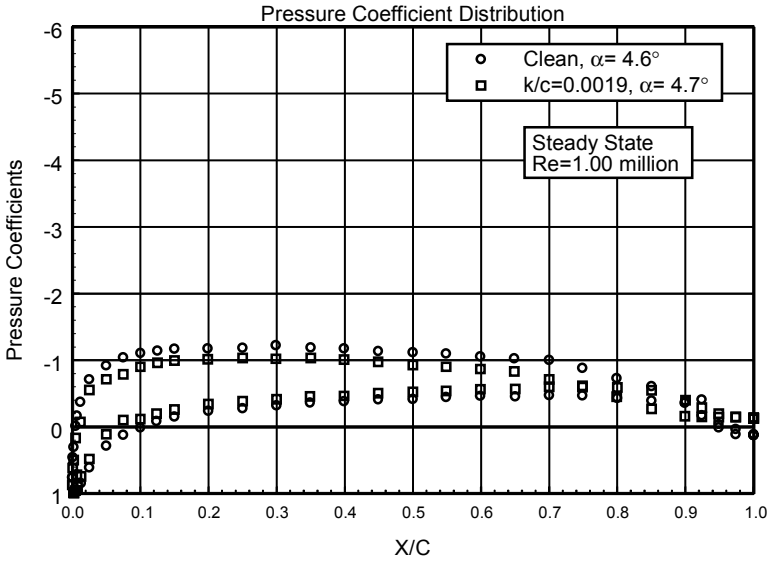

Figure 48. α = 4.6°

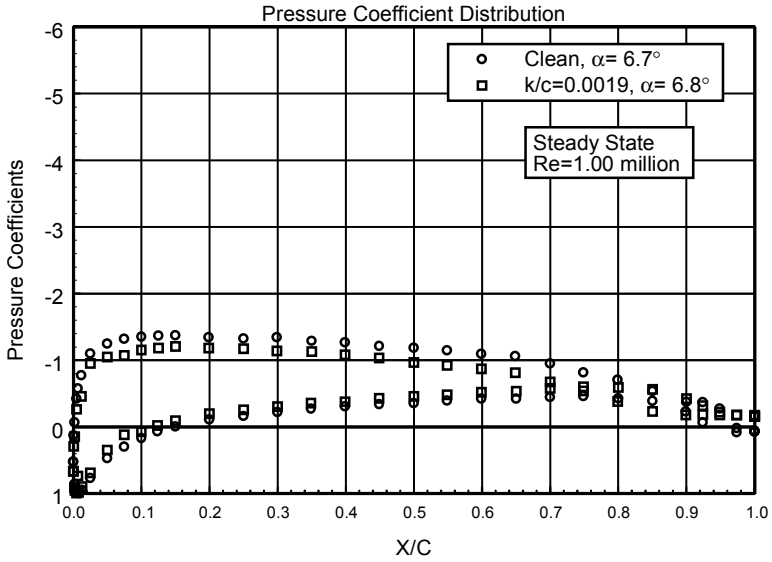

Figure 49. α = 6.7°

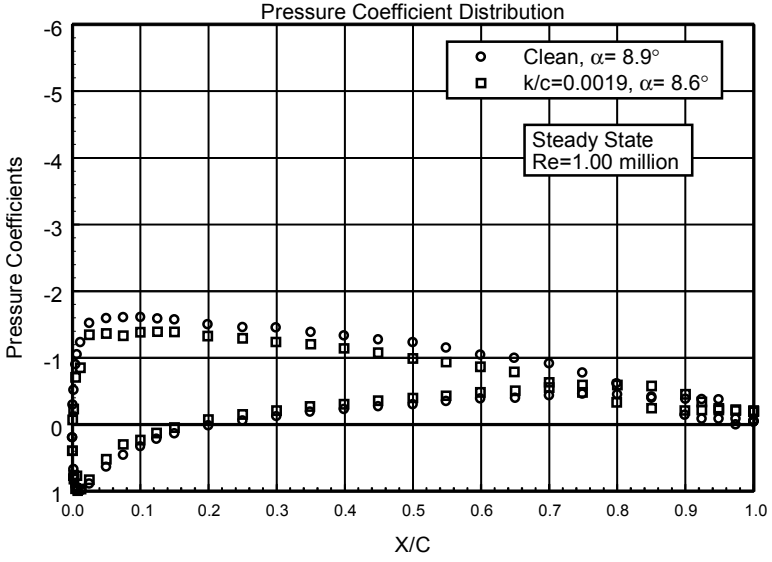

Figure 50. α = 8.9°

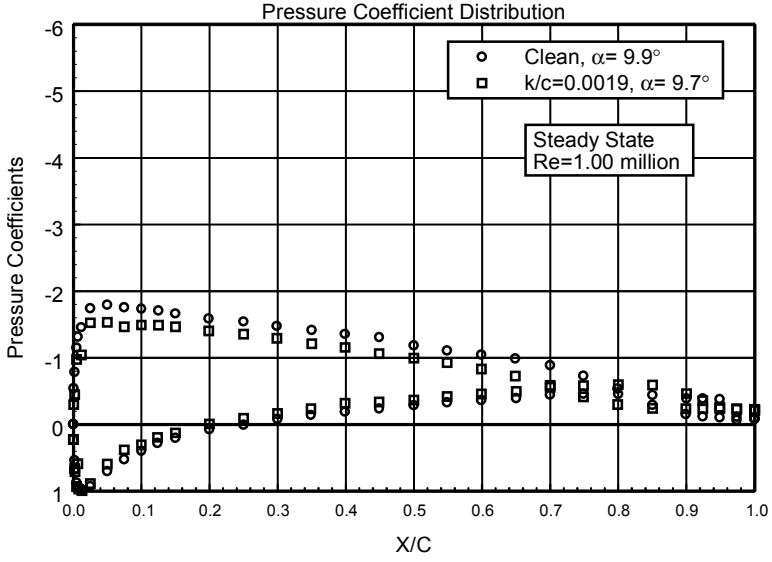

Figure 51. α = 9.9°

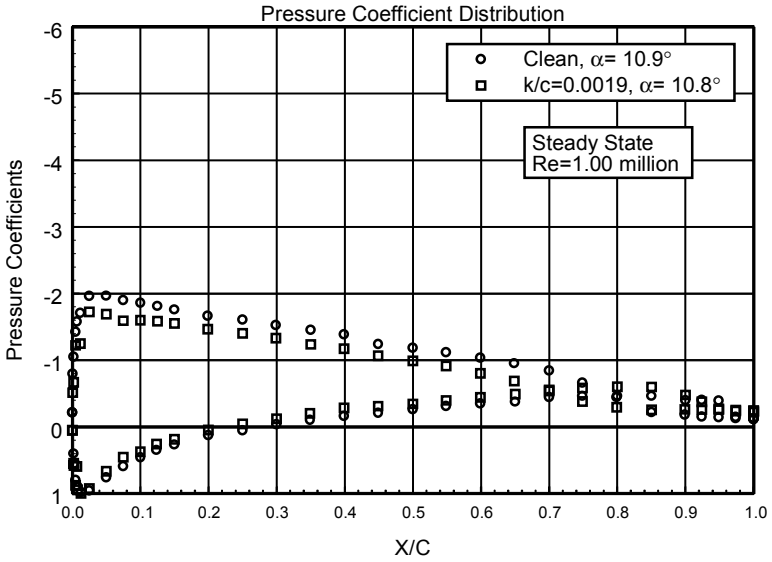

Figure 52. α = 10.9°

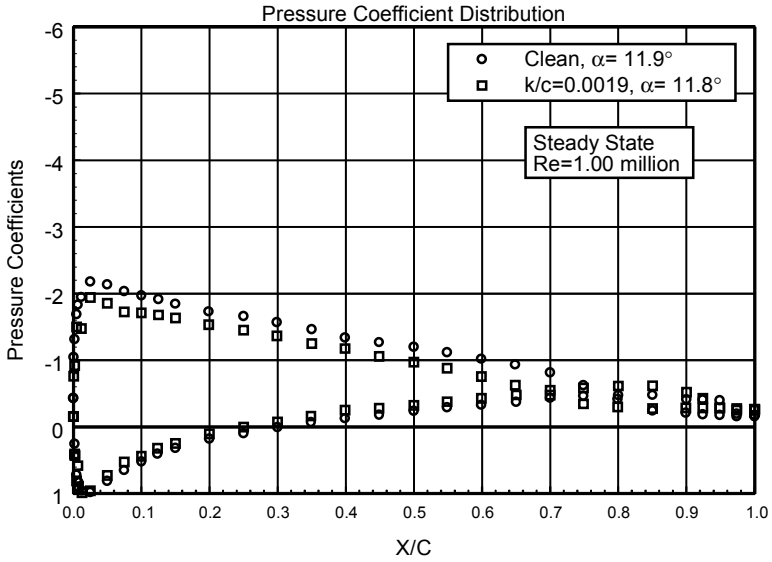

Figure 53. α = 11.9°

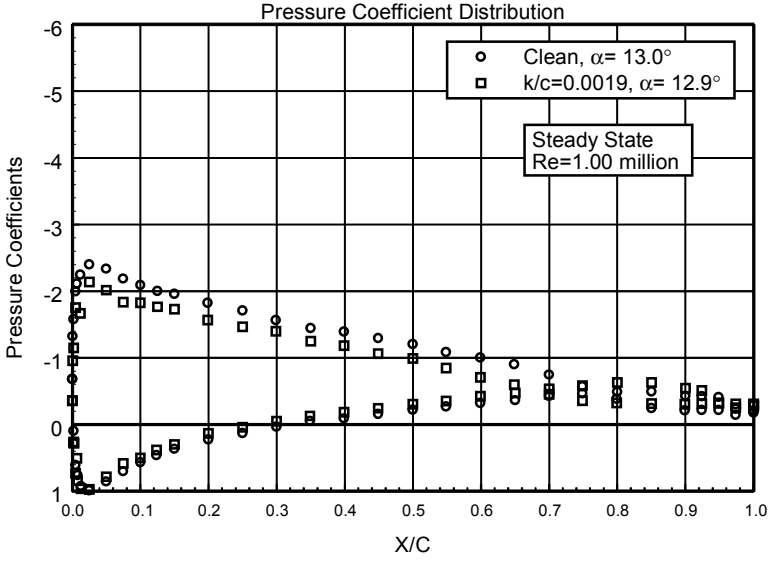

Figure 54. α = 13.0°

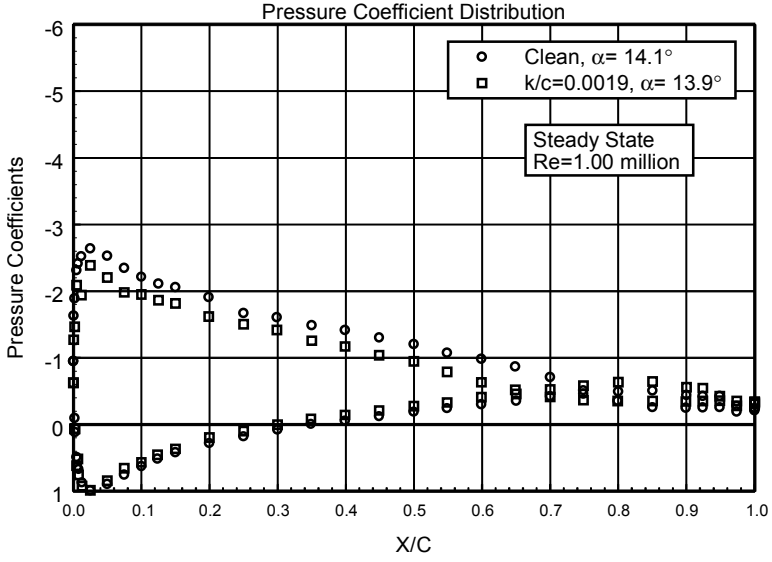

Figure 55. α = 14.1°

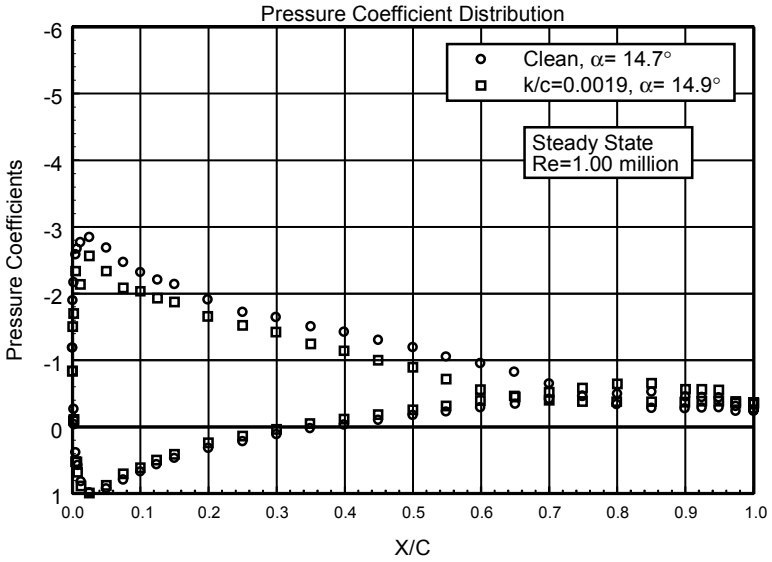

Figure 56. α = 14.7°

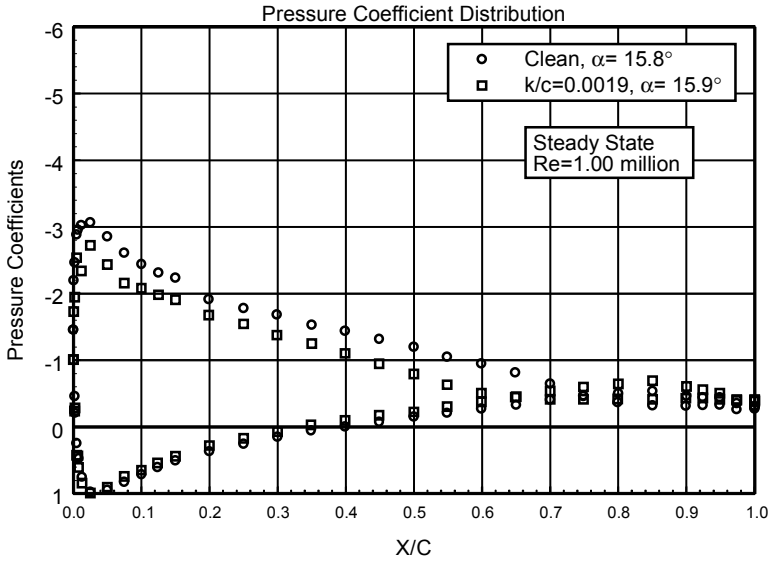

Figure 57. α = 15.8°

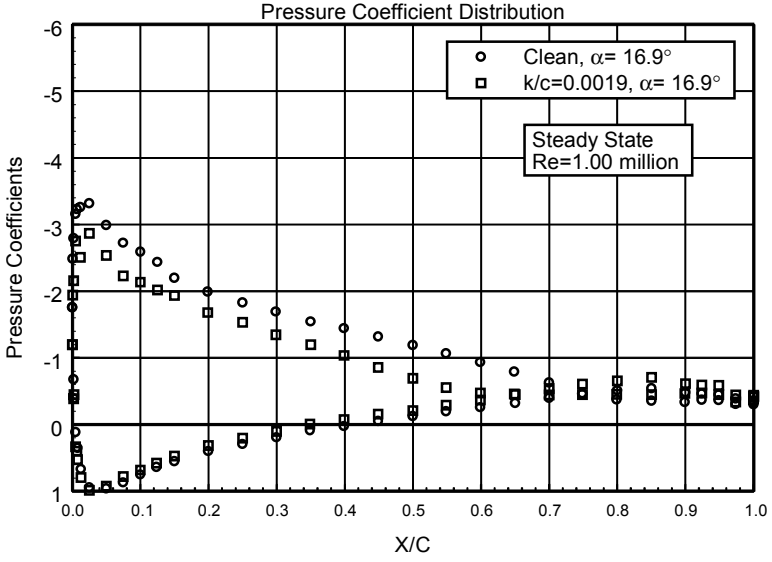

Figure 58. α = 16.9°

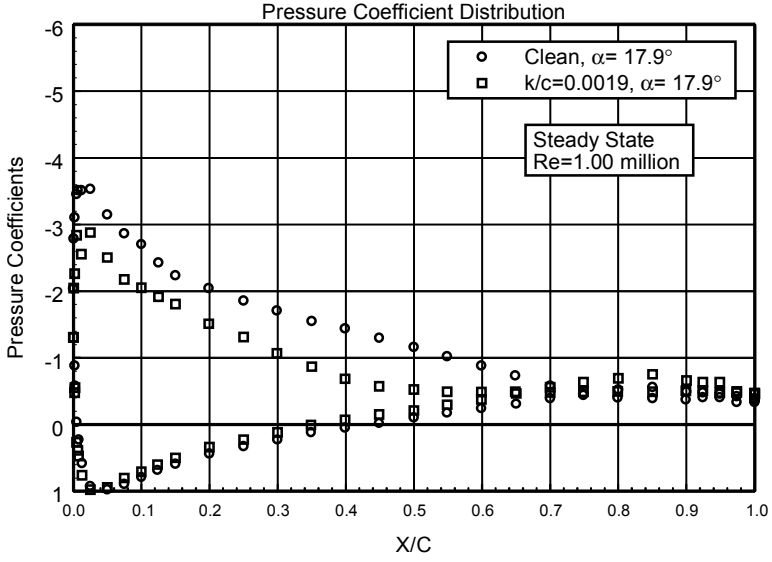

Figure 59. α = 17.9°

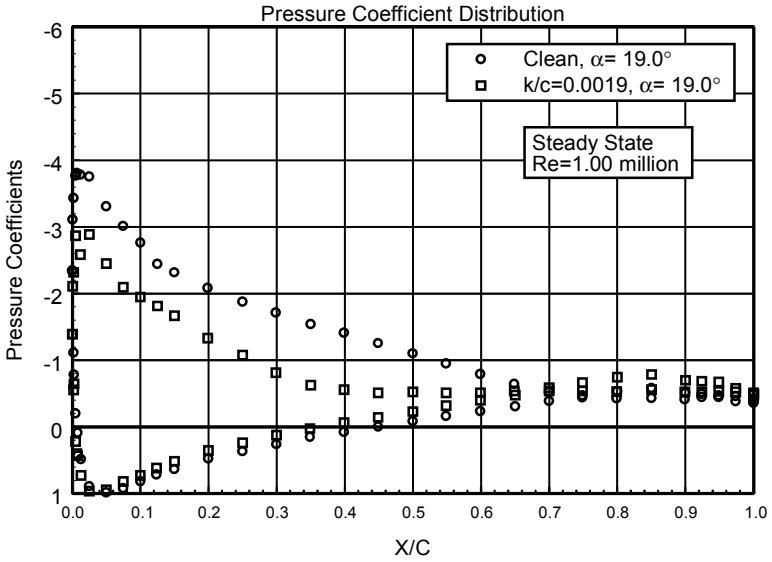

Figure 60. α = 19.0°

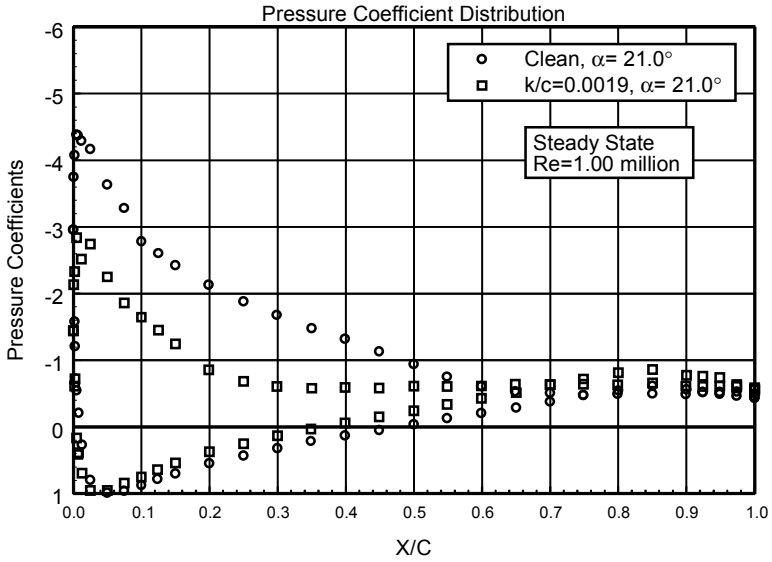

Figure 61. α = 21.0°

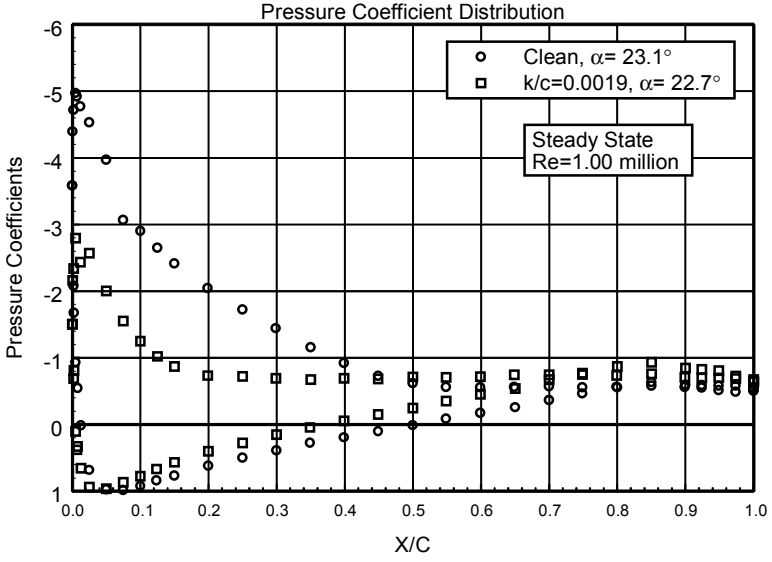

Figure 62. α = 23.1°

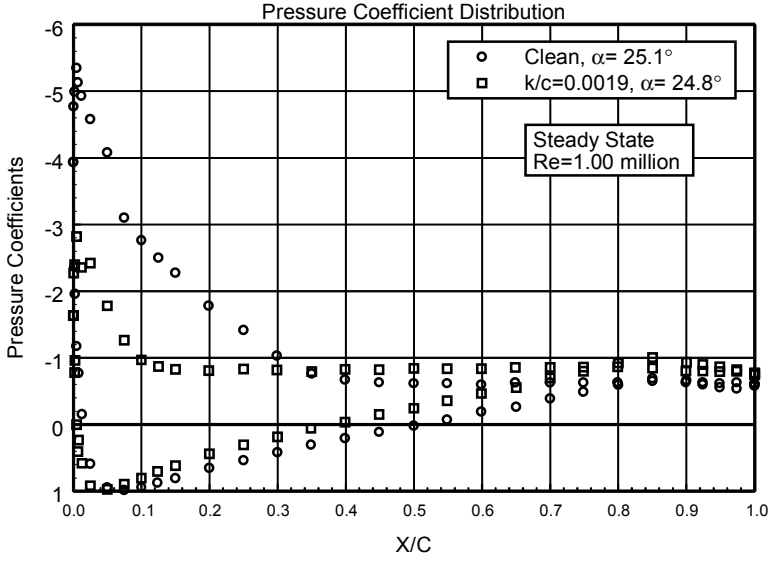

Figure 63. α = 25.1°

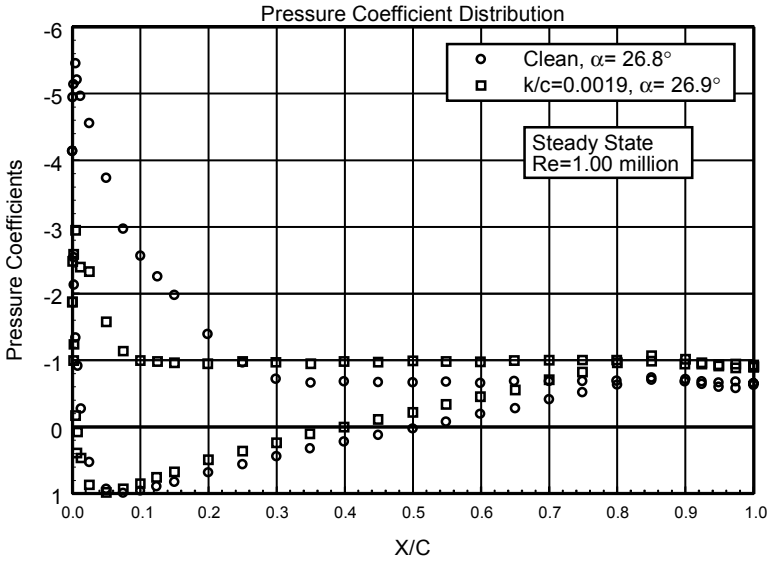

Figure 64. α = 26.8°

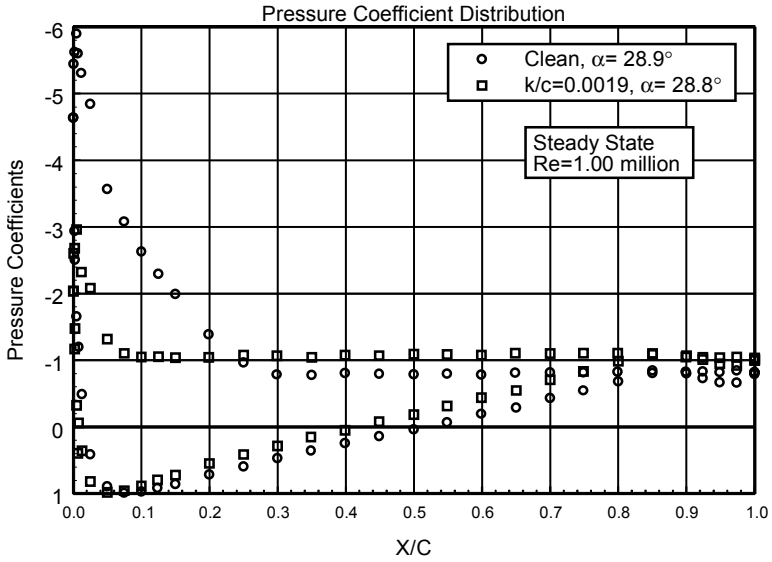

Figure 65. α = 28.9°

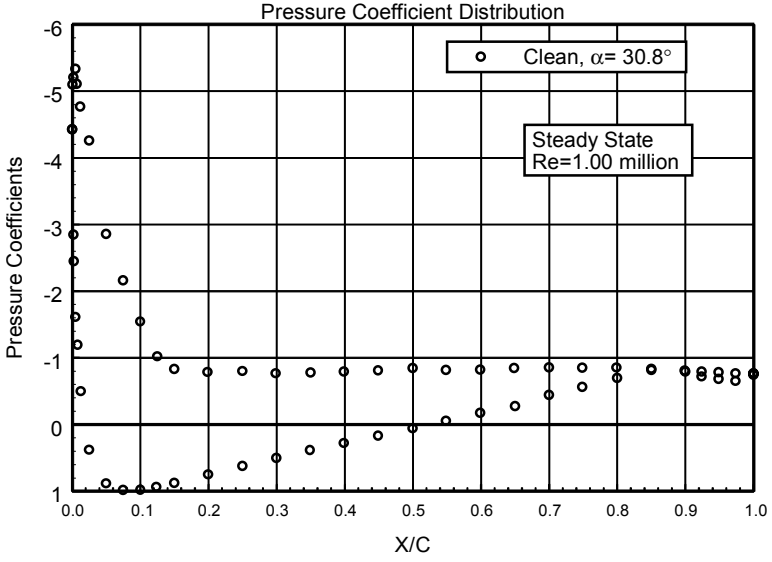

Figure 66. α = 30.8°

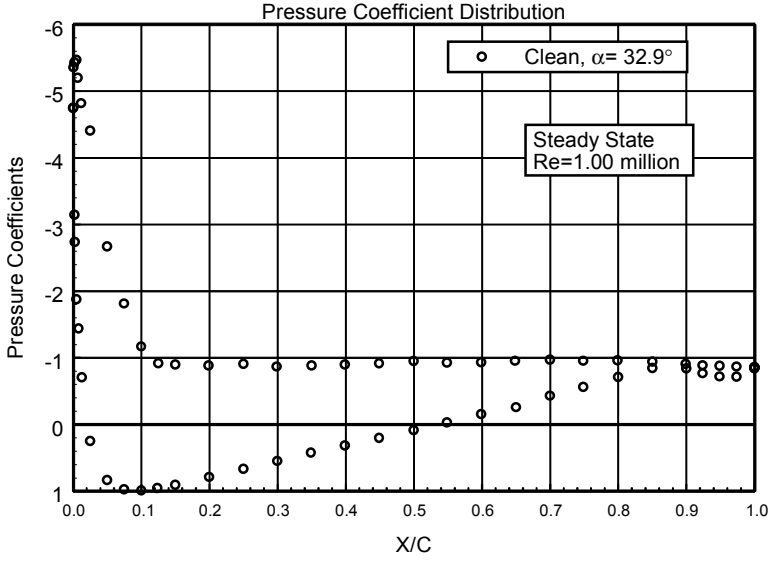

Figure 67. α = 32.9°

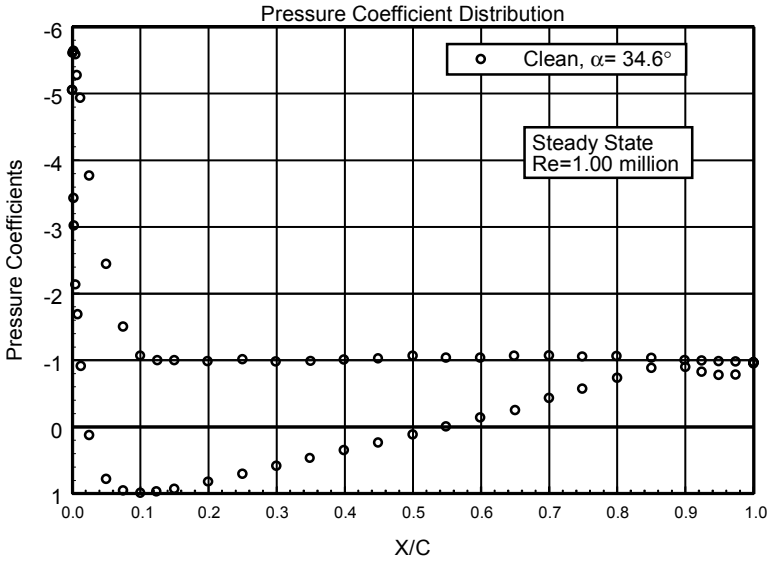

Figure 68. α = 34.6°

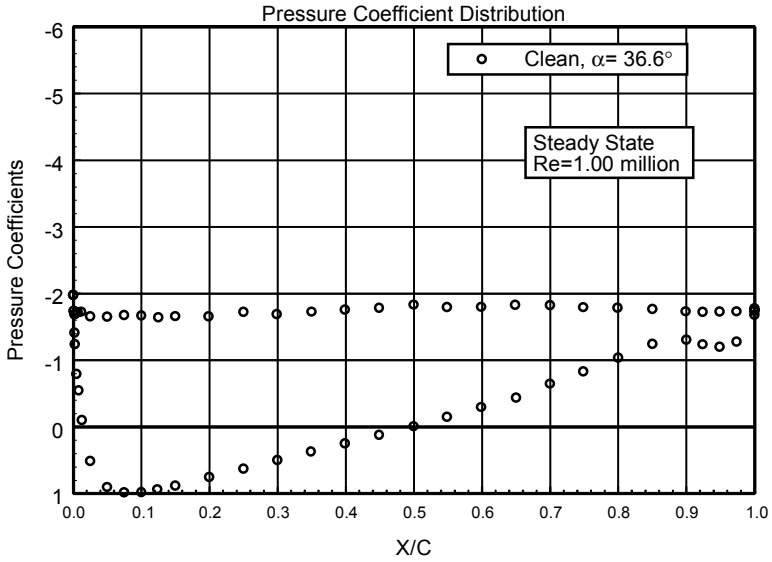

Figure 69. α = 36.6°

L303

Pressure Distributions, Steady State, Re = 1.25 million

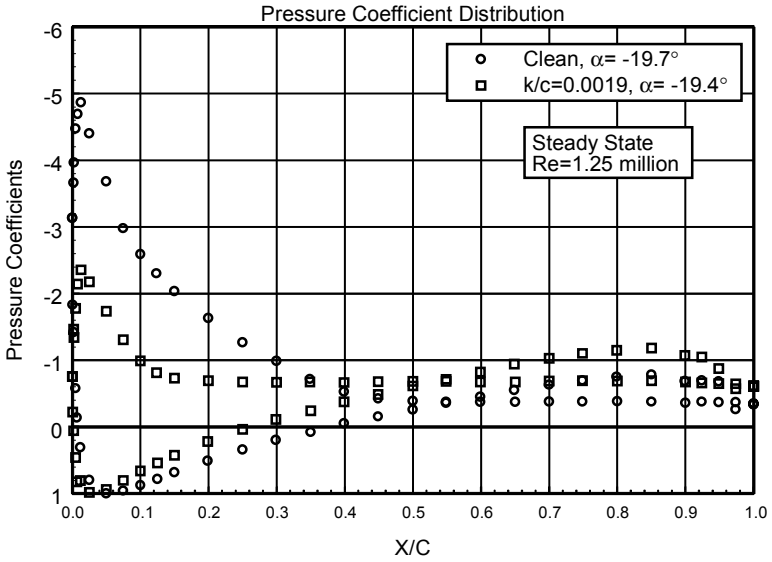

Figure 70. α = -19.7°

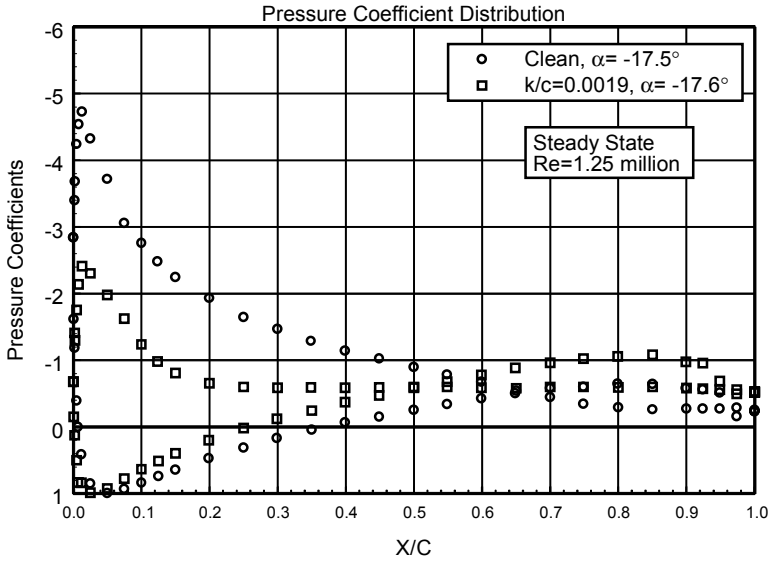

Figure 71. α = -17.5°

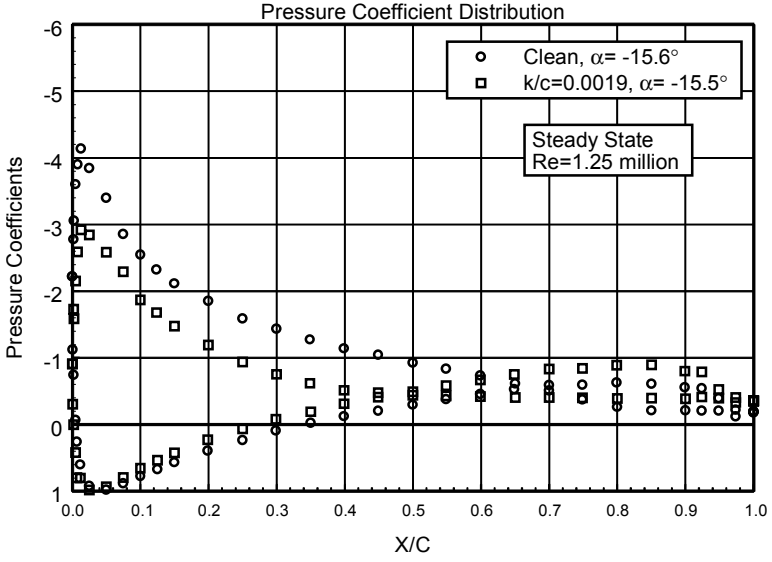

Figure 72. α = -15.6°

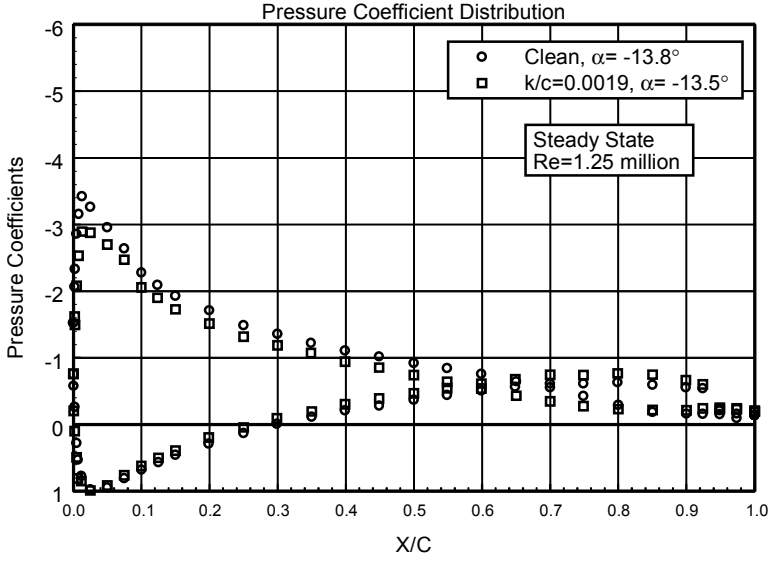

Figure 73. α = -13.8°

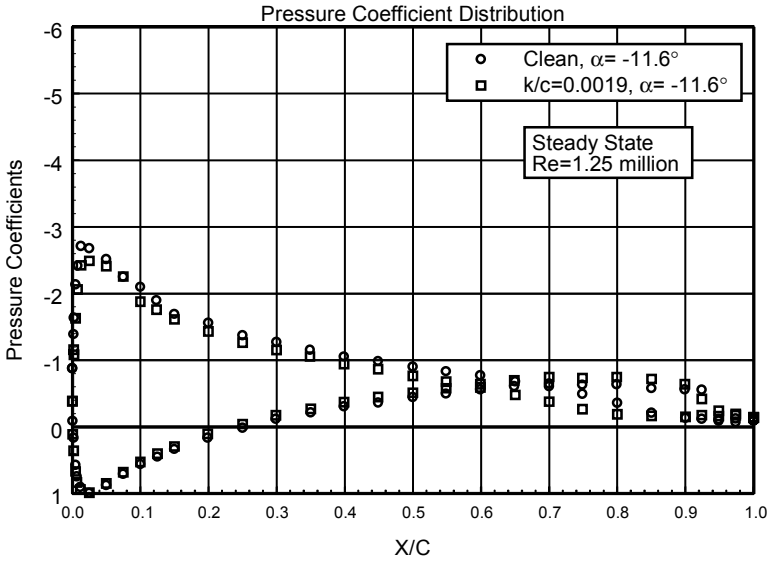

Figure 74. α = -11.6°

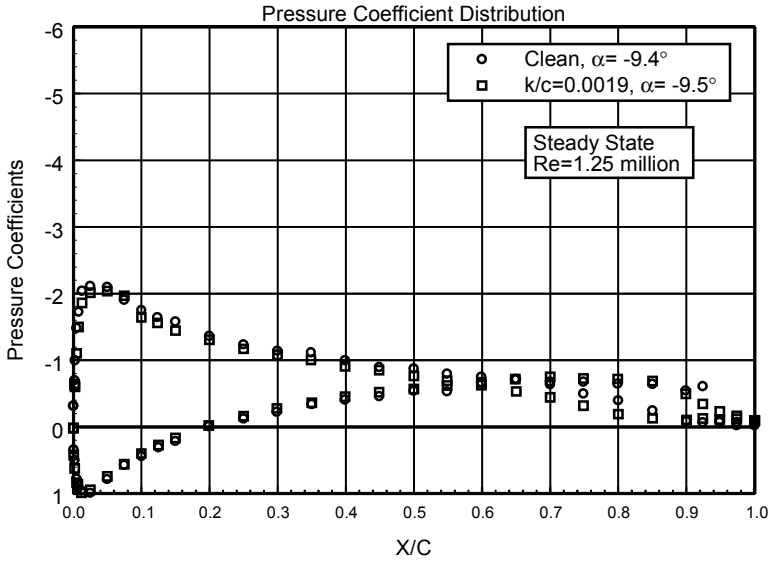

Figure 75. α = -9.4°

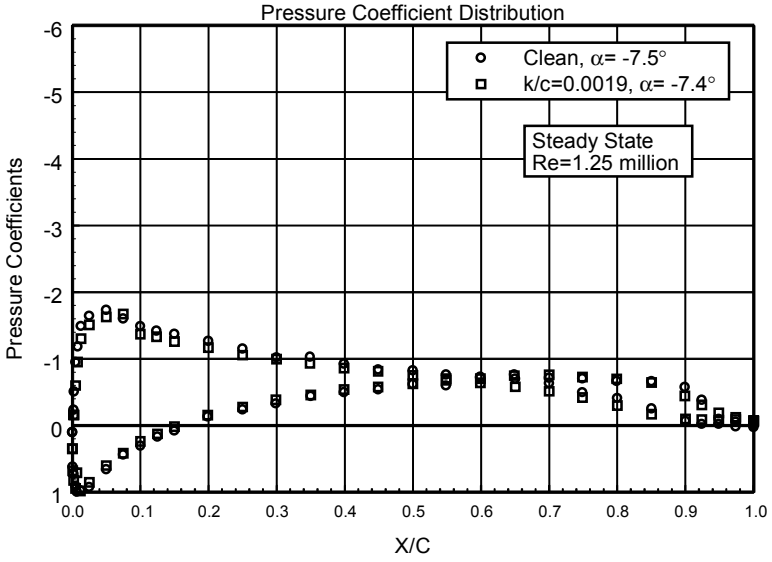

Figure 76. α = -7.5°

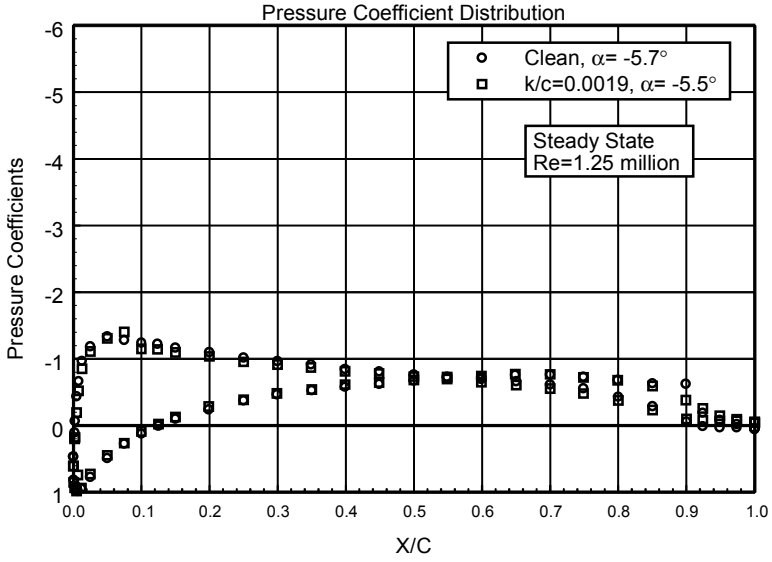

Figure 77. α = -5.7°

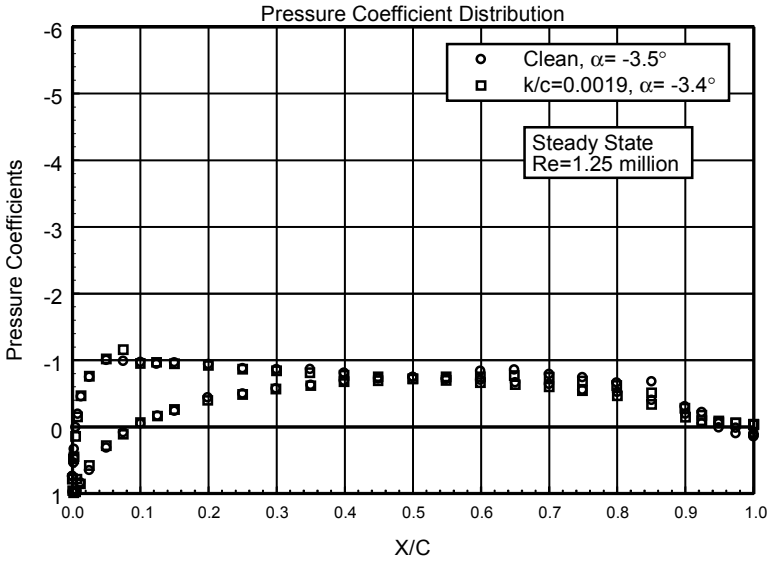

Figure 78. α = -3.5°

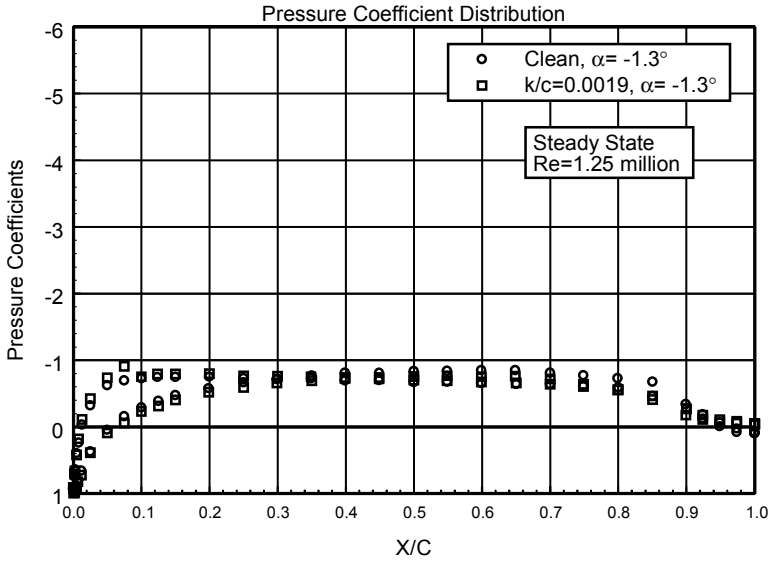

Figure 79. α = -1.3°

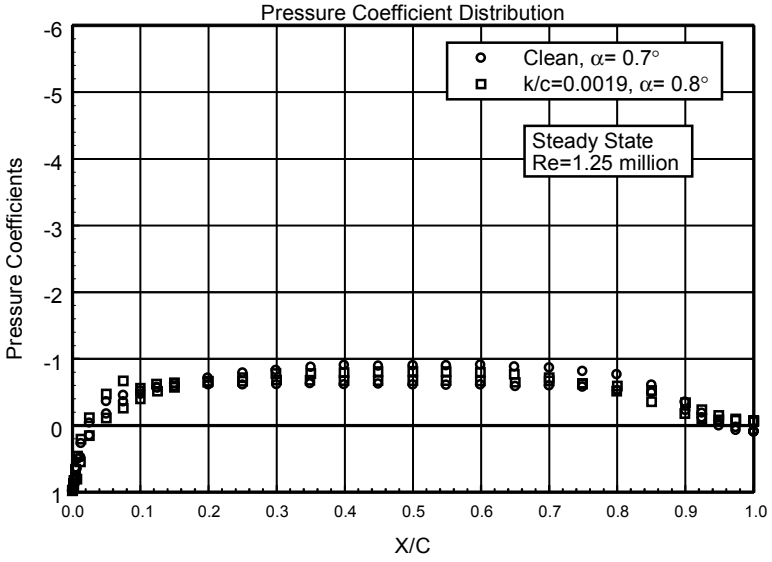

Figure 80. α = 0.7°

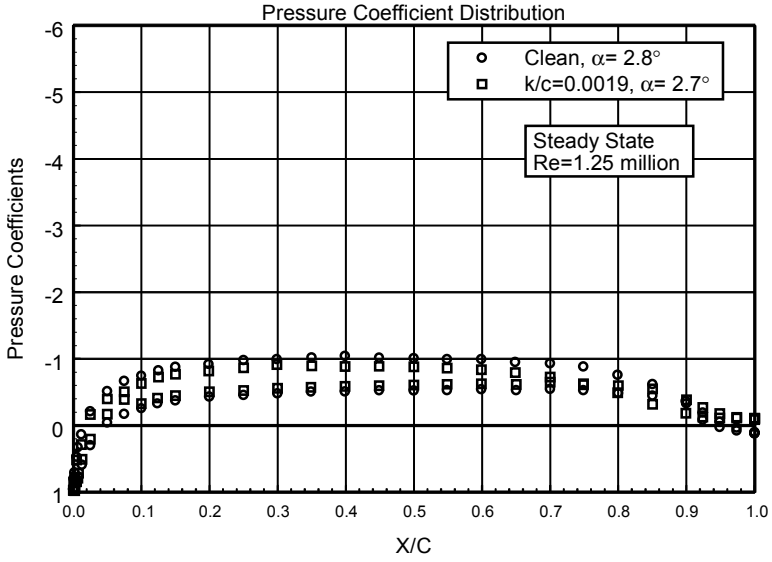

Figure 81. α = 2.8°

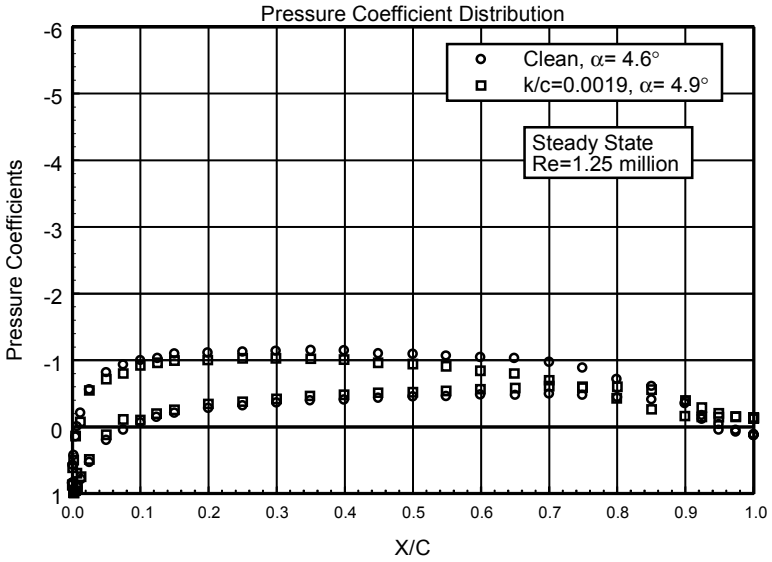

Figure 82. α = 4.6°

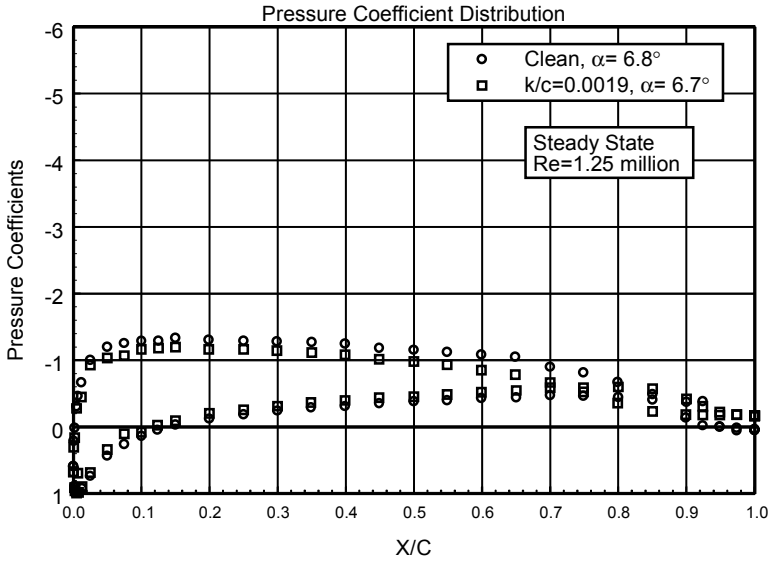

Figure 83. α = 6.8°

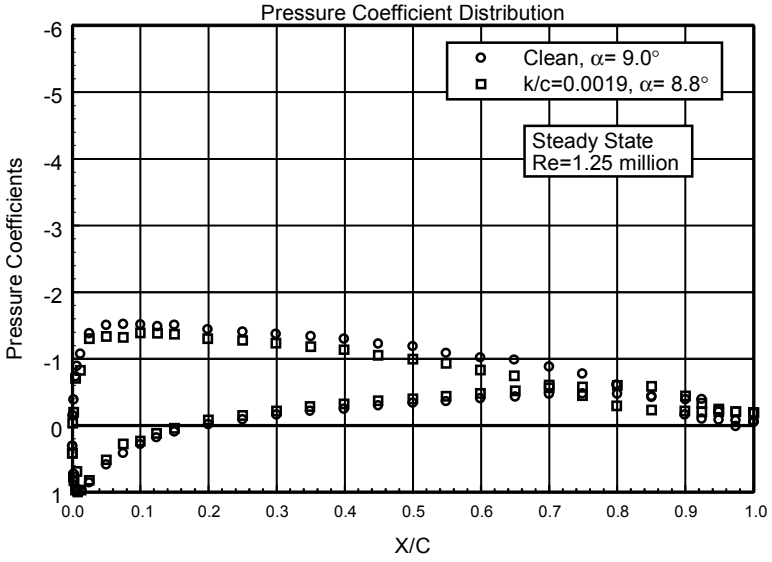

Figure 84. α = 9.0°

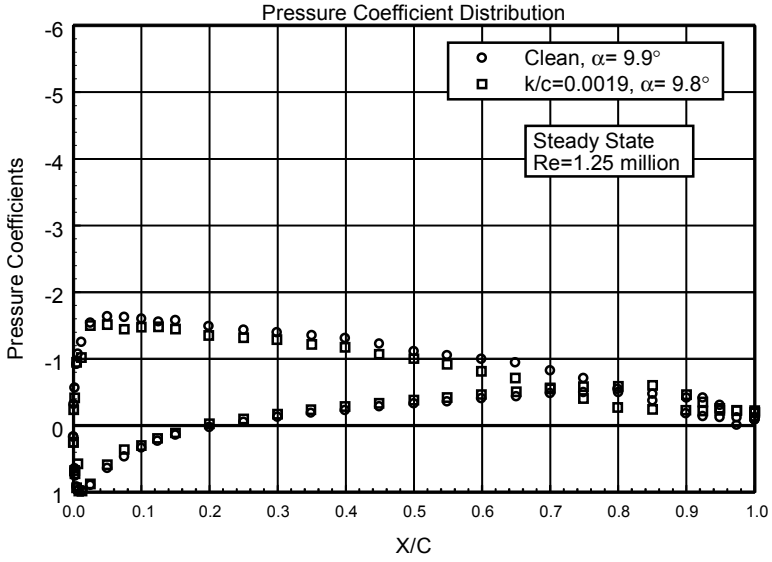

Figure 85. α = 9.9°

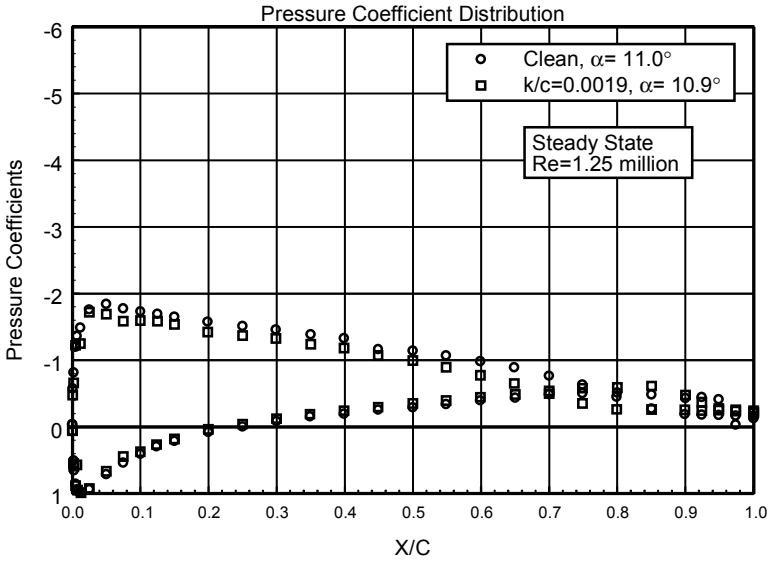

Figure 86. α = 11.0°

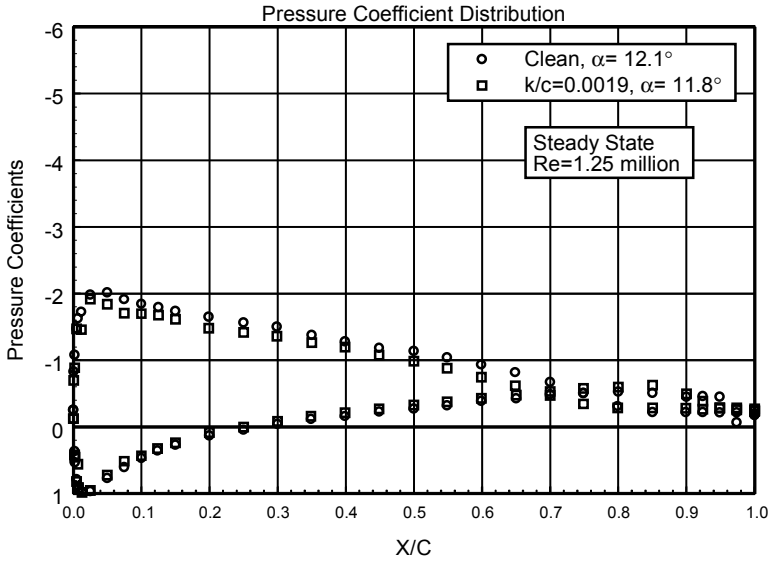

Figure 87. α = 12.1°

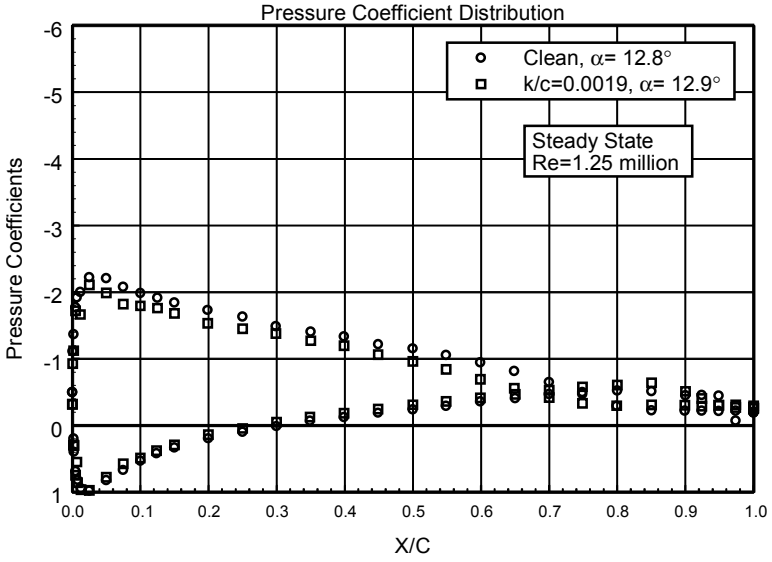

Figure 88. α = 12.8°

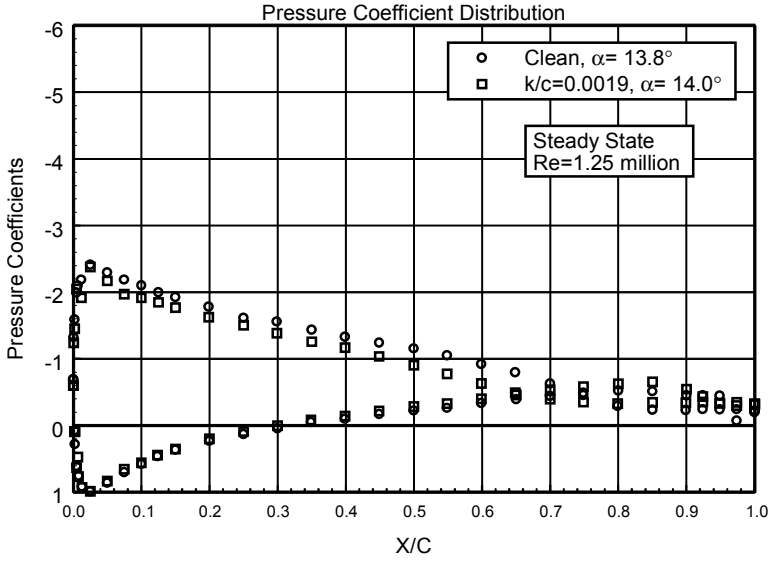

Figure 89. α = 13.8°

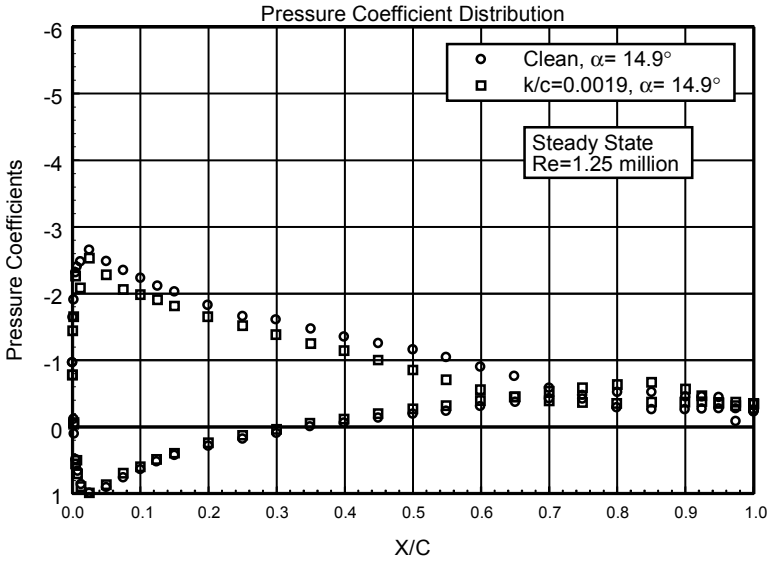

Figure 90. α = 14.9°

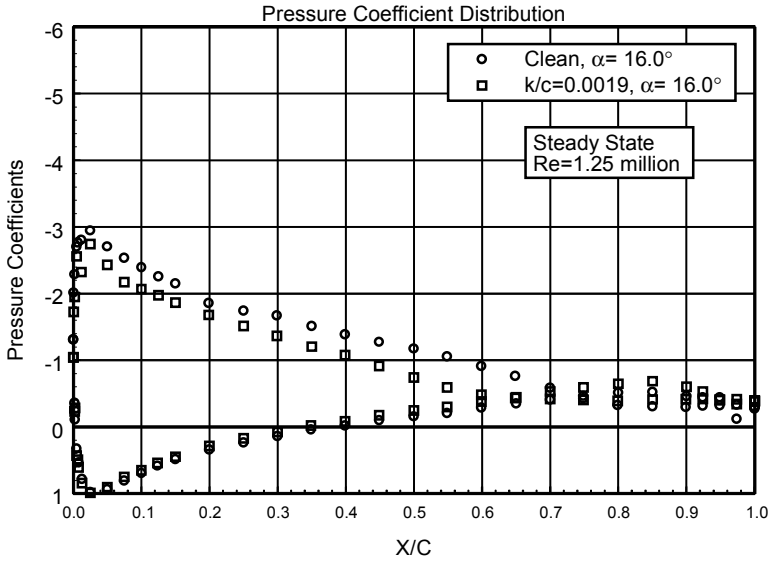

Figure 91. α = 16.0°

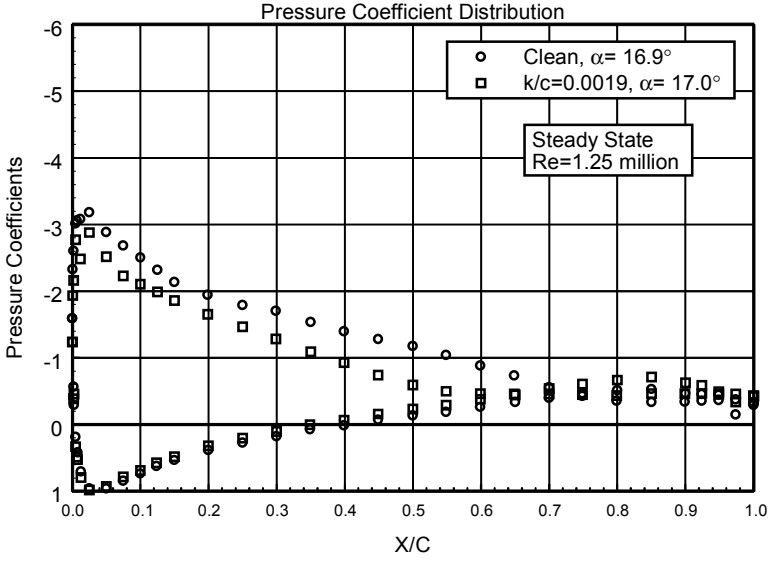

Figure 92. α = 16.9°

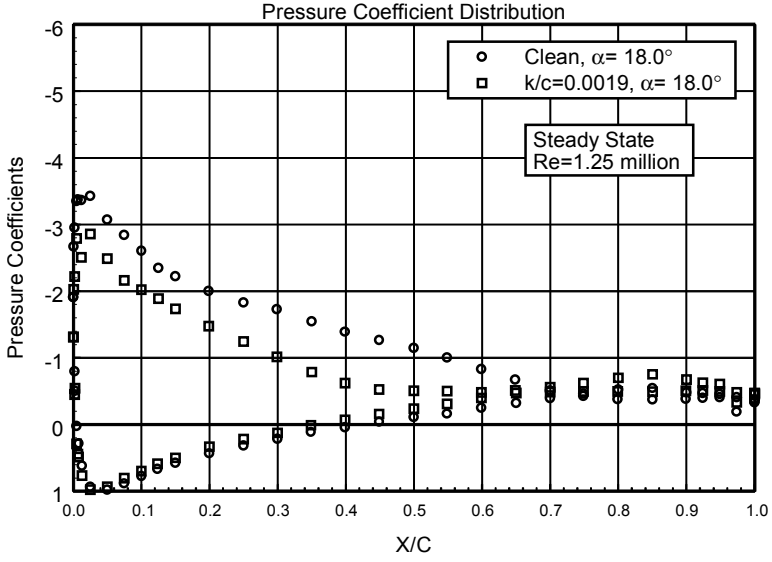

Figure 93. α = 18.0°

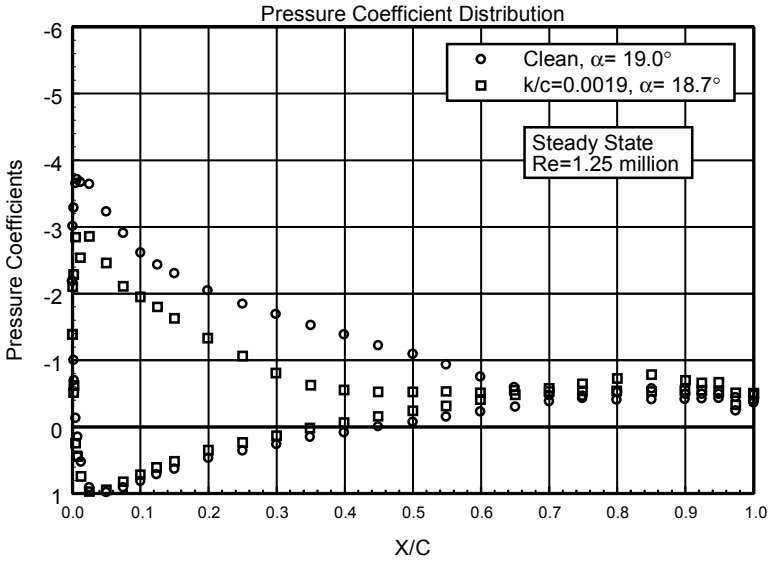

Figure 94. α = 19.0°

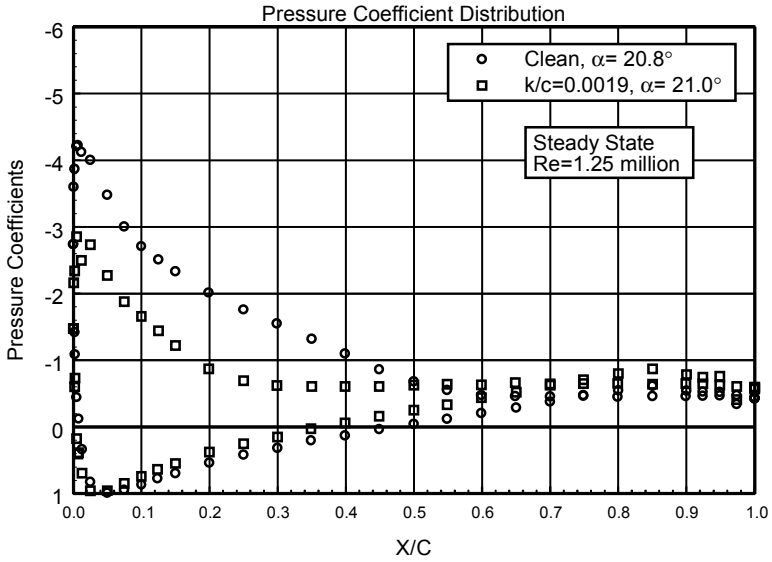

Figure 95. α = 20.8°

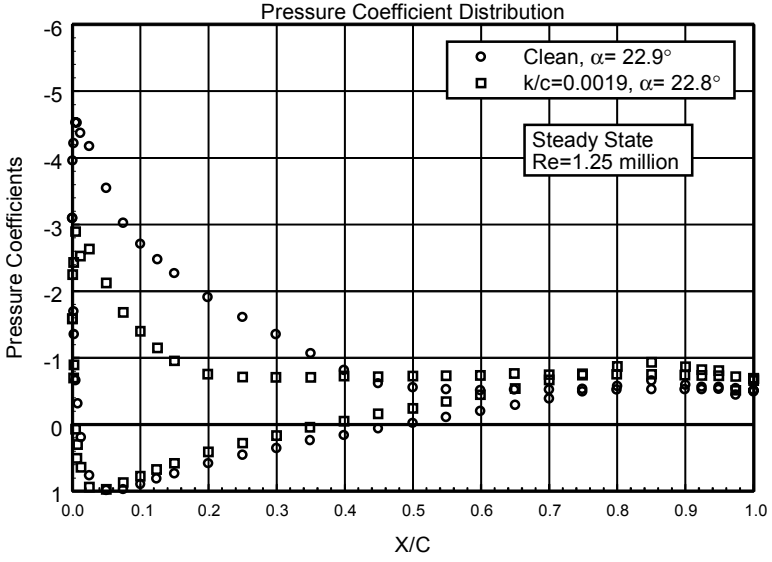

Figure 96. α = 22.9°

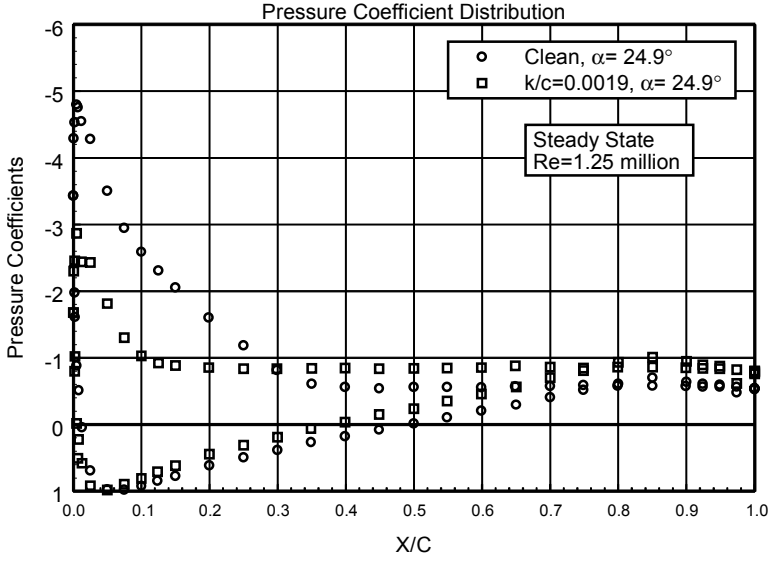

Figure 97. α = 24.9°

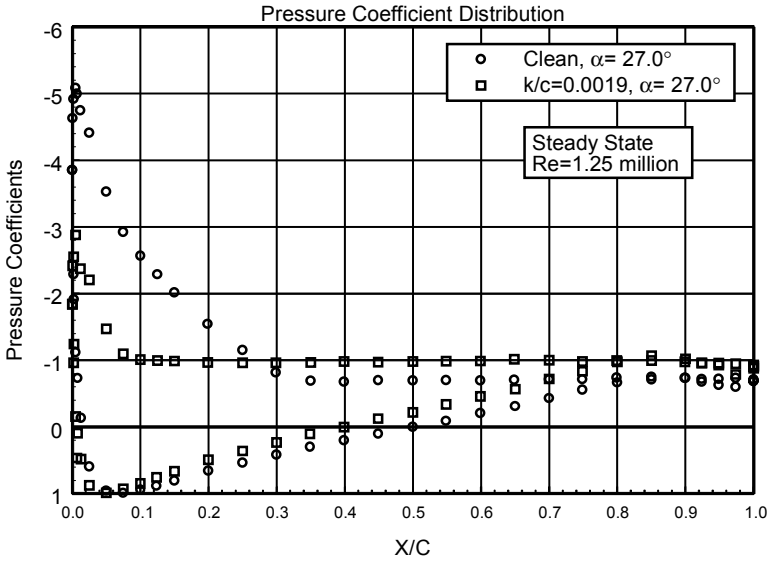

Figure 98. α = 27.0°

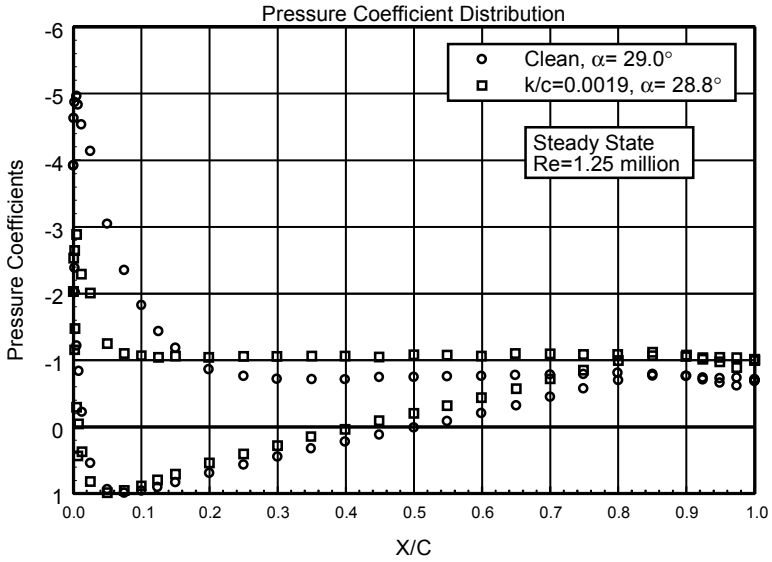

Figure 99. α = 29.0°

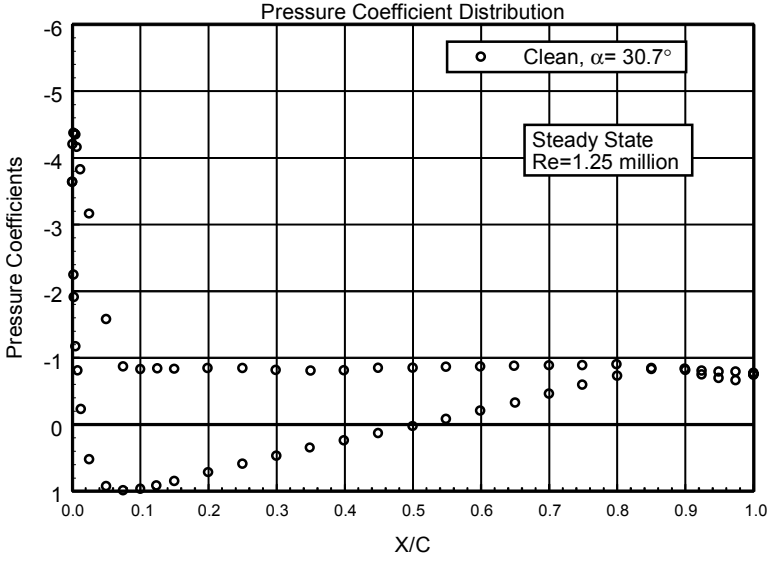

Figure 100. α = 30.7°

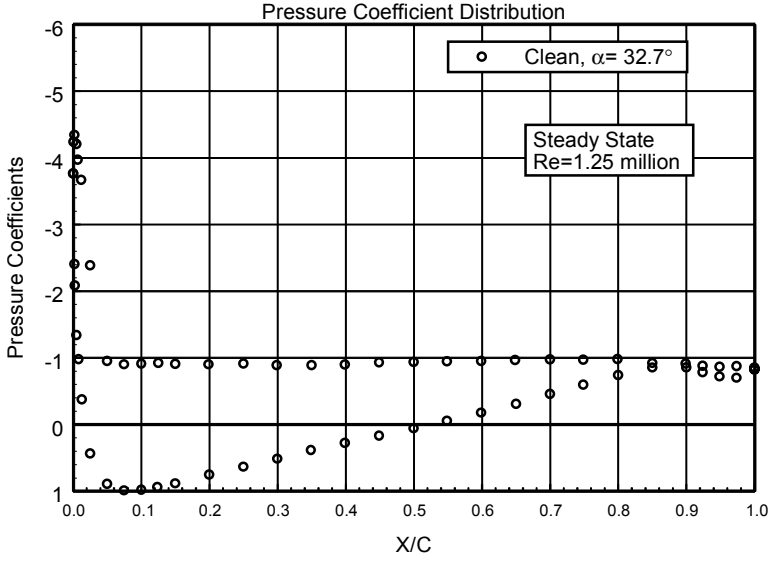

Figure 101. α = 32.7°

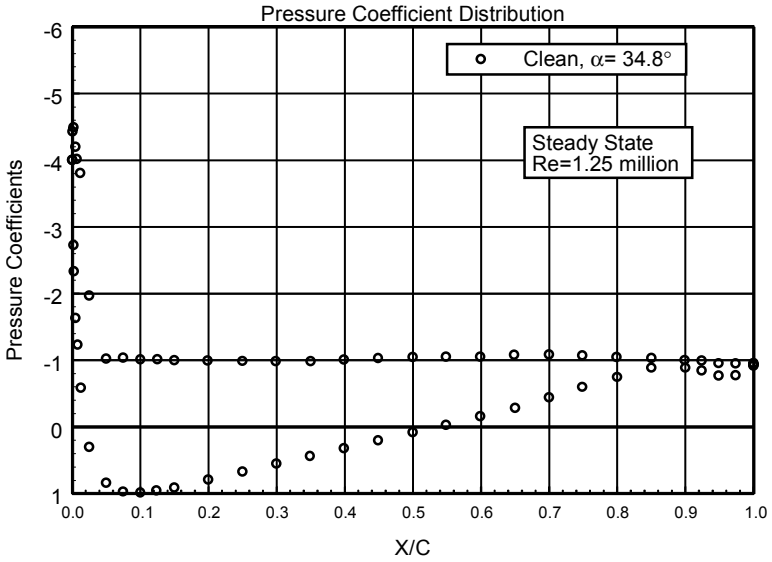

Figure 102. α = 34.8°

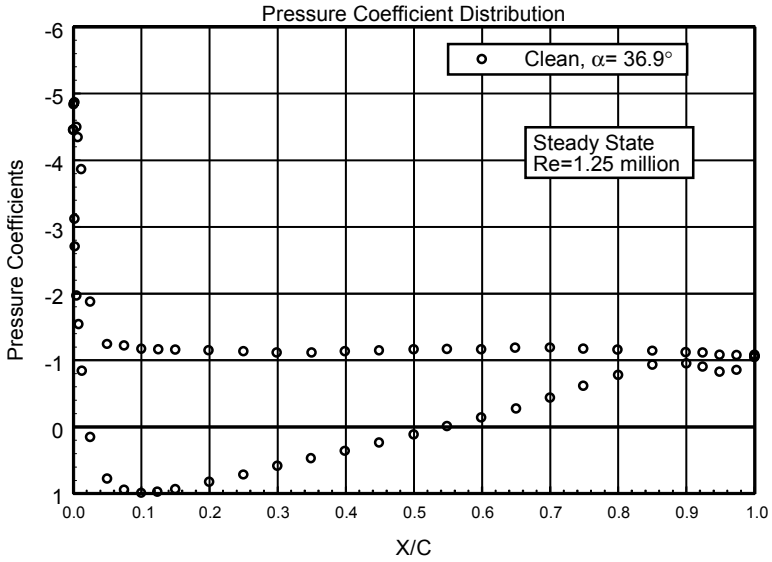

Figure 103. α = 36.9°

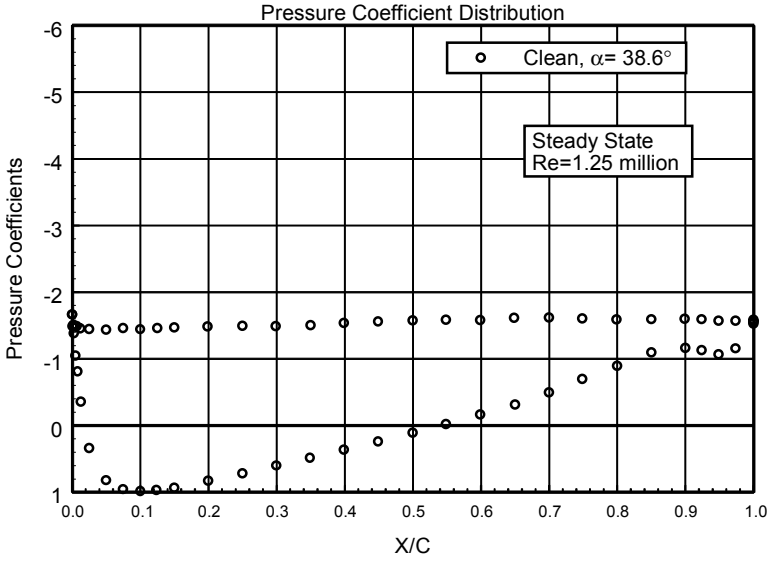

Figure 104. α = 38.6°

Appendix C: Unsteady Integrated Coefficients

List of Figures Page

Unsteady Airfoil Characteristics

±5.5° Sine, Re = 0.75 million

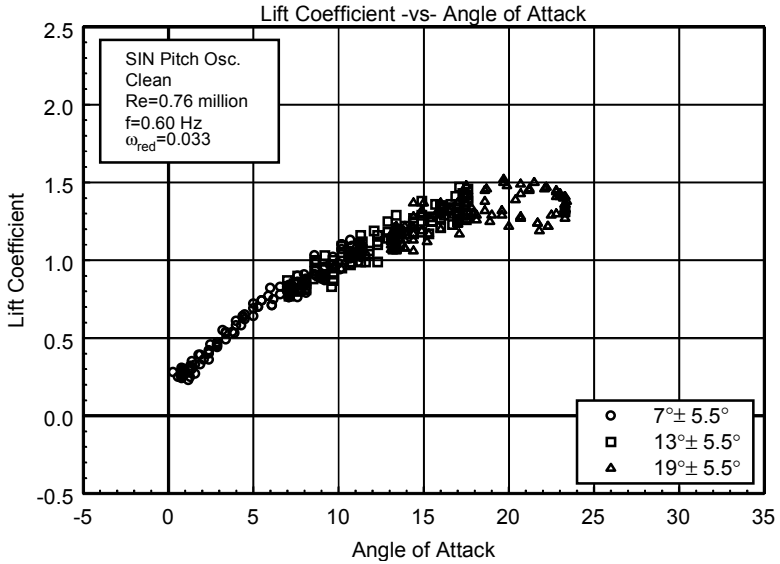

Figure C1. Lift coefficient vs α.

L303
Clean
Re=0.76 million
$\omega_{reduced}$=0.033

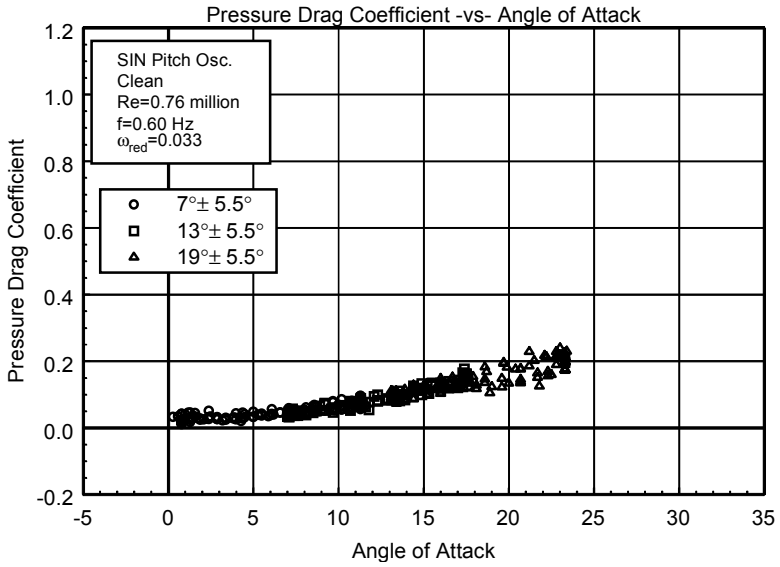

Figure C2. Pressure drag coefficient vs α.

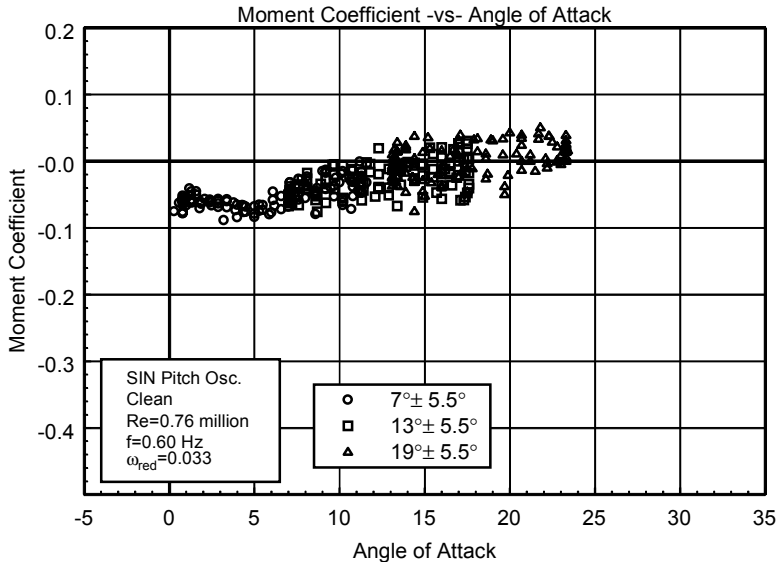

Figure C3. Moment coefficient vs α.

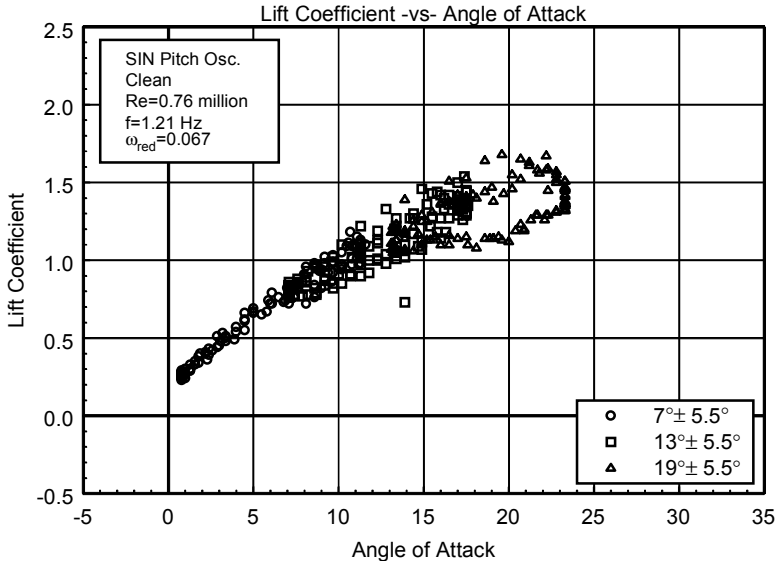

Figure C4. Lift coefficient vs α.

L303
Clean
Re=0.76 million
$\omega_{reduced}$=0.067

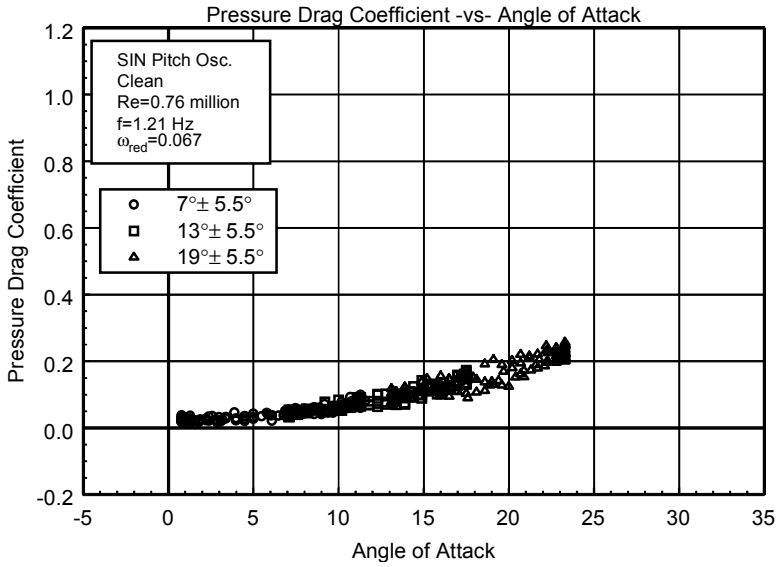

Figure C5. Pressure drag coefficient vs α.

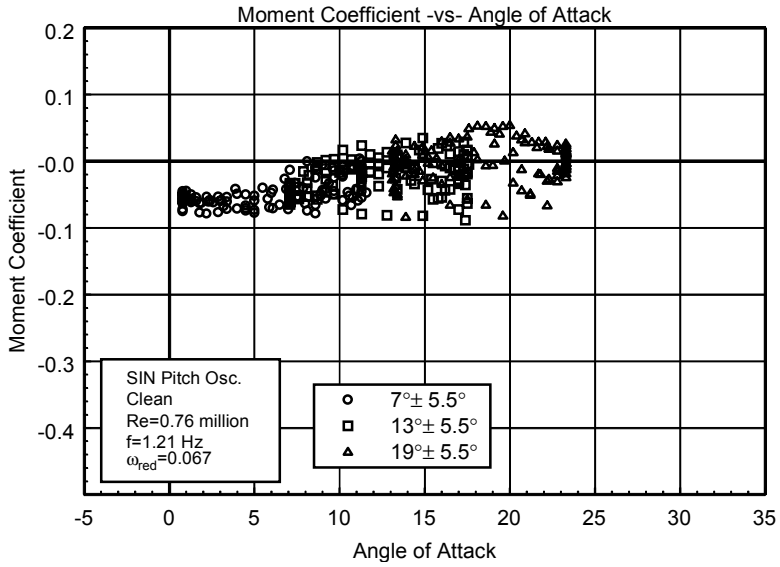

Figure C6. Moment coefficient vs α.

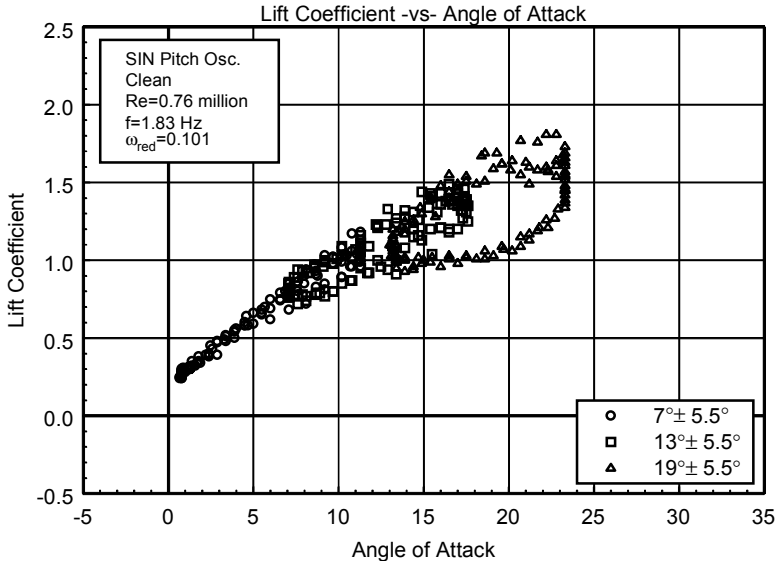

Figure C7. Lift coefficient vs α.

L303
Clean
Re=0.76 million
$\omega_{reduced}$=0.101

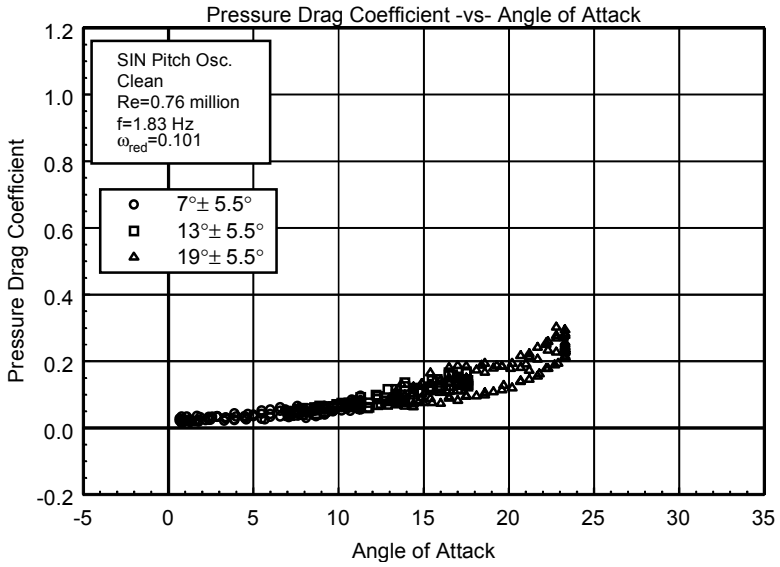

Figure C8. Pressure drag coefficient vs α.

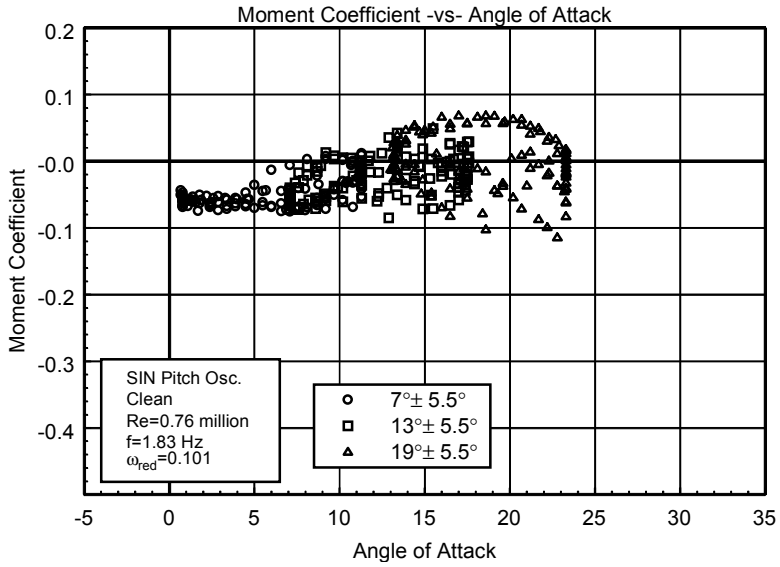

Figure C9. Moment coefficient vs α.

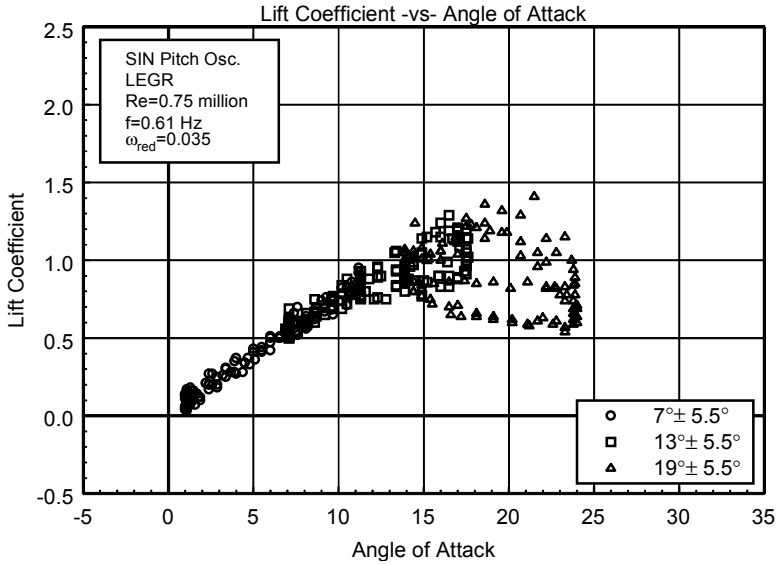

Figure C10. Lift coefficient vs α.

L303
LEGR
Re=0.75 million
$\omega_{reduced}$=0.035

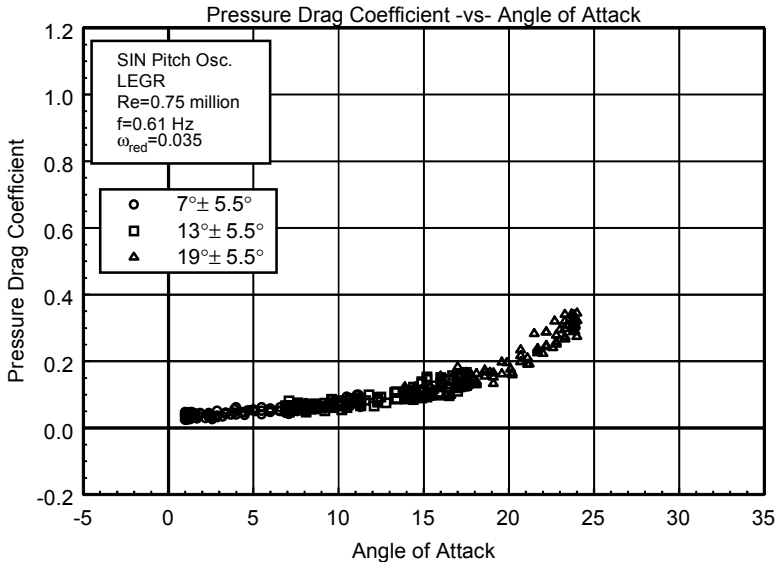

Figure C11. Pressure drag coefficient vs α.

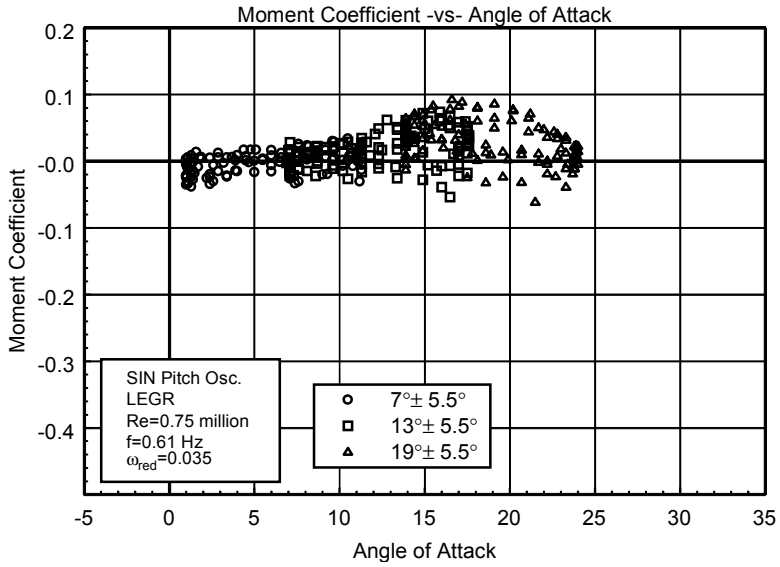

Figure C12. Moment coefficient vs α.

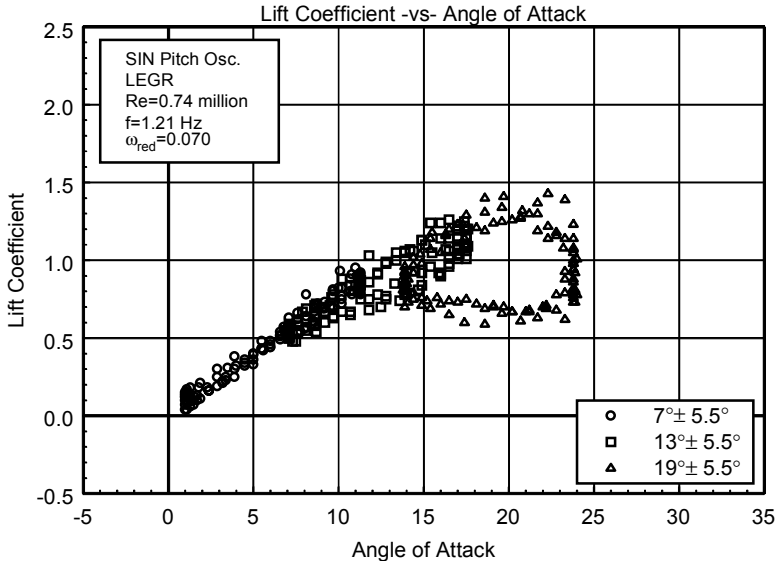

Figure C13. Lift coefficient vs α.

L303
LEGR
Re=0.74 million
$\omega_{reduced}$=0.070

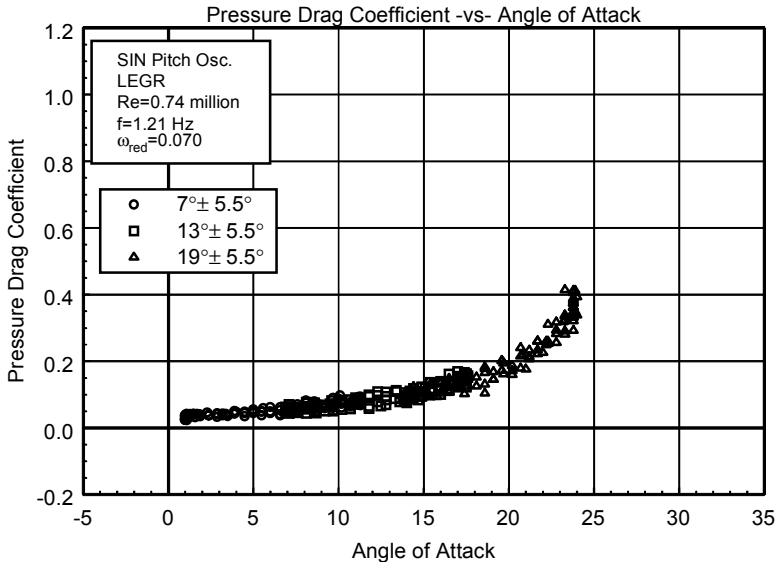

Figure C14. Pressure drag coefficient vs α.

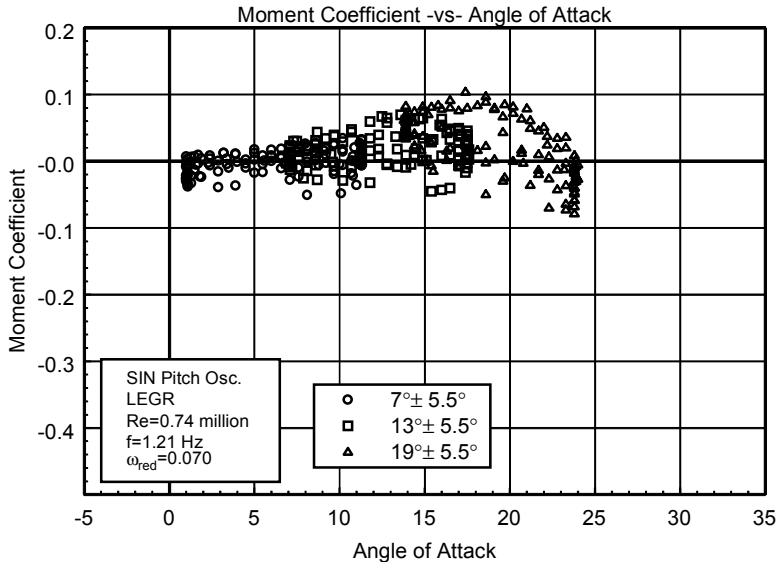

Figure C15. Moment coefficient vs α.

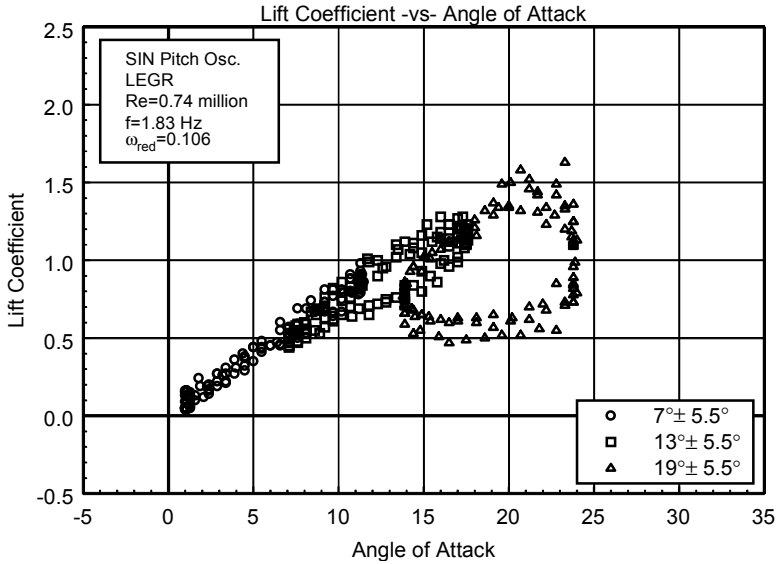

Figure C16. Lift coefficient vs α.

L303
LEGR
Re=0.74 million
$\omega_{reduced}$=0.106

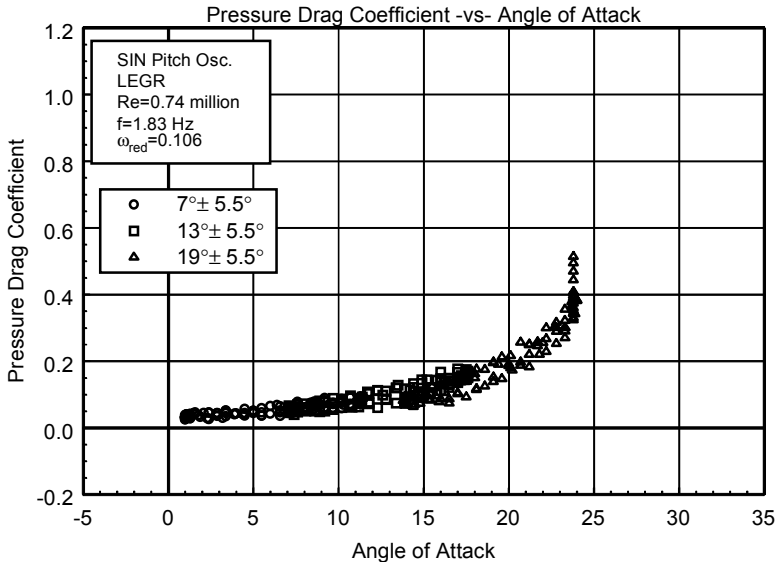

Figure C17. Pressure drag coefficient vs α.

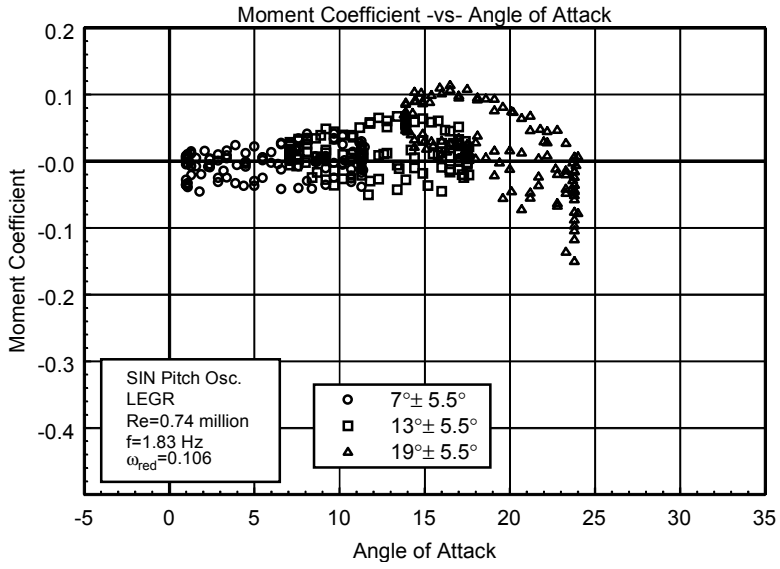

Figure C18. Moment coefficient vs α.

Unsteady Airfoil Characteristics

±5.5° Sine, Re = 1 million

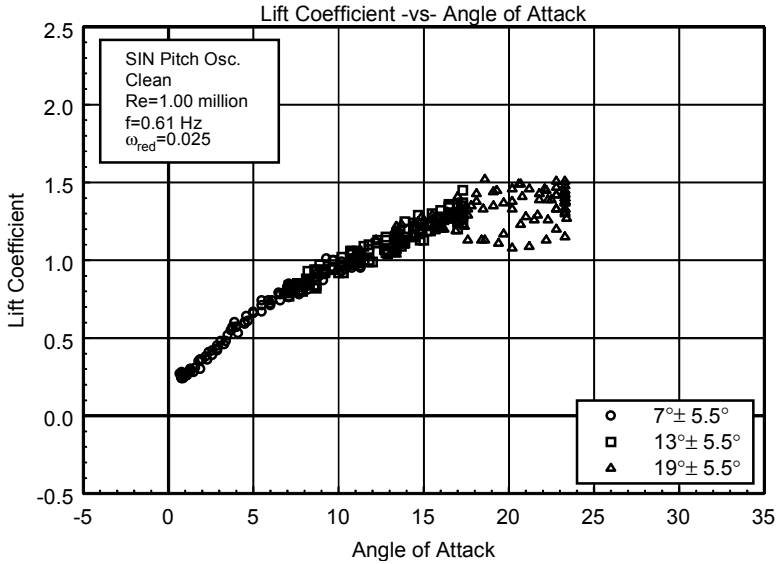

Figure C19. Lift coefficient vs α.

L303
Clean
Re=1.00 million
$\omega_{reduced}$=0.025

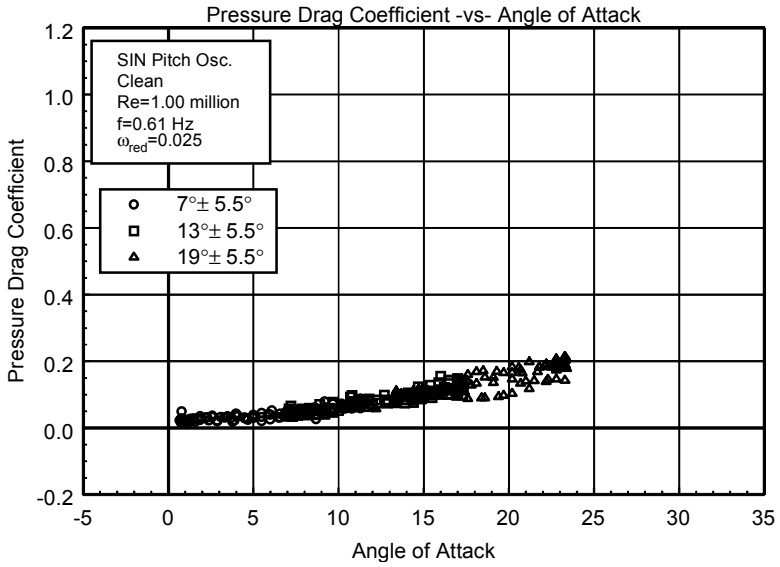

Figure C20. Pressure drag coefficient vs α.

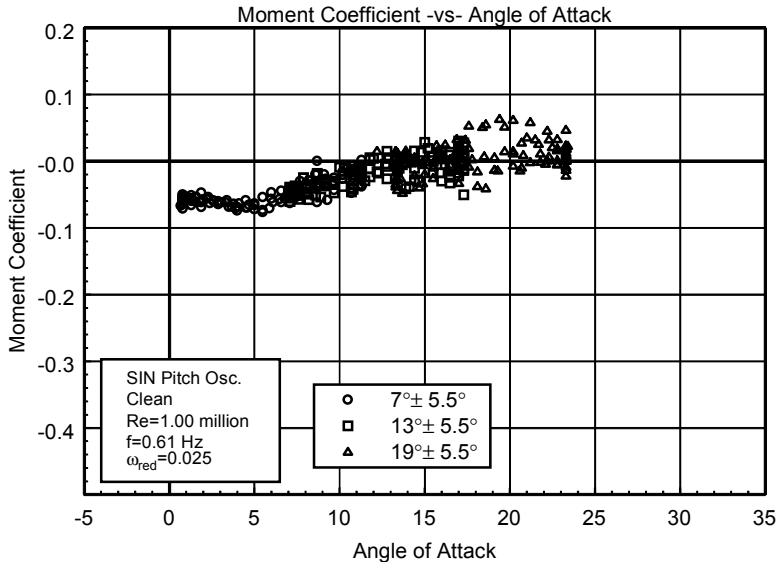

Figure C21. Moment coefficient vs α.

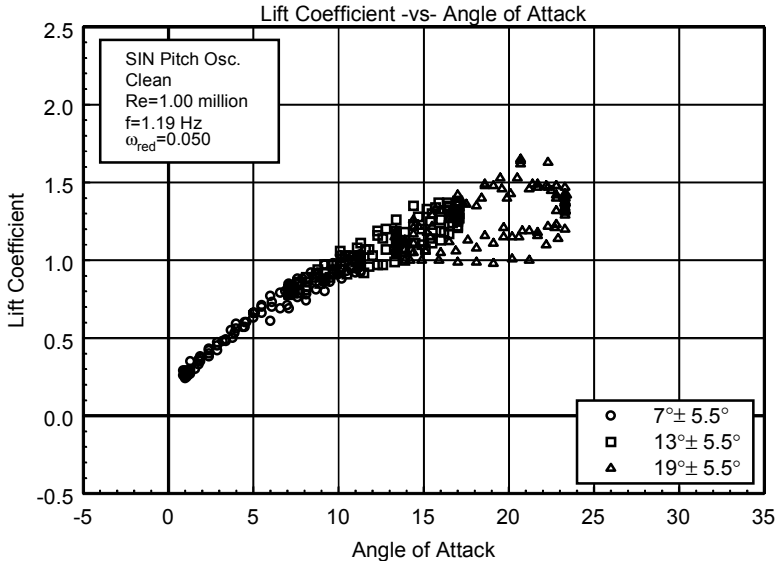

Figure C22. Lift coefficient vs α.

L303
Clean
Re=1.00 million
$\omega_{reduced}$=0.050

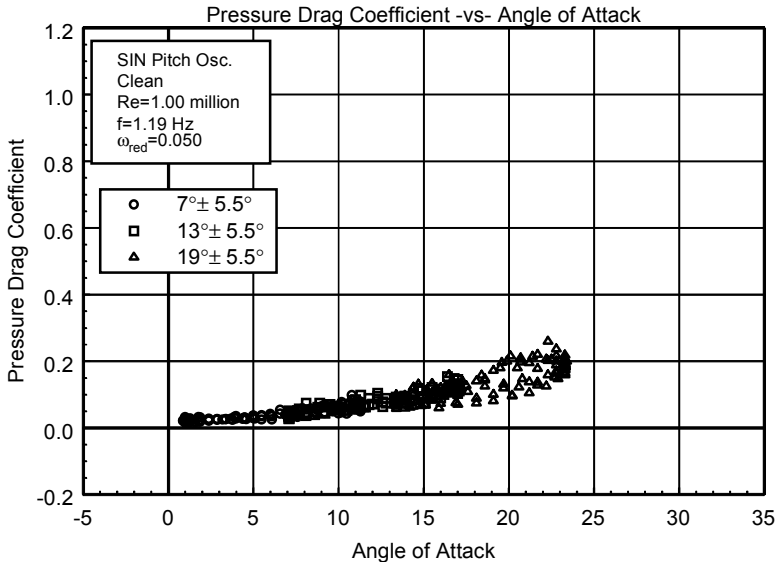

Figure C23. Pressure drag coefficient vs α.

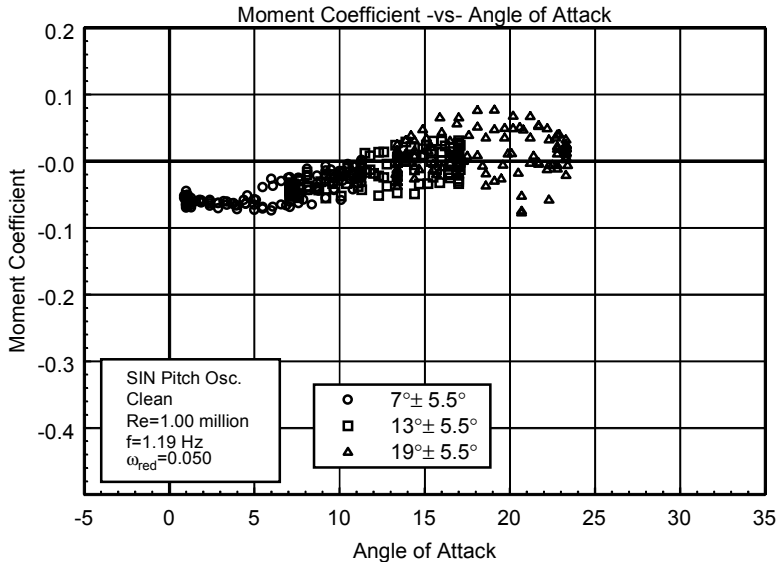

Figure C24. Moment coefficient vs α.

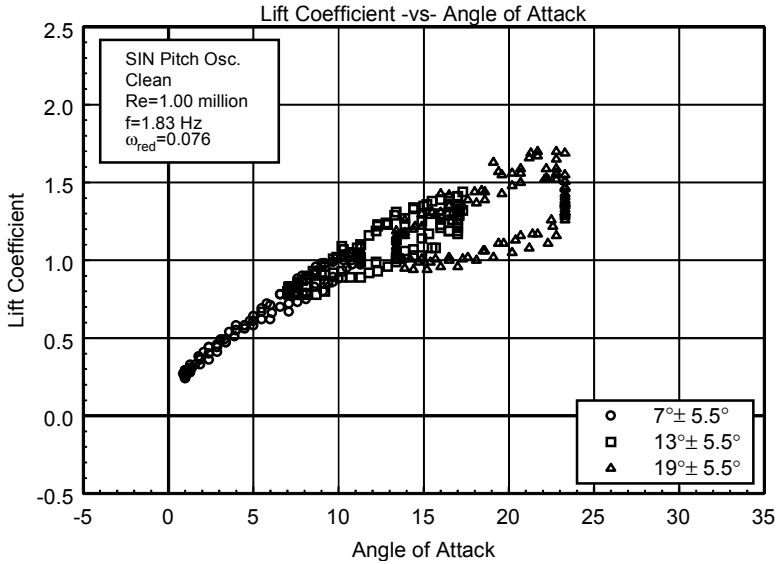

Figure C25. Lift coefficient vs α.

L303
Clean
Re=1.00 million
$\omega_{reduced}$=0.076

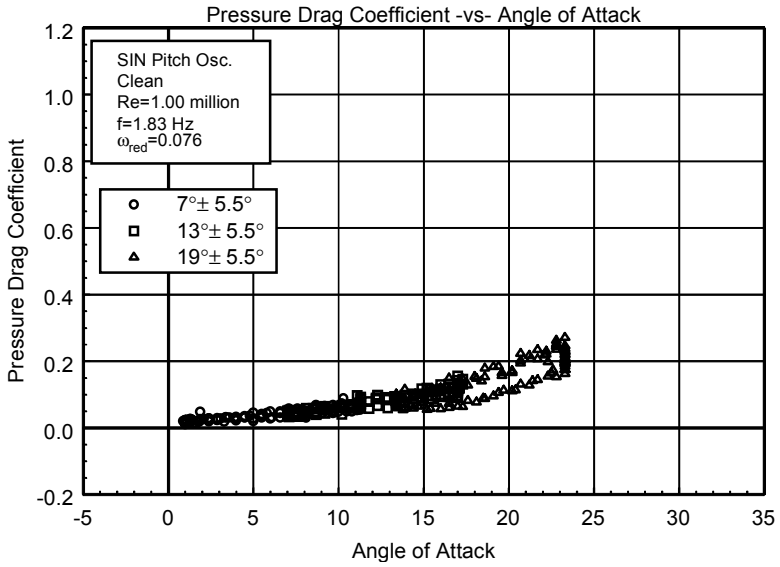

Figure C26. Pressure drag coefficient vs α.

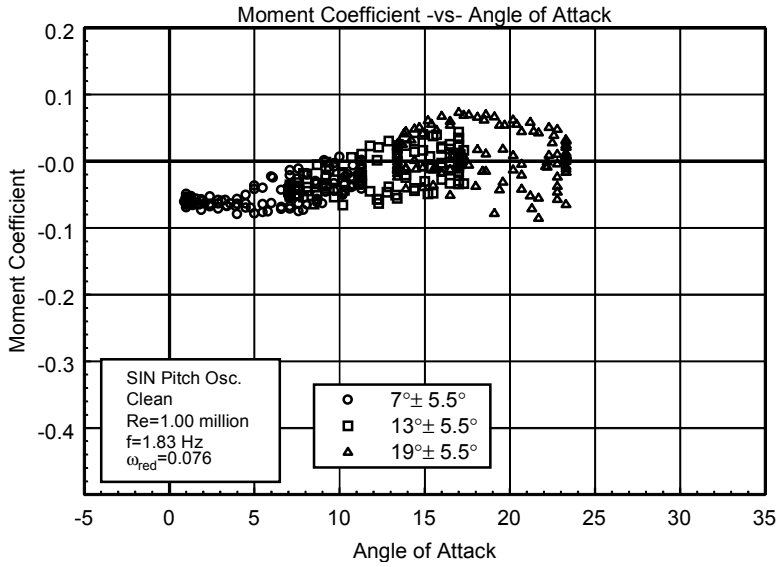

Figure C27. Moment coefficient vs α.

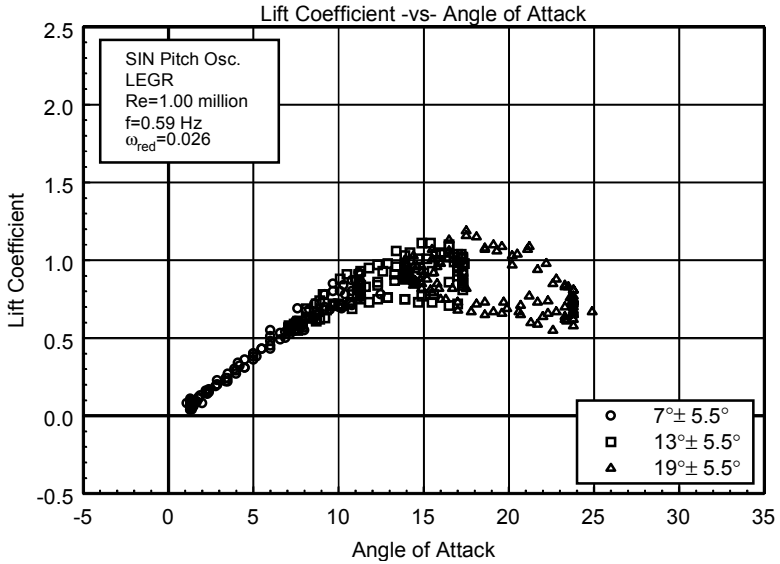

Figure C28. Lift coefficient vs α.

L303
LEGR
Re=1.00 million
$\omega_{reduced}$=0.026

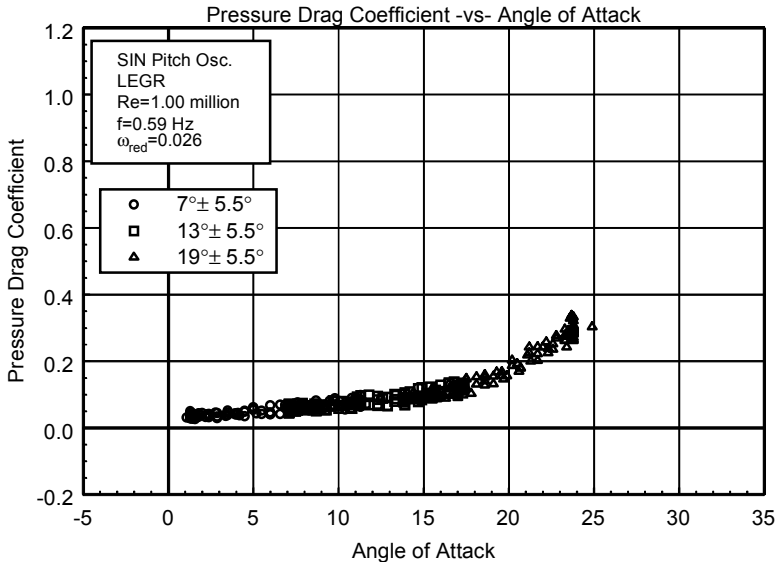

Figure C29. Pressure drag coefficient vs α.

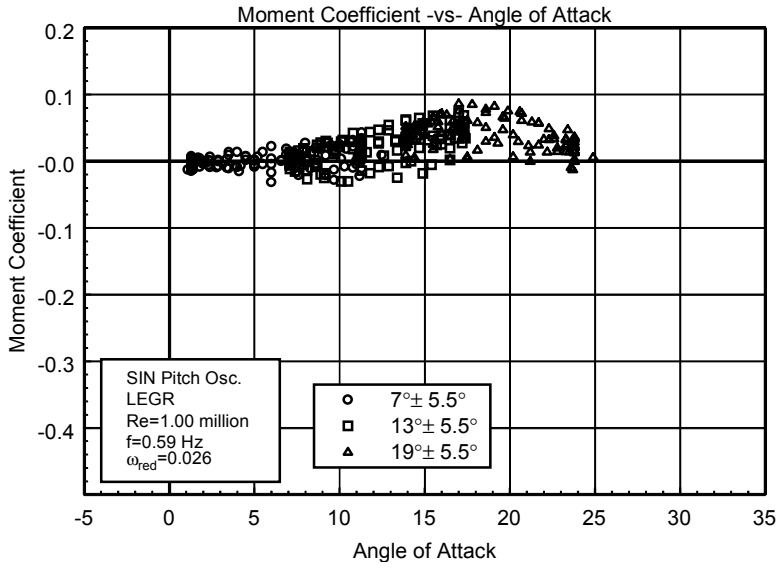

Figure C30. Moment coefficient vs α.

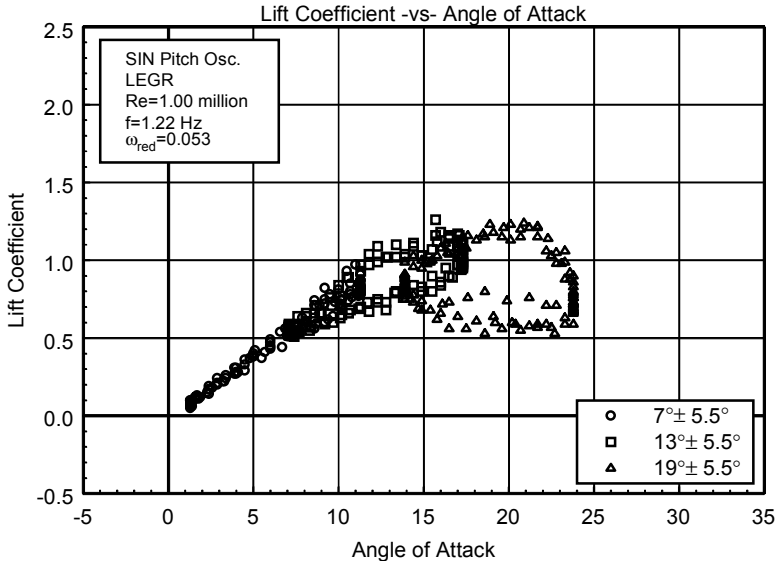

Figure C31. Lift coefficient vs α.

L303
LEGR
Re=1.00 million
$\omega_{reduced}$=0.053

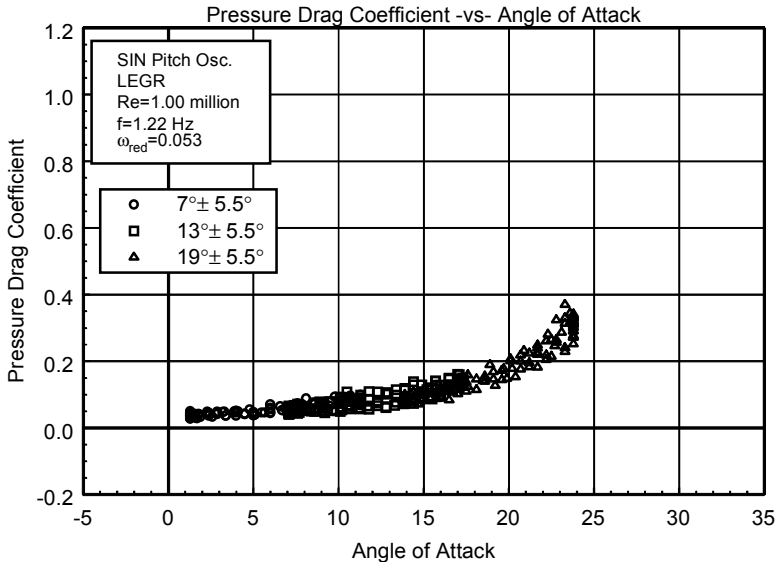

Figure C32. Pressure drag coefficient vs α.

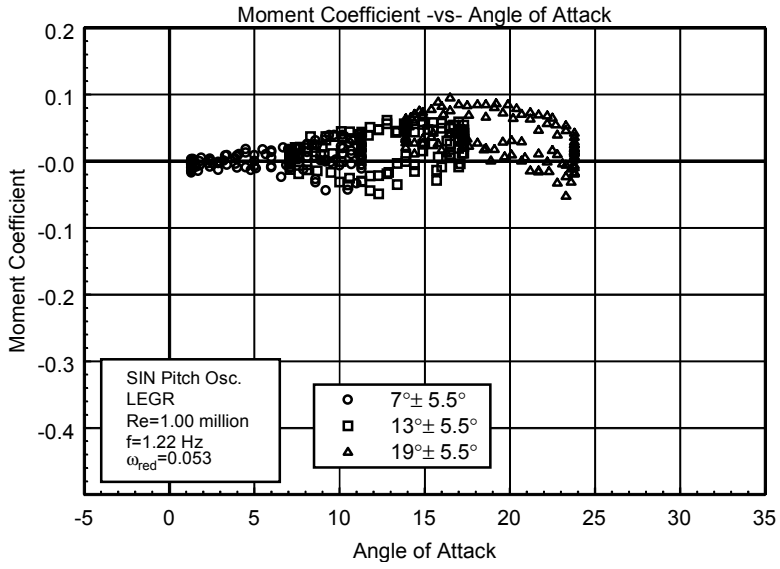

Figure C33. Moment coefficient vs α.

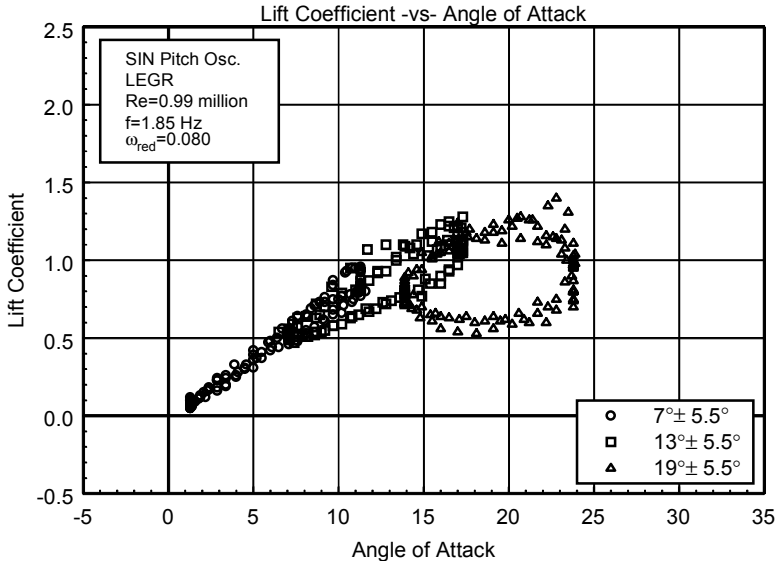

Figure C34. Lift coefficient vs α.

L303
LEGR
Re=0.99 million
$\omega_{reduced}$=0.080

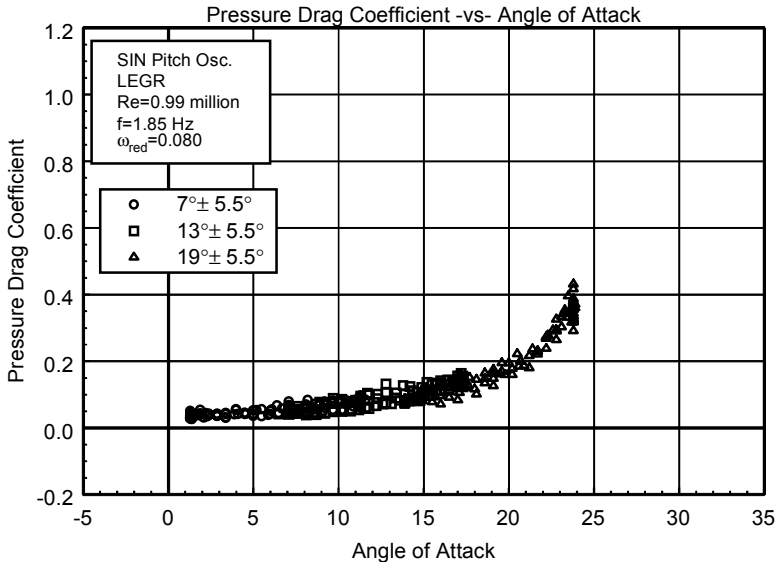

Figure C35. Pressure drag coefficient vs α.

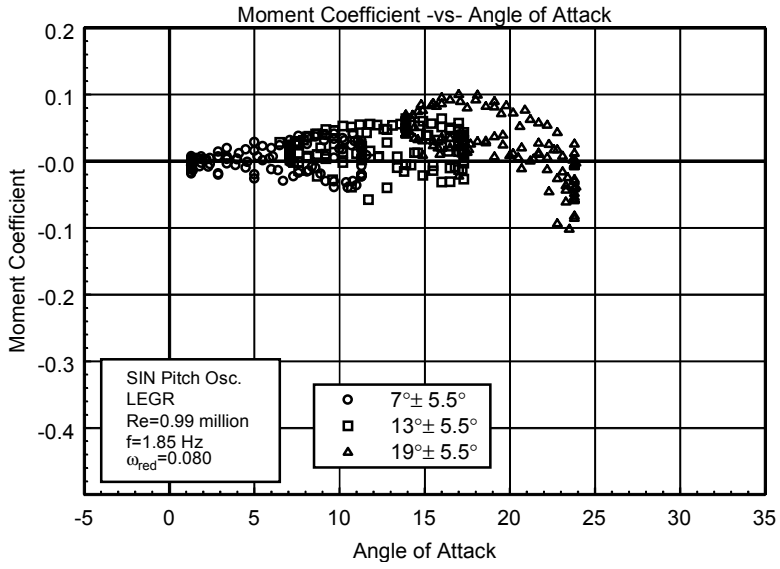

Figure C36. Moment coefficient vs α.

Unsteady Airfoil Characteristics

±5.5° Sine, Re= 1.25 million

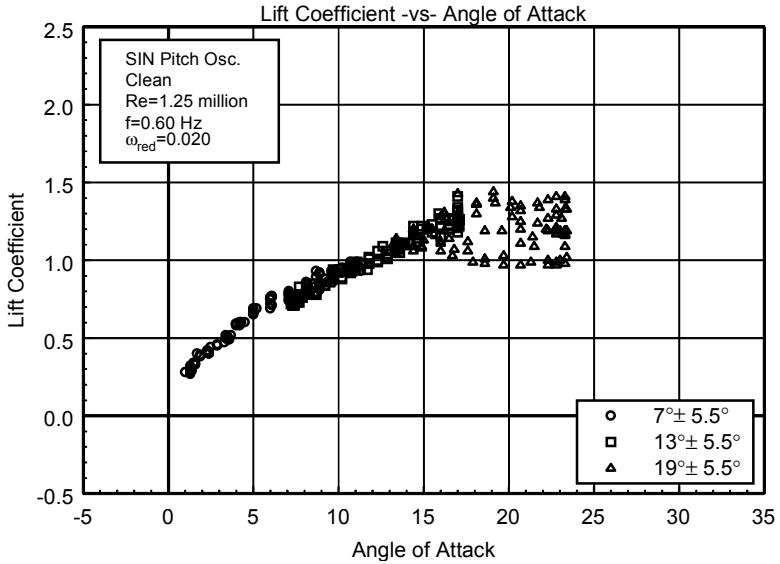

Figure C37. Lift coefficient vs α.

L303
Clean
Re=1.25 million
$\omega_{reduced}$=0.020

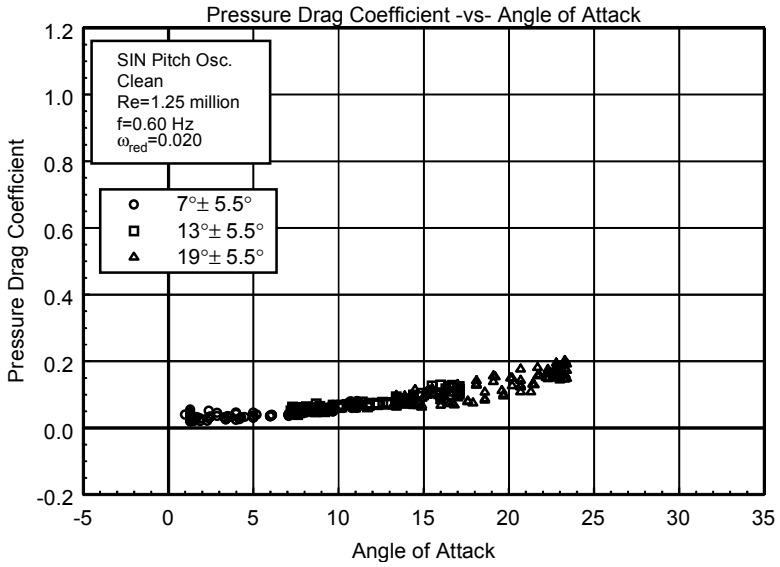

Figure C38. Pressure drag coefficient vs α.

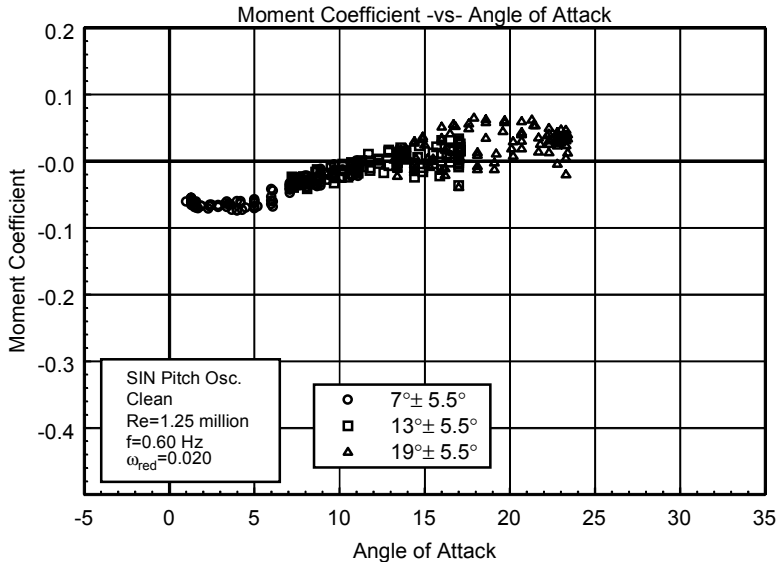

Figure C39. Moment coefficient vs α.

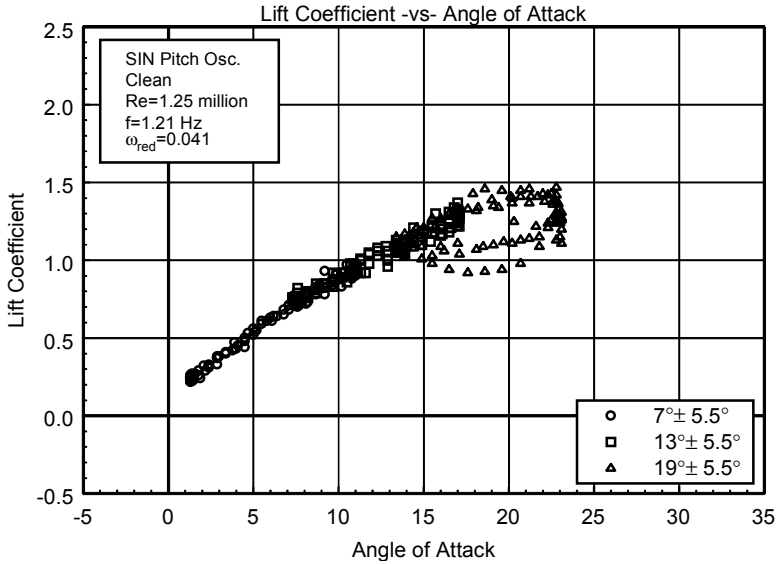

Figure C40. Lift coefficient vs α.

L303
Clean
Re=1.25 million
$\omega_{reduced}$=0.041

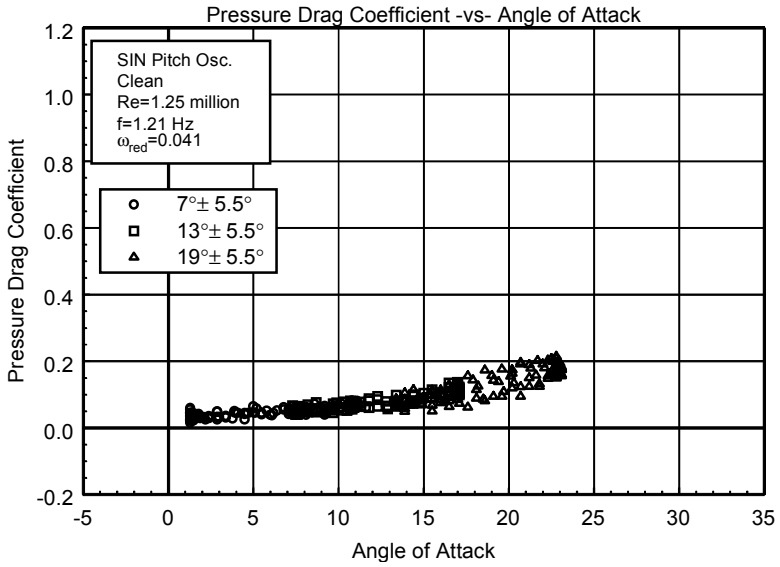

Figure C41. Pressure drag coefficient vs α.

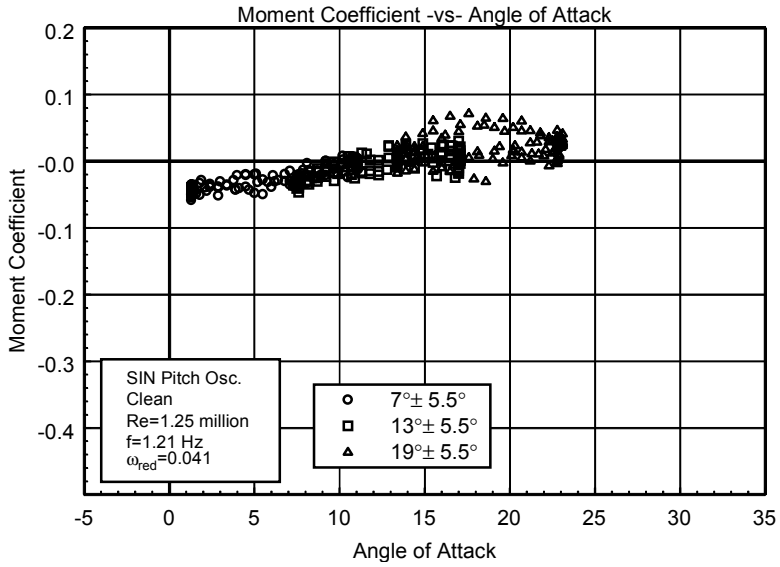

Figure C42. Moment coefficient vs α.

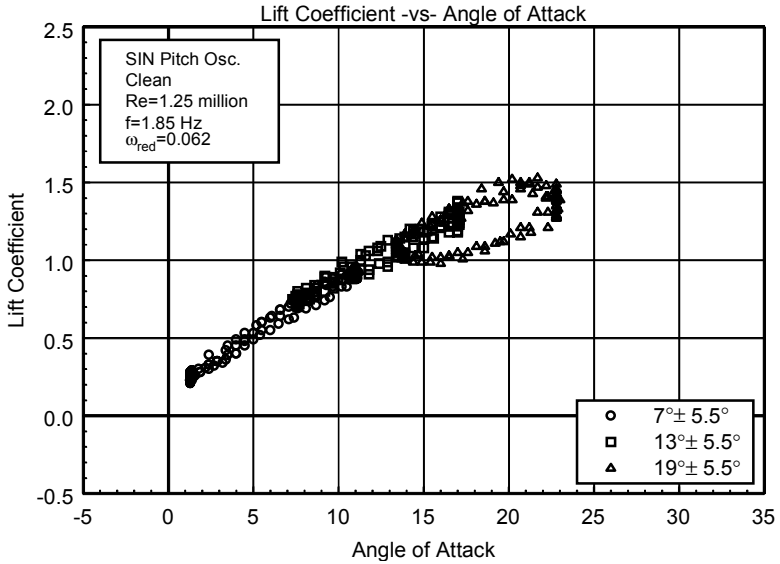

Figure C43. Lift coefficient vs α.

L303
Clean
Re=1.25 million
$\omega_{reduced}$=0.062

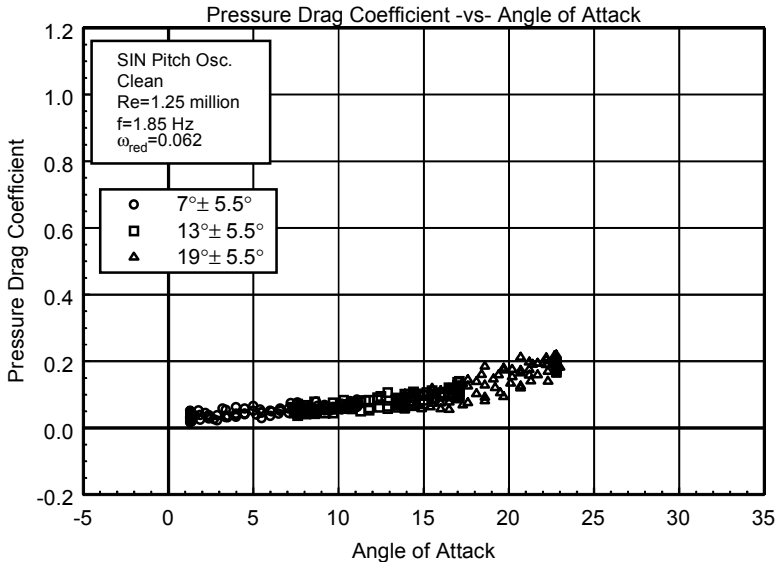

Figure C44. Pressure drag coefficient vs α.

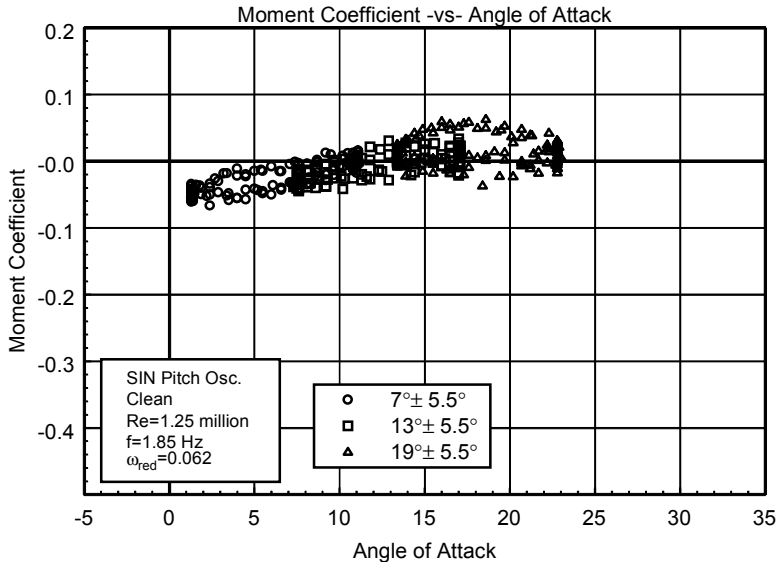

Figure C45. Moment coefficient vs α.

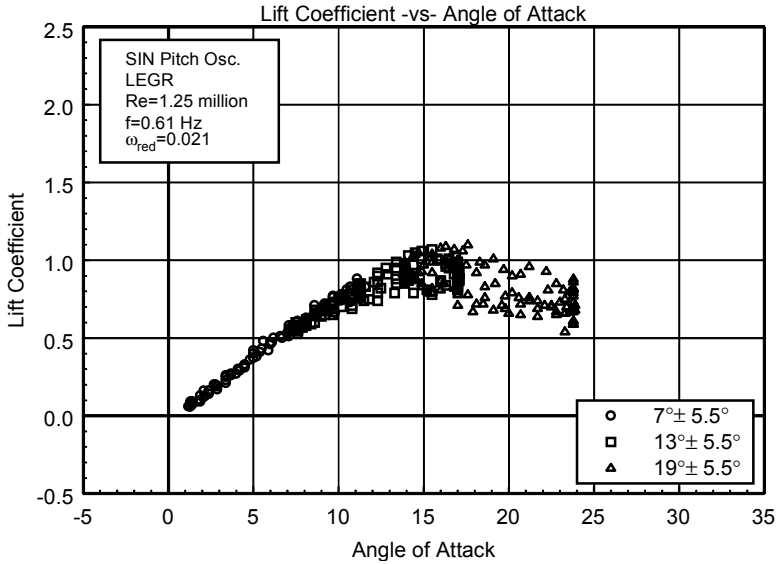

Figure C46. Lift coefficient vs α.

L303
LEGR
Re=1.25 million
$\omega_{reduced}$=0.021

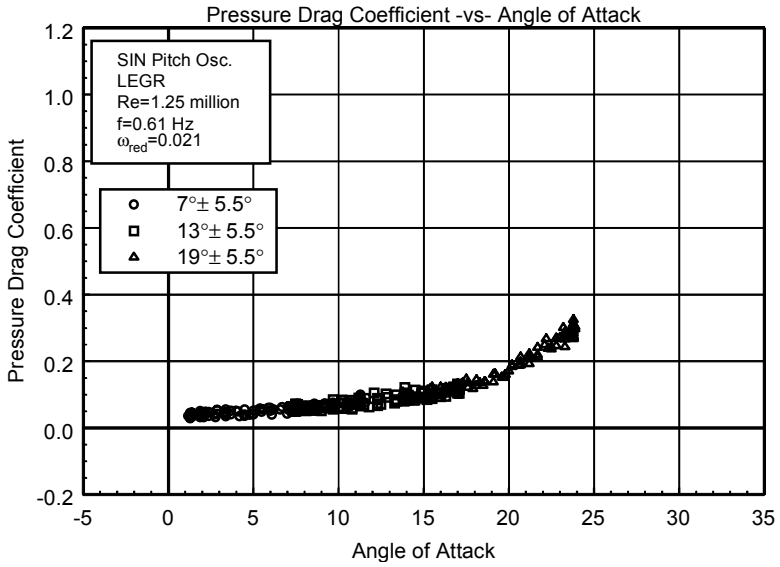

Figure C47. Pressure drag coefficient vs α.

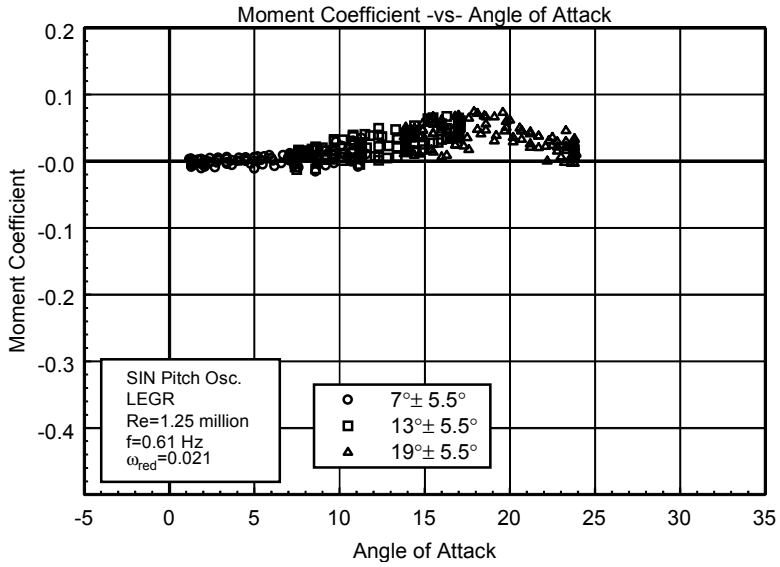

Figure C48. Moment coefficient vs α.

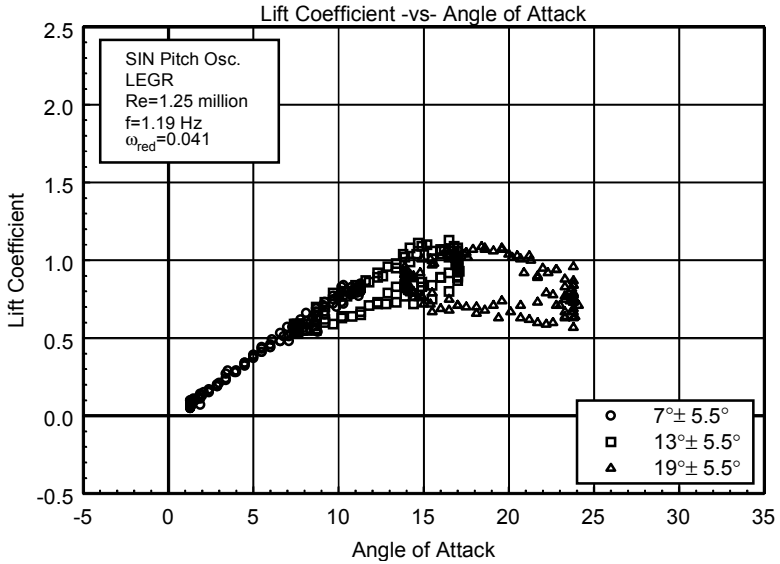

Figure C49. Lift coefficient vs α.

L303
LEGR
Re=1.25 million
$\omega_{reduced}$=0.041

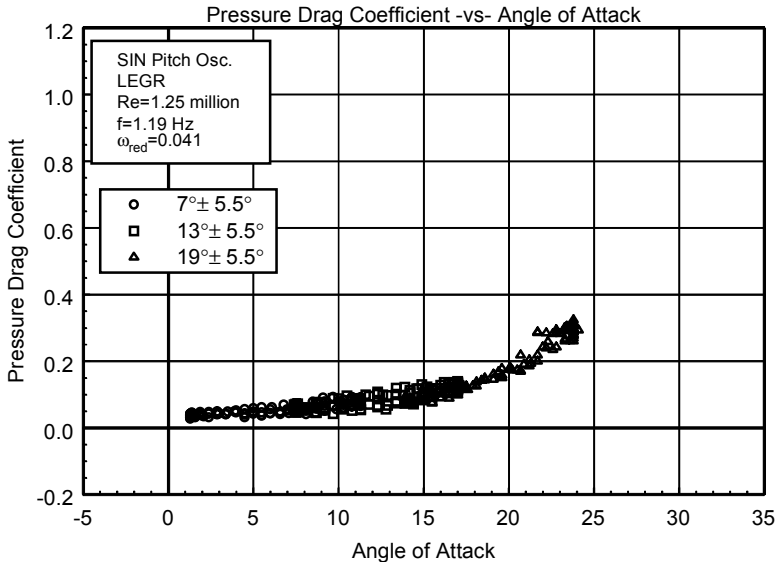

Figure C50. Pressure drag coefficient vs α.

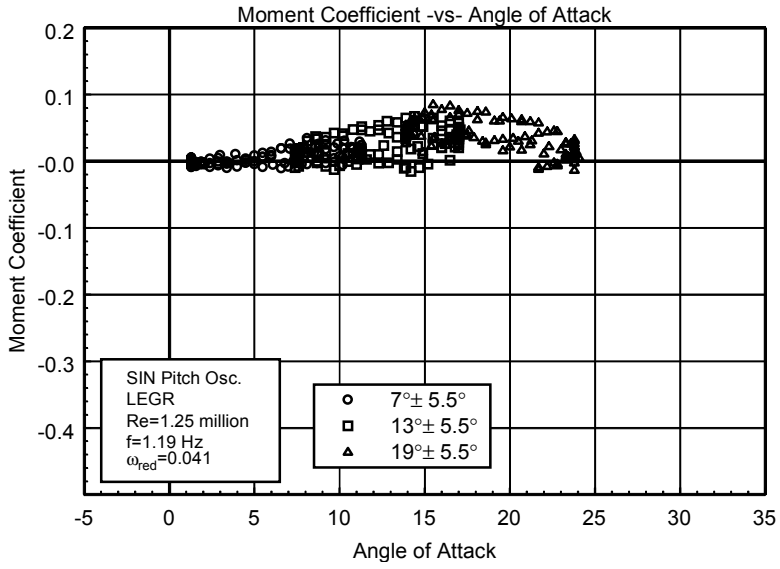

Figure C51. Moment coefficient vs α.

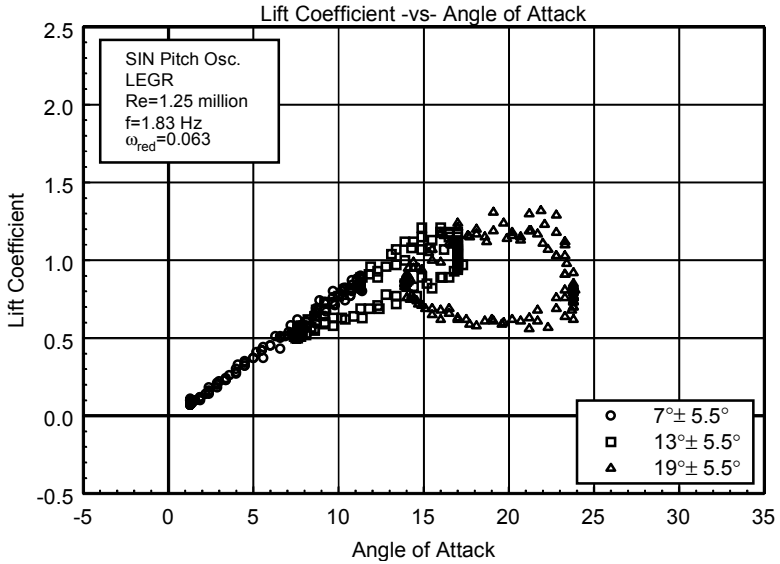

Figure C52. Lift coefficient vs α.

L303
LEGR
Re=1.25 million
$\omega_{reduced}$=0.063

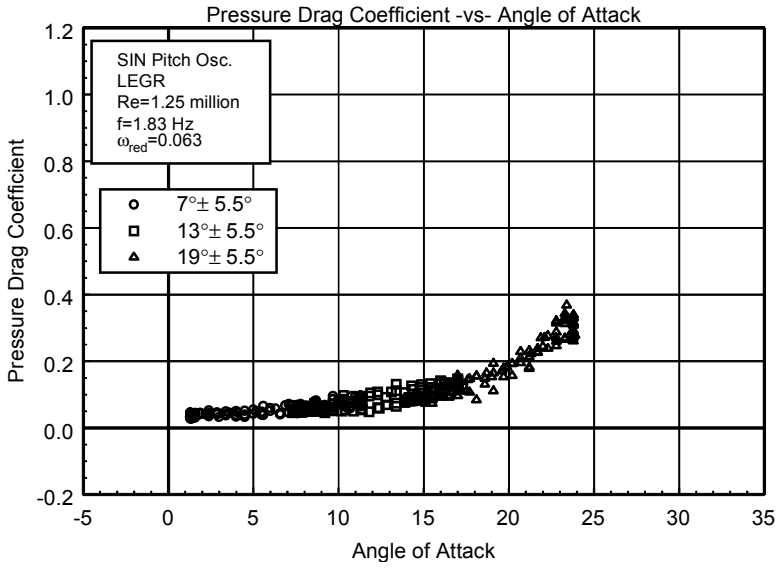

Figure C53. Pressure drag coefficient vs α.

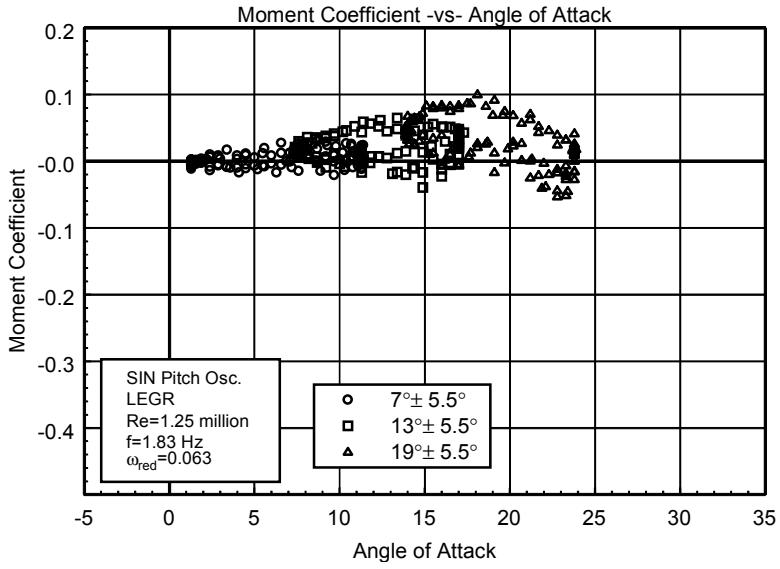

Figure C54. Moment coefficient vs α.

Unsteady Airfoil Characteristics

±10° Sine, Re = 0.75 million

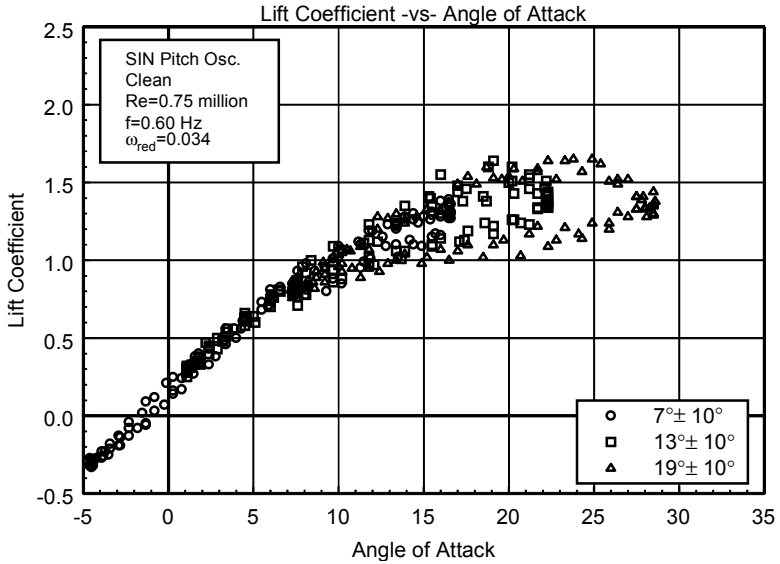

Figure C55. Lift coefficient vs α.

L303
Clean
Re=0.75 million
$\omega_{reduced}$=0.034

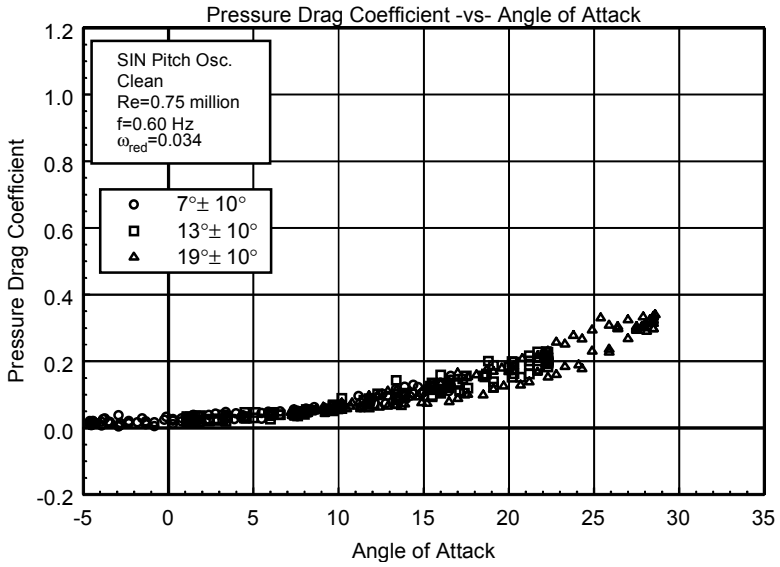

Figure C56. Pressure drag coefficient vs α.

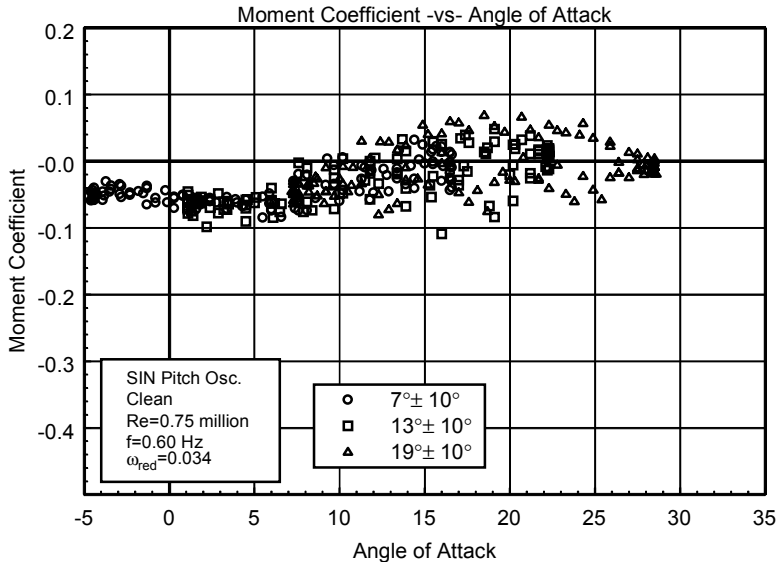

Figure C57. Moment coefficient vs α.

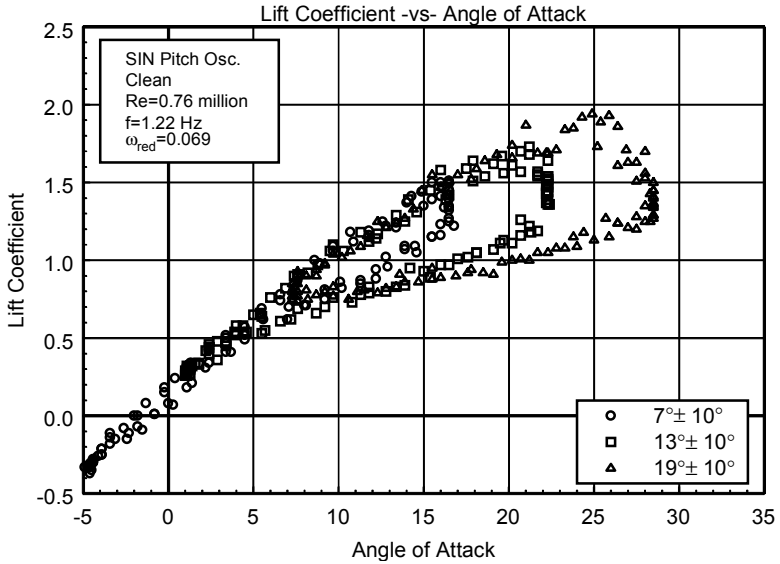

Figure C58. Lift coefficient vs α.

L303
Clean
Re=0.76 million
$\omega_{reduced}$=0.069

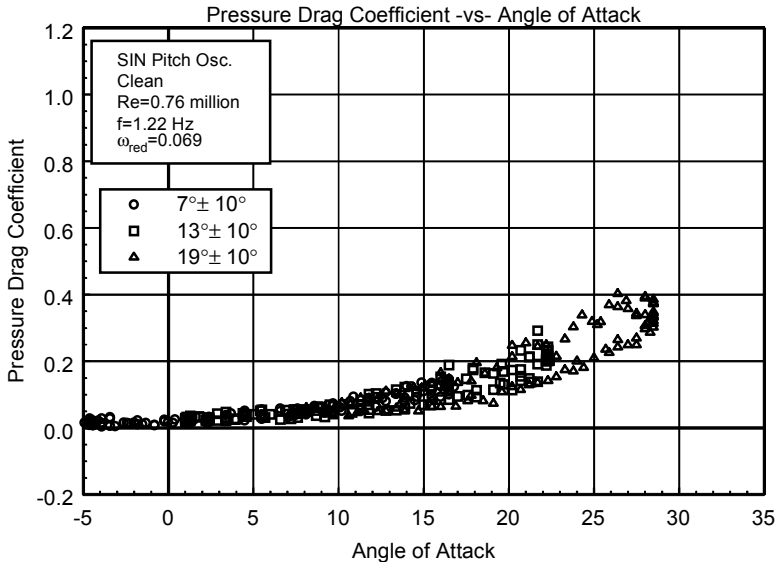

Figure C59. Pressure drag coefficient vs α.

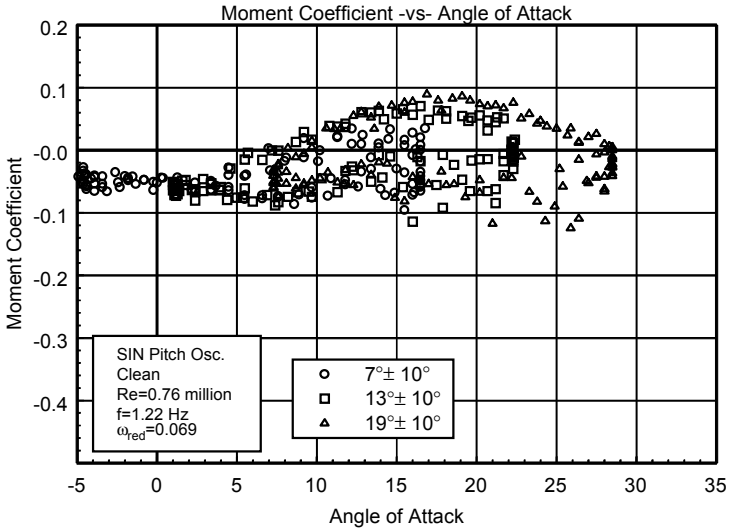

Figure C60. Moment coefficient vs α.

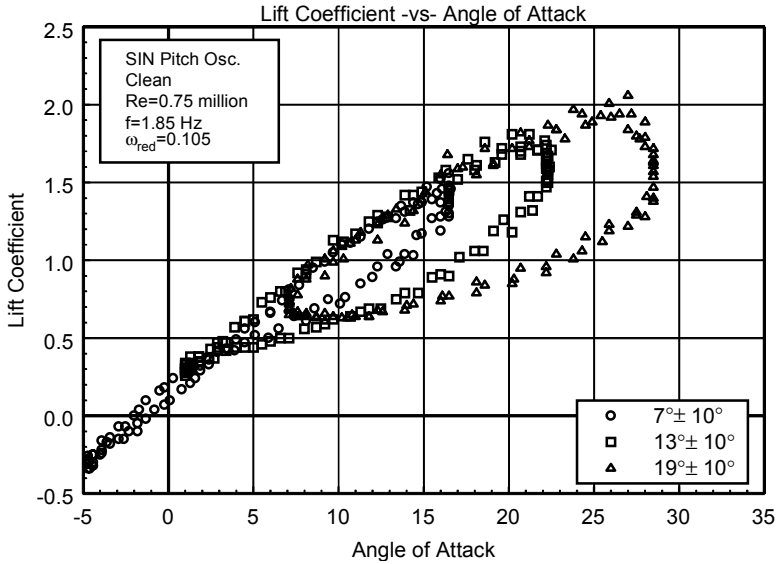

Figure C61. Lift coefficient vs α.

L303
Clean
Re=0.75 million
$\omega_{reduced}$=0.105

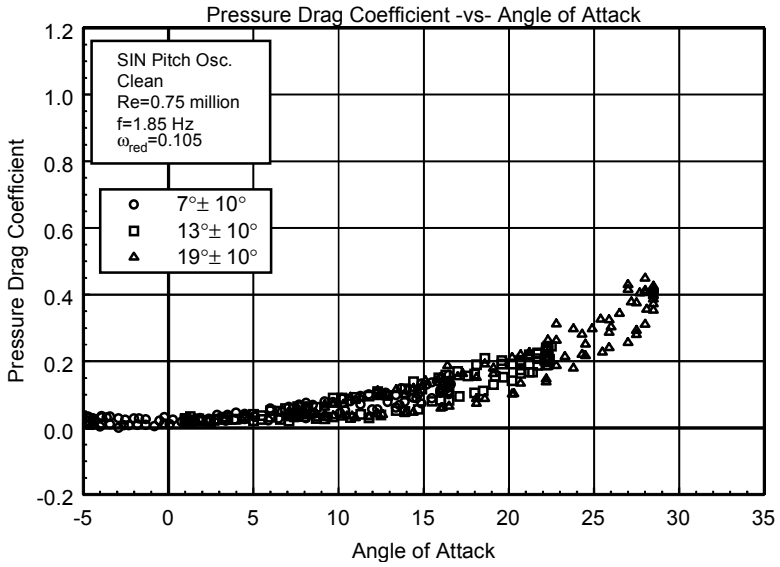

Figure C62. Pressure drag coefficient vs α.

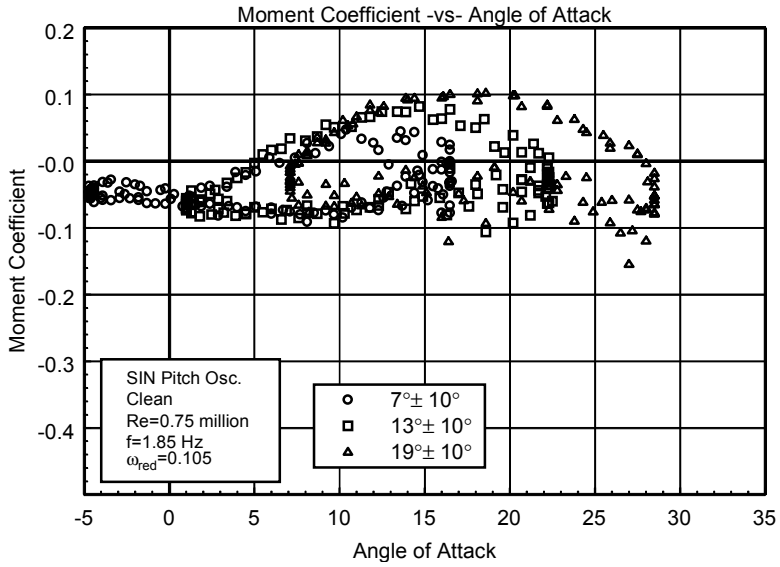

Figure C63. Moment coefficient vs α.

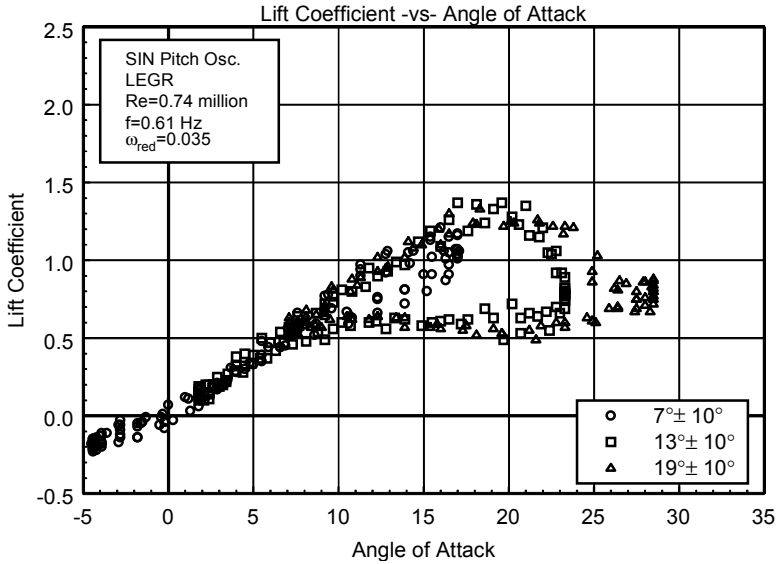

Figure C64. Lift coefficient vs α.

L303
LEGR
Re=0.74 million
$\omega_{reduced}$=0.035

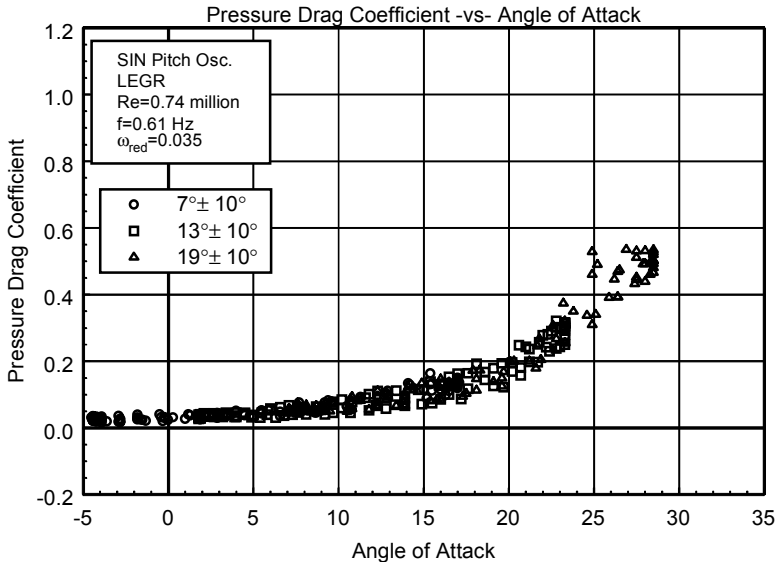

Figure C65. Pressure drag coefficient vs α.

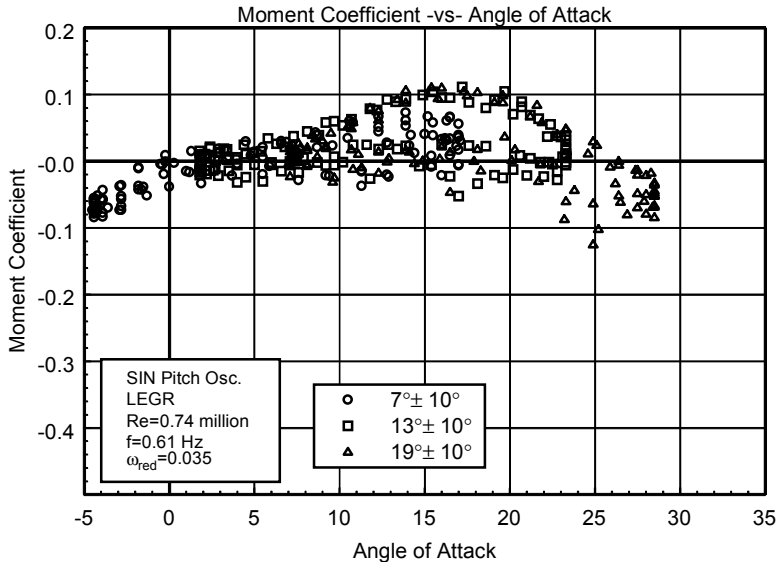

Figure C66. Moment coefficient vs α.

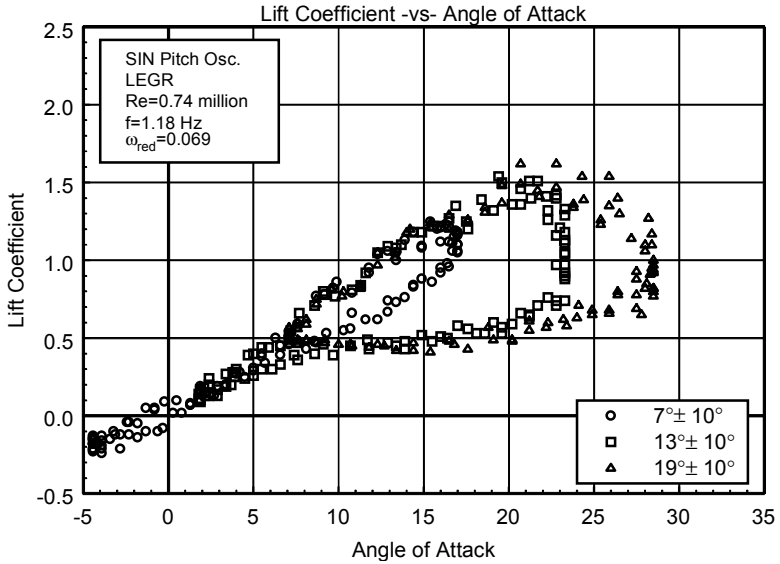

Figure C67. Lift coefficient vs α.

L303
LEGR
Re=0.74 million
$\omega_{reduced}$=0.069

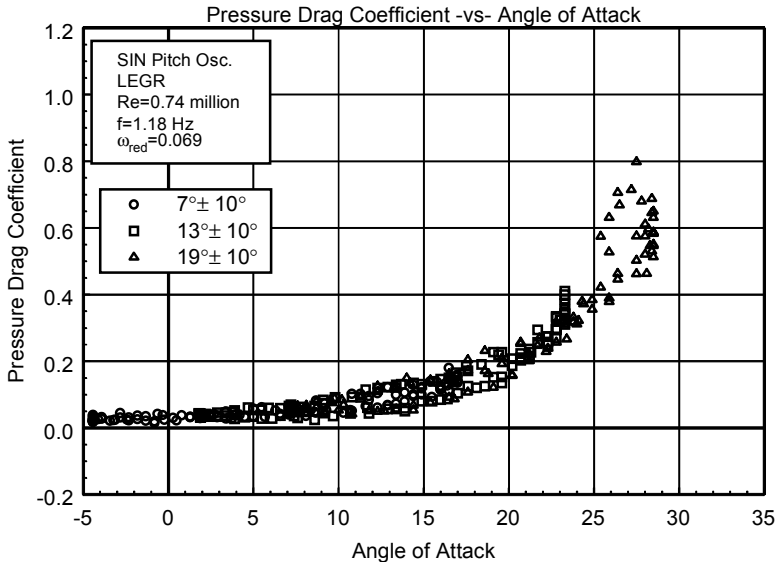

Figure C68. Pressure drag coefficient vs α.

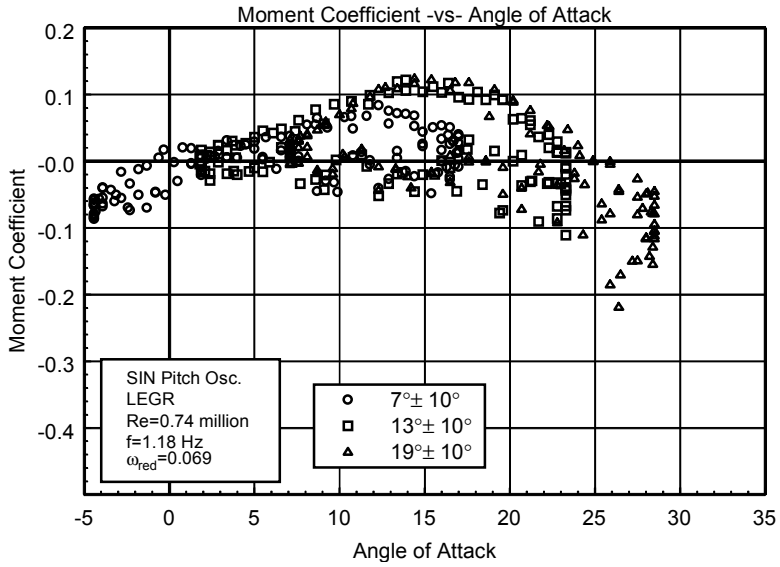

Figure C69. Moment coefficient vs α.

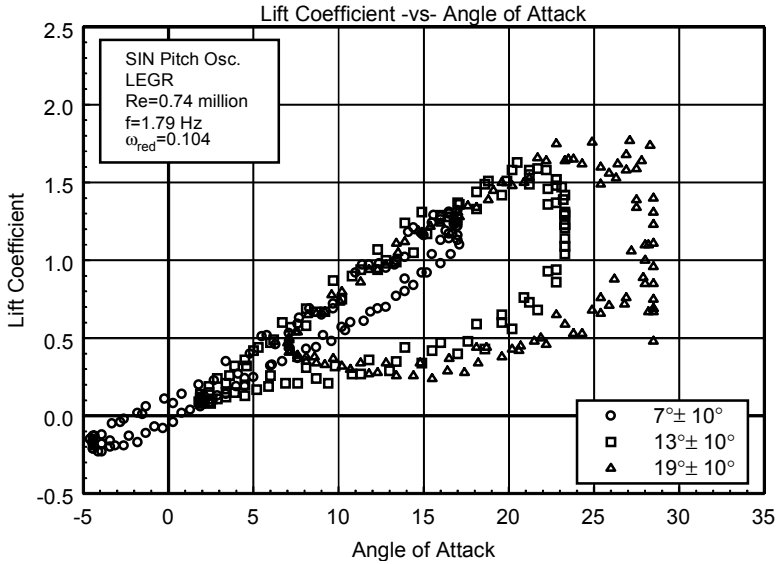

Figure C70. Lift coefficient vs α.

L303
LEGR
Re=0.74 million
$\omega_{reduced}$=0.104

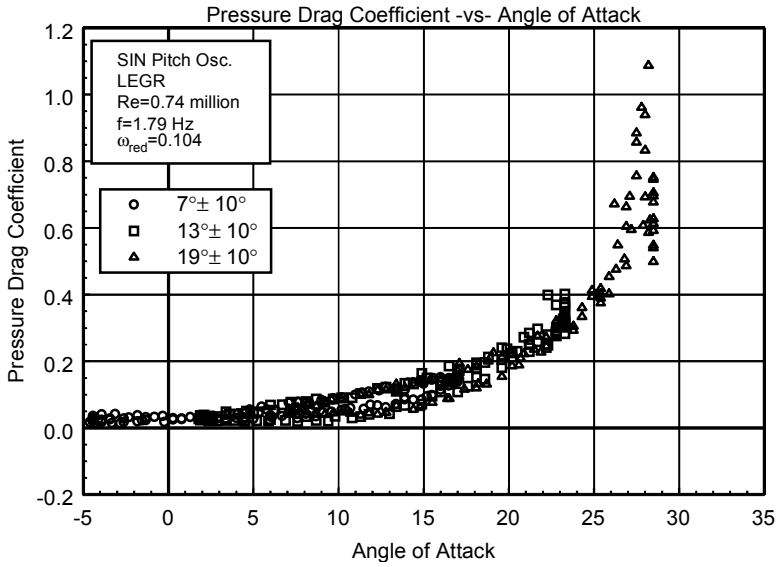

Figure C71. Pressure drag coefficient vs α.

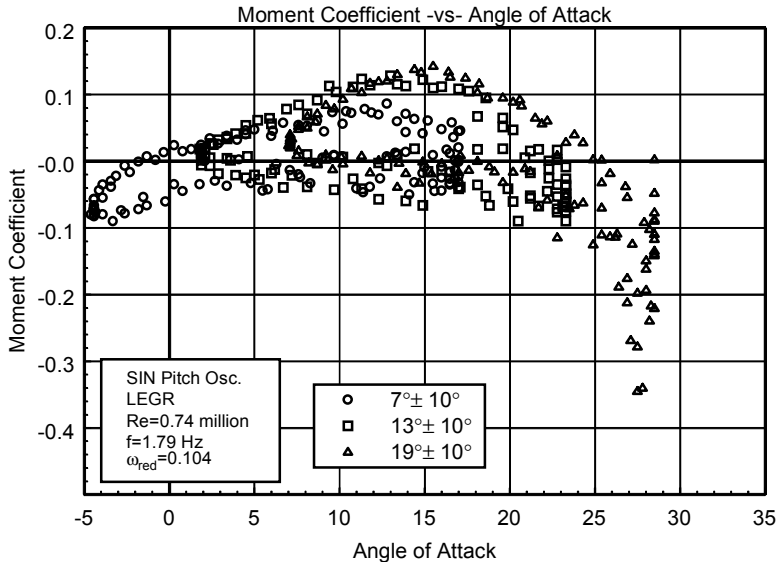

Figure C72. Moment coefficient vs α.

Unsteady Airfoil Characteristics

±10° Sine, Re = 1 million

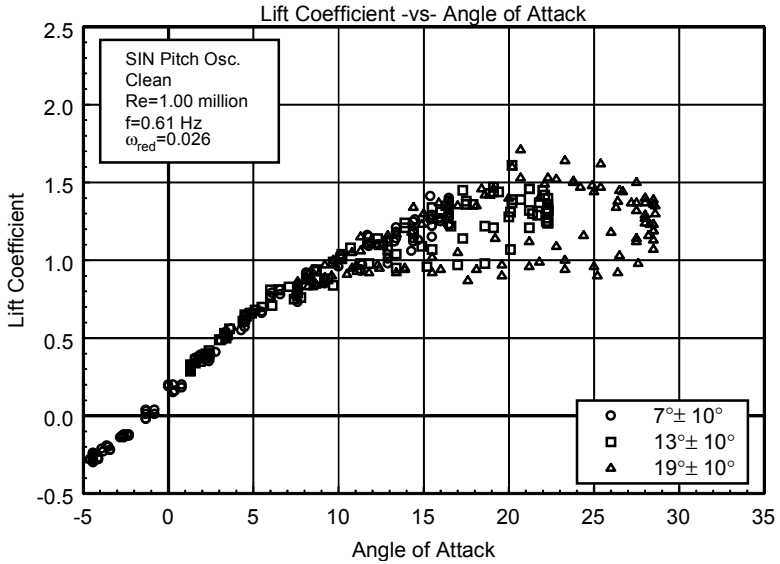

Figure C73. Lift coefficient vs α.

L303
Clean
Re=1.00 million
$\omega_{reduced}$=0.026

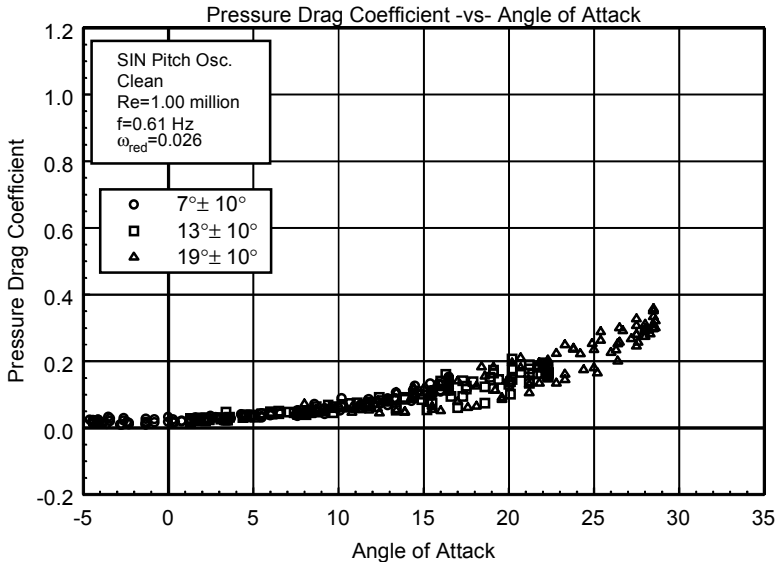

Figure C74. Pressure drag coefficient vs α.

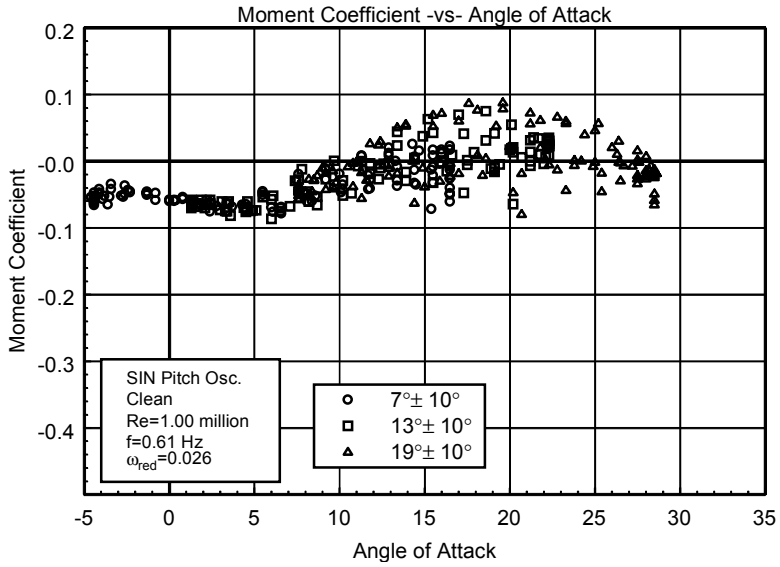

Figure C75. Moment coefficient vs α.

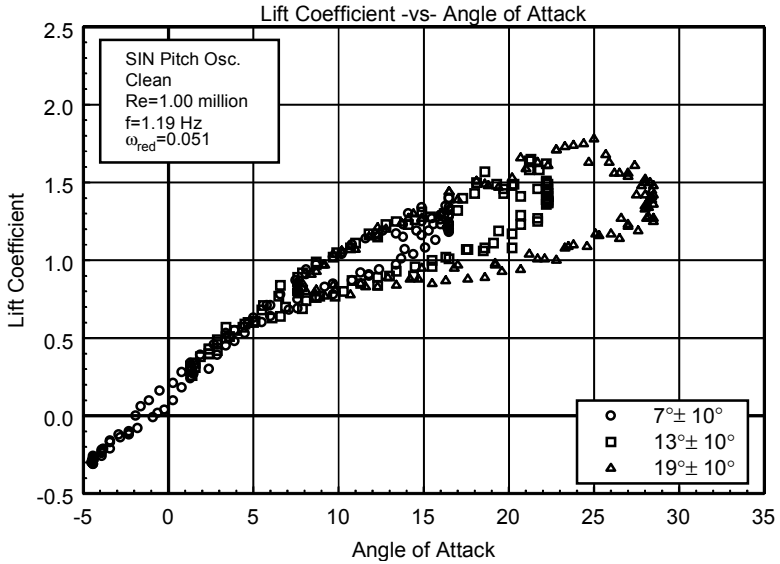

Figure C76. Lift coefficient vs α.

L303
Clean
Re=1.00 million
$\omega_{reduced}$=0.051

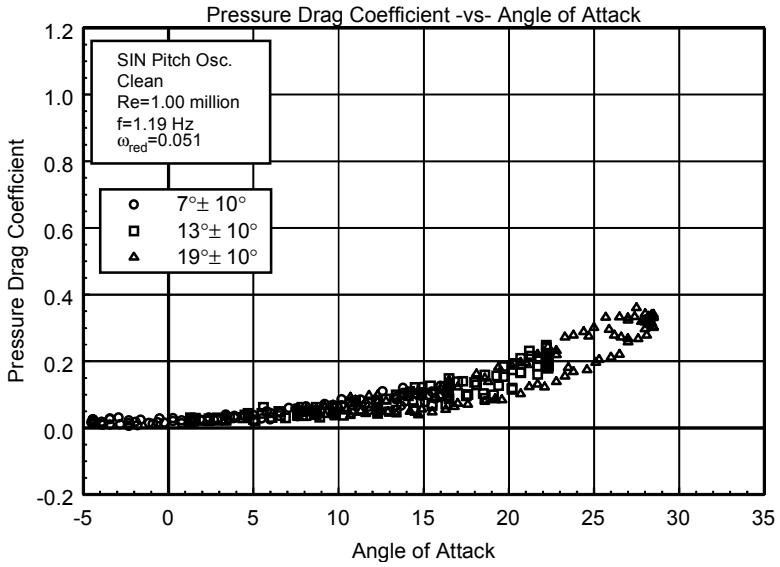

Figure C77. Pressure drag coefficient vs α.

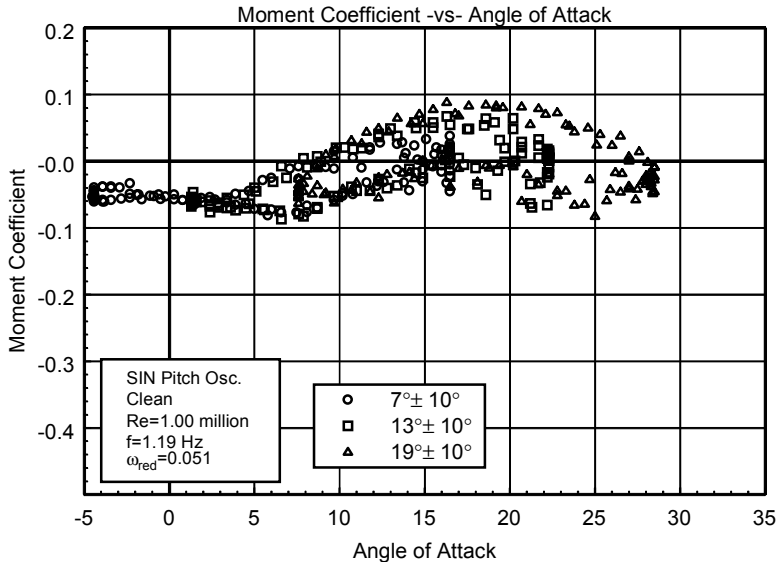

Figure C78. Moment coefficient vs α.

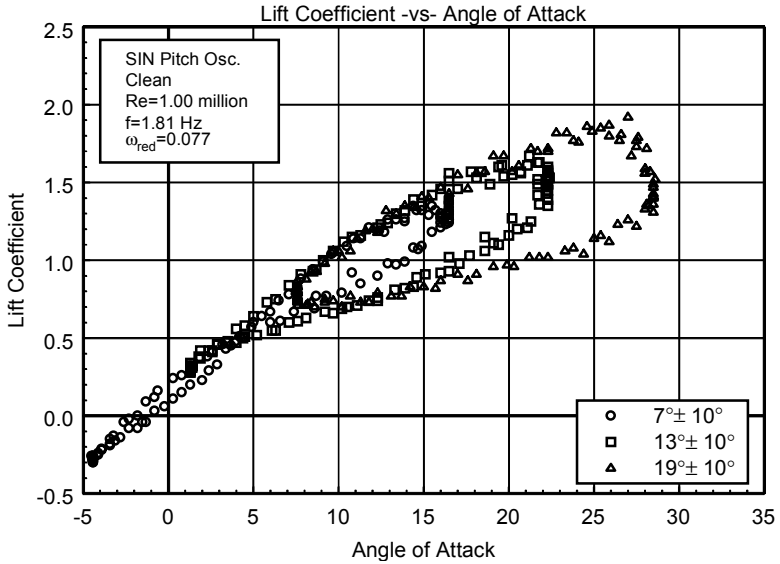

Figure C79. Lift coefficient vs α.

L303
Clean
Re=1.00 million
$\omega_{reduced}$=0.077

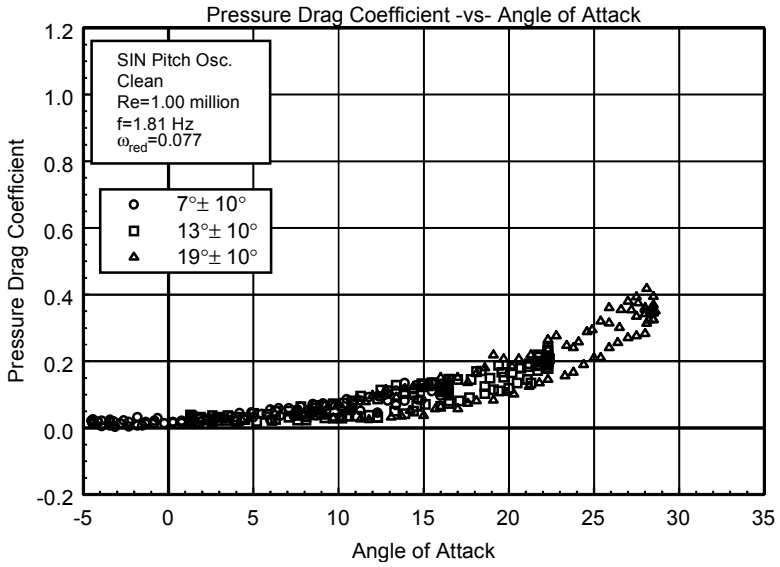

Figure C80. Pressure drag coefficient vs α.

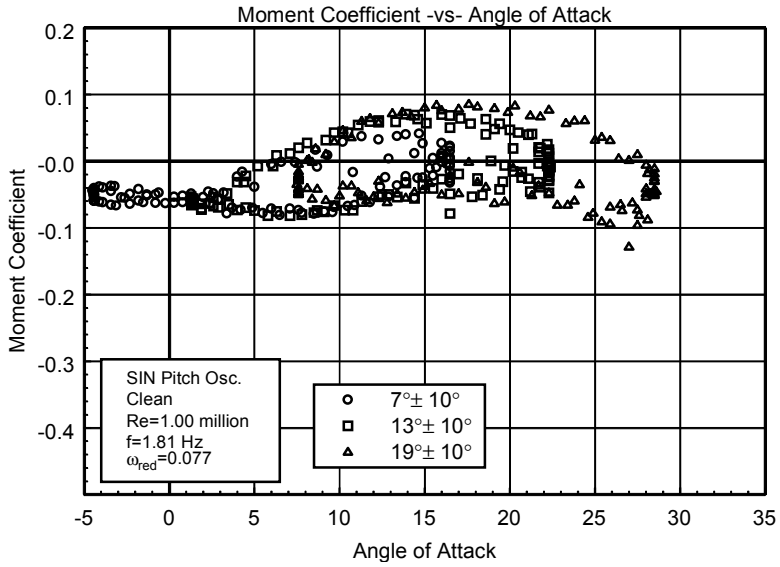

Figure C81. Moment coefficient vs α.

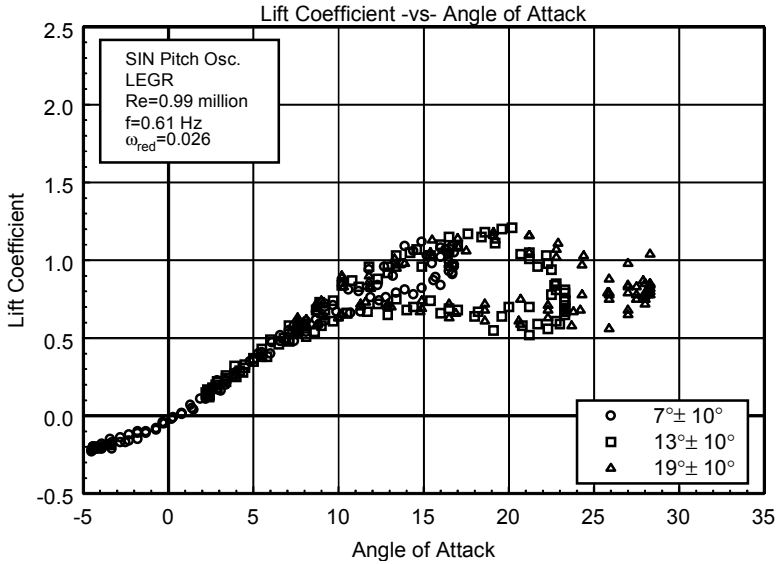

Figure C82. Lift coefficient vs α.

L303
LEGR
Re=0.99 million
$\omega_{reduced}$=0.026

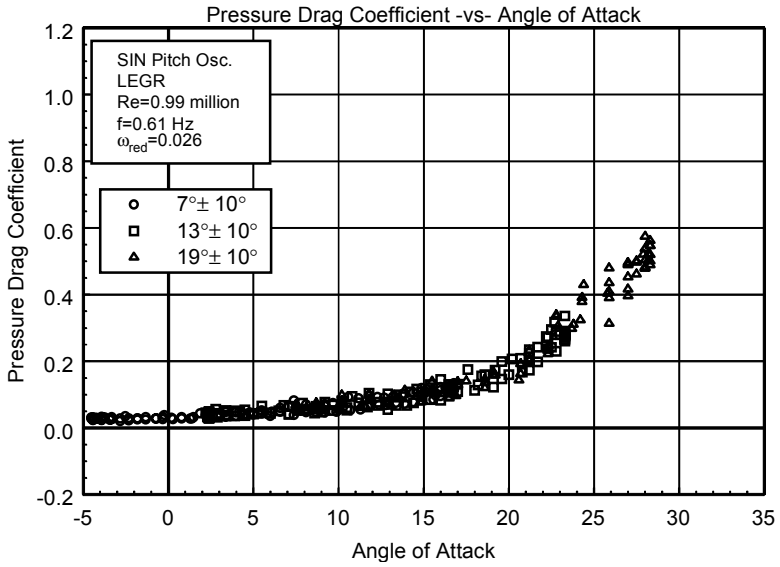

Figure C83. Pressure drag coefficient vs α.

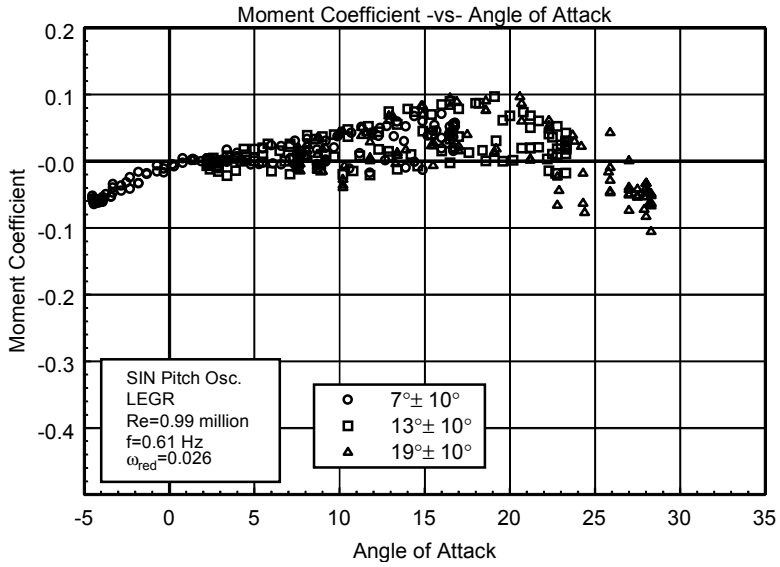

Figure C84. Moment coefficient vs α.

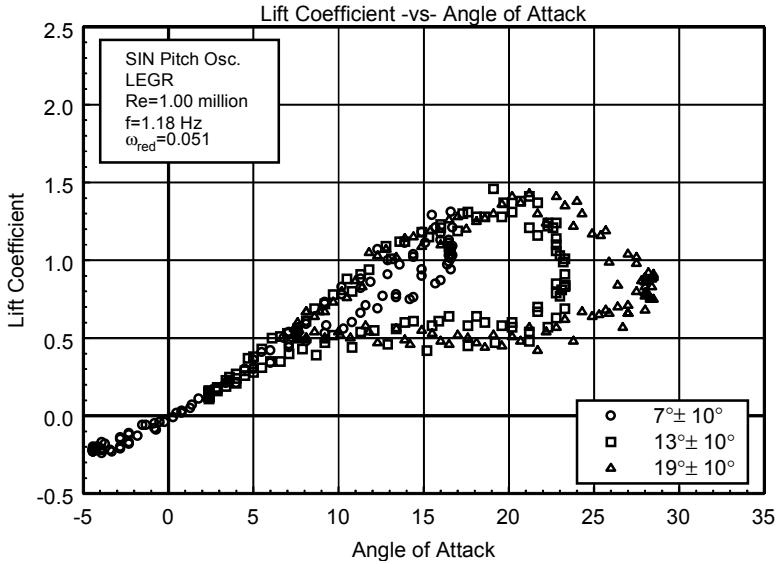

Figure C85. Lift coefficient vs α.

L303
LEGR
Re=1.00 million
$\omega_{reduced}$=0.051

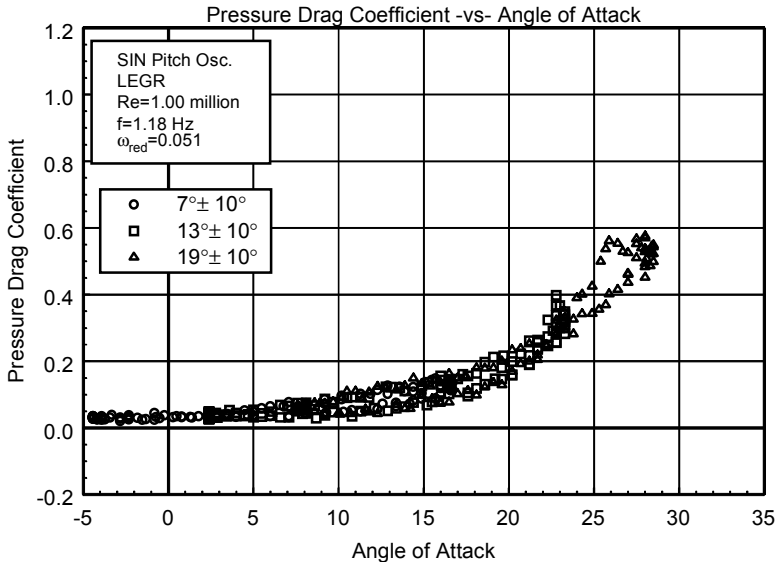

Figure C86. Pressure drag coefficient vs α.

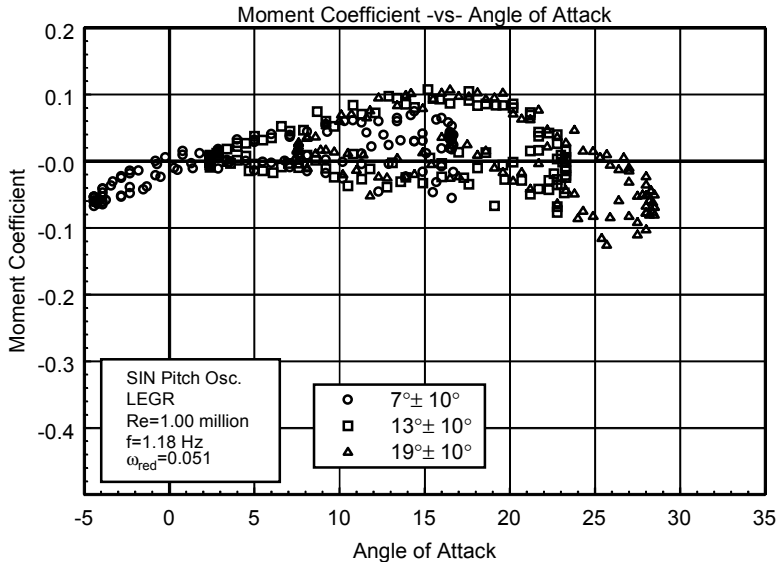

Figure C87. Moment coefficient vs α.

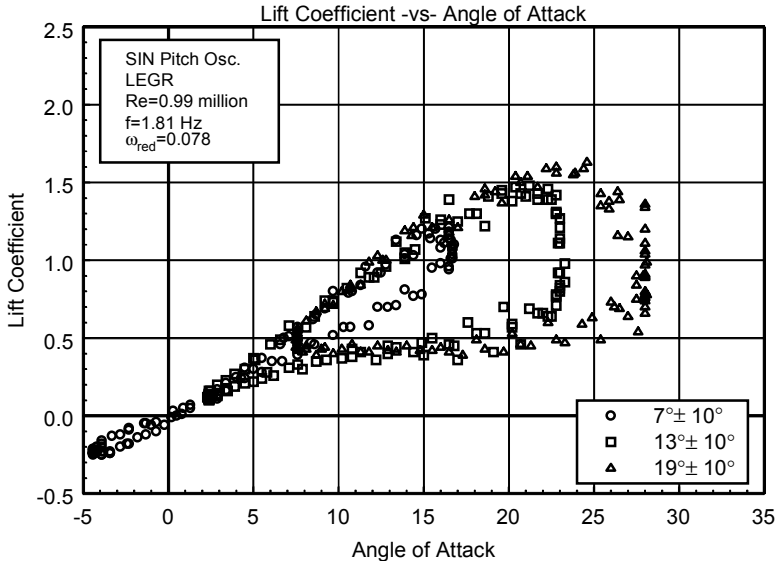

Figure C88. Lift coefficient vs α.

S810
LEGR
Re=0.99 million
$\omega_{reduced}$=0.078

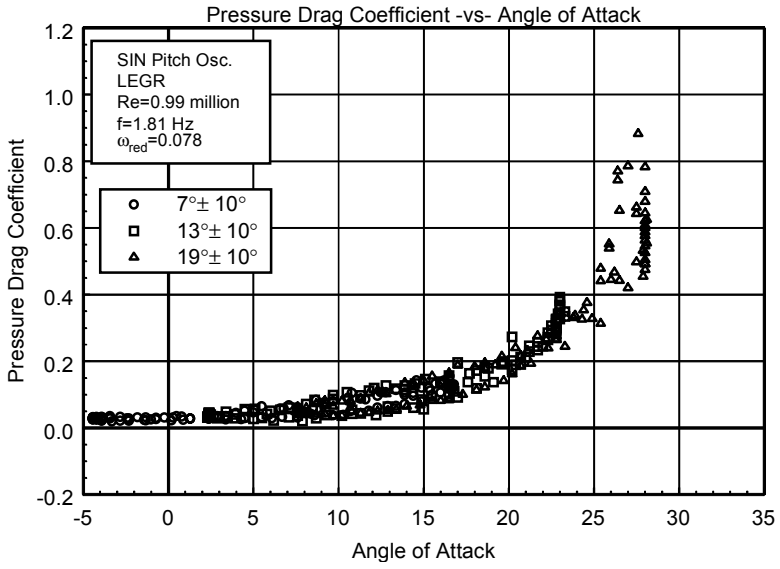

Figure C89. Pressure drag coefficient vs α.

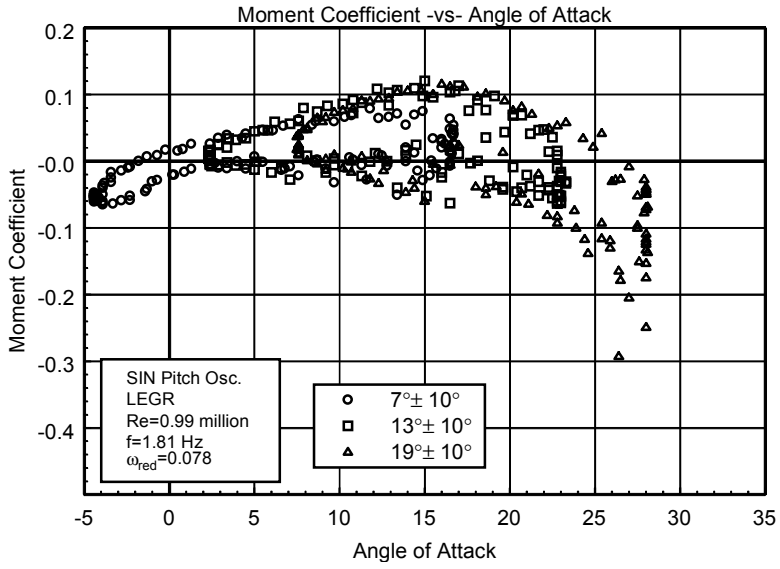

Figure C90. Moment coefficient vs α.

Unsteady Airfoil Characteristics

±10° Sine, Re = 1.25 million

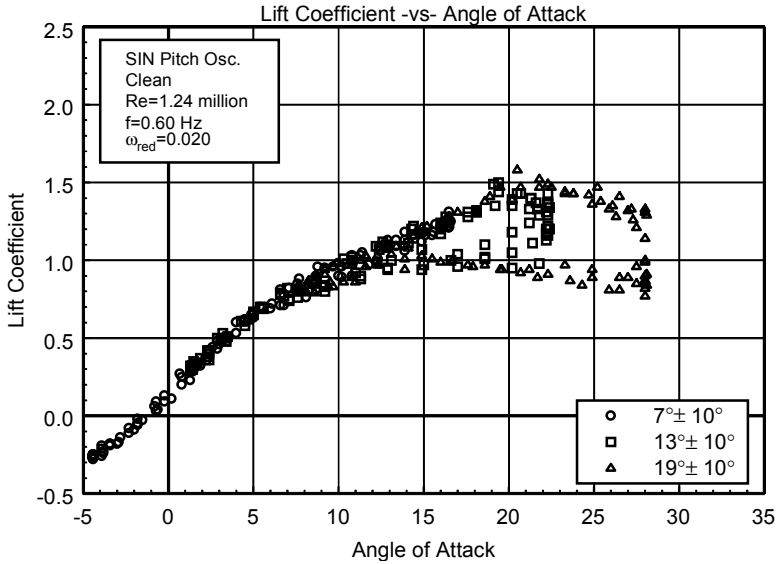

Figure C91. Lift coefficient vs α.

L303
Clean
Re=1.24 million
$\omega_{reduced}$=0.020

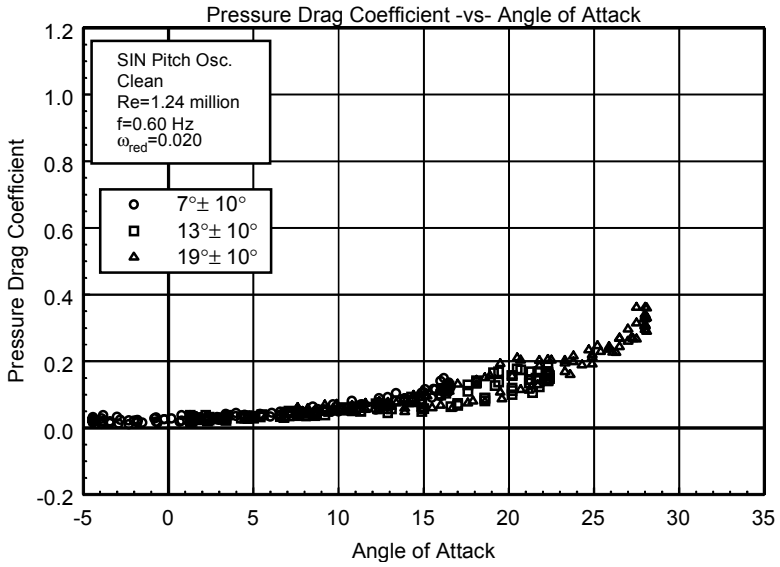

Figure C92. Pressure drag coefficient vs α.

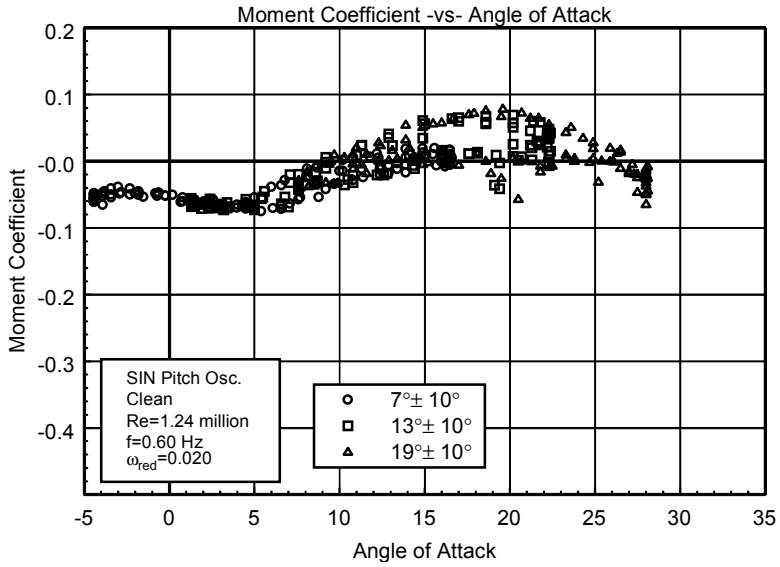

Figure C93. Moment coefficient vs α.

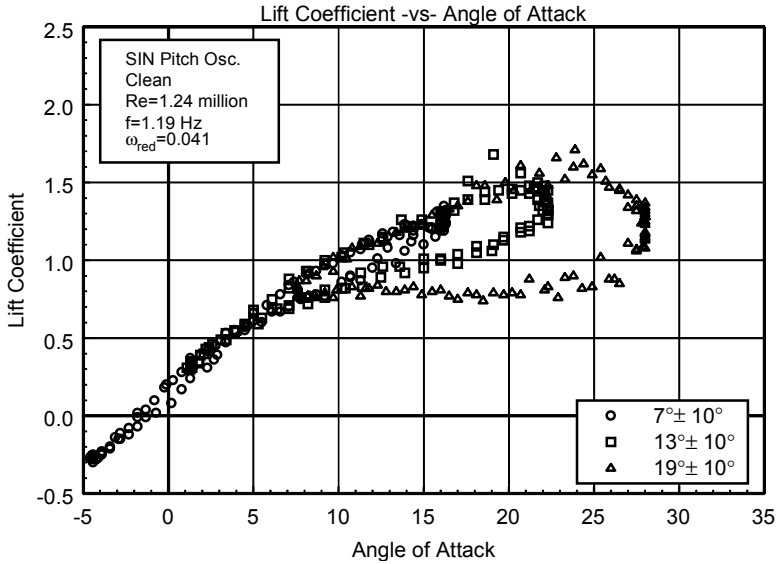

Figure C94. Lift coefficient vs α.

L303
Clean
Re=1.24 million
$\omega_{reduced}$=0.041

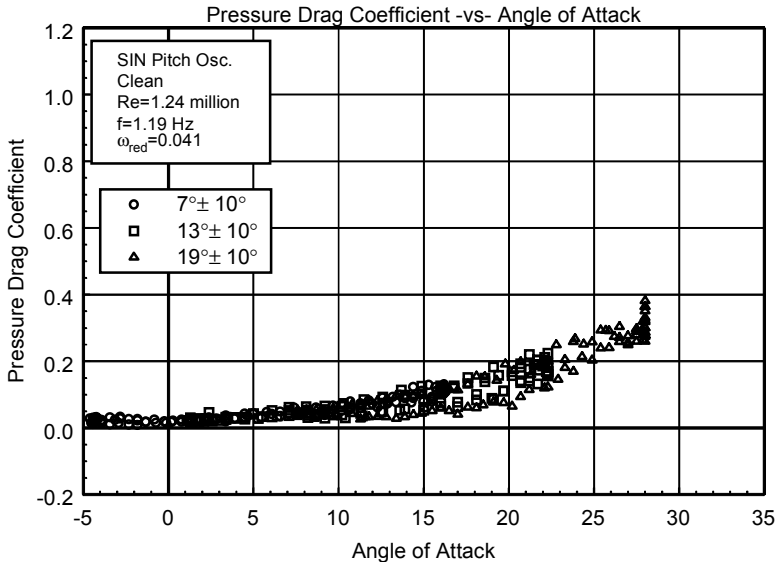

Figure C95. Pressure drag coefficient vs α.

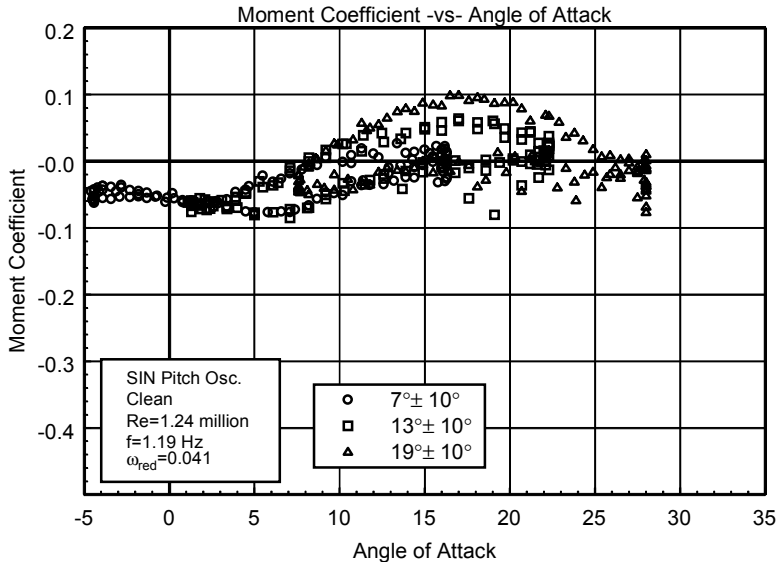

Figure C96. Moment coefficient vs α.

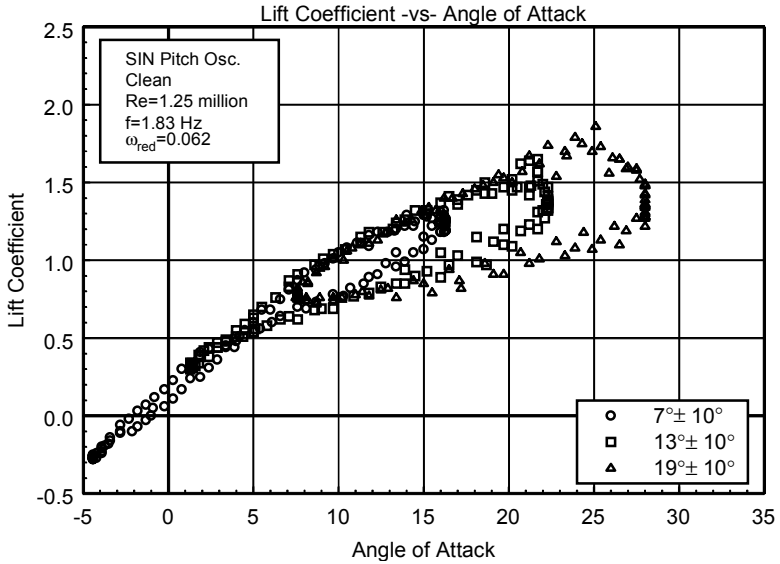

Figure C97. Lift coefficient vs α.

L303
Clean
Re=1.25 million
$\omega_{reduced}$=0.062

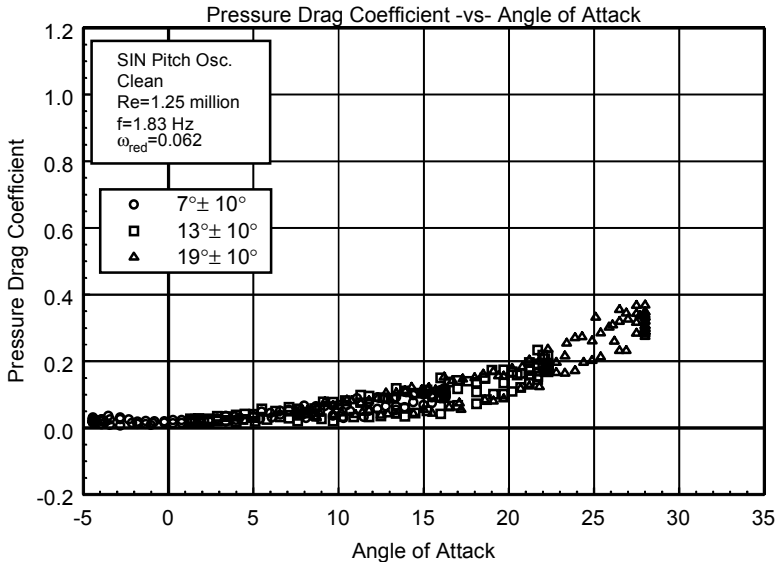

Figure C98. Pressure drag coefficient vs α.

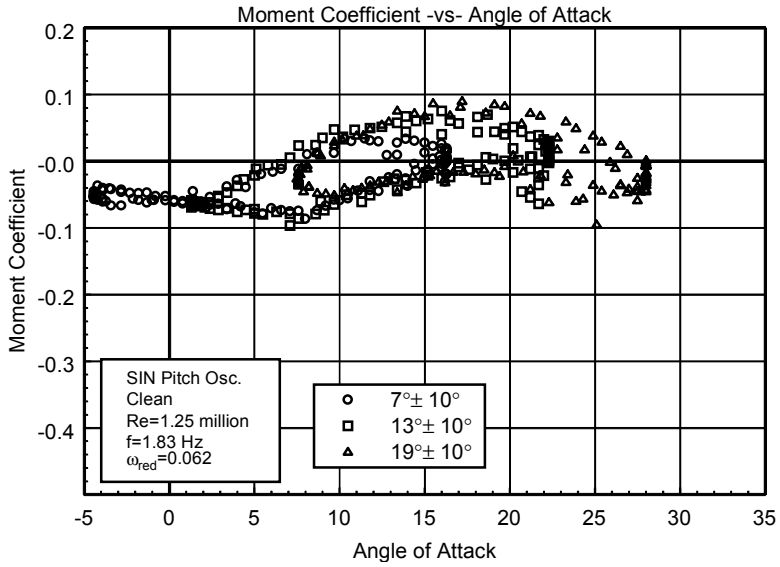

Figure C99. Moment coefficient vs α.

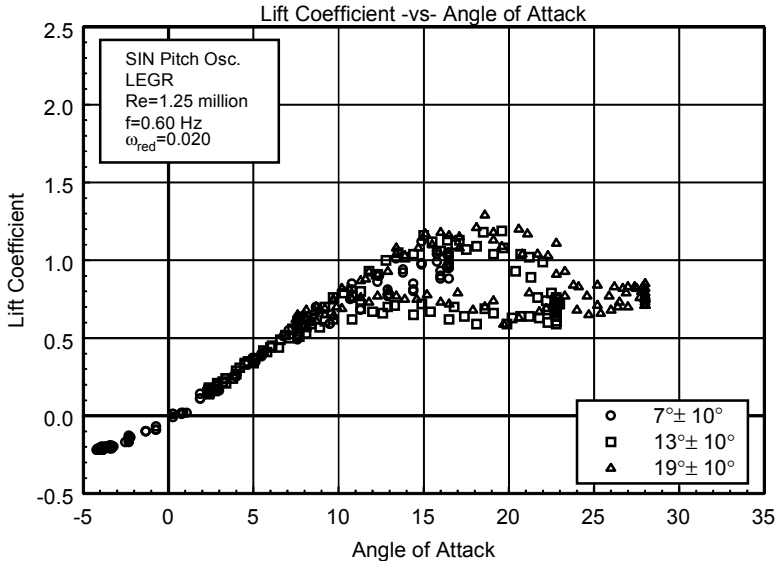

Figure C100. Lift coefficient vs α.

L303
LEGR
Re=1.25 million
$\omega_{reduced}$=0.020

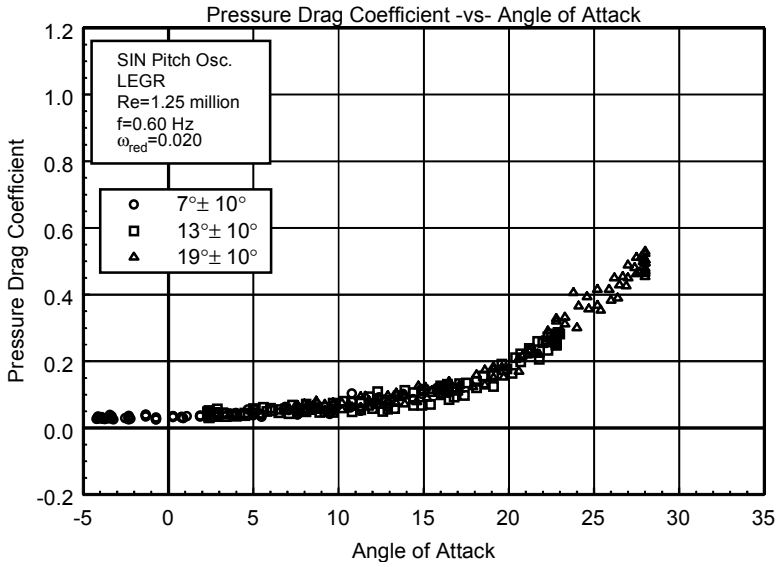

Figure C101. Pressure drag coefficient vs α.

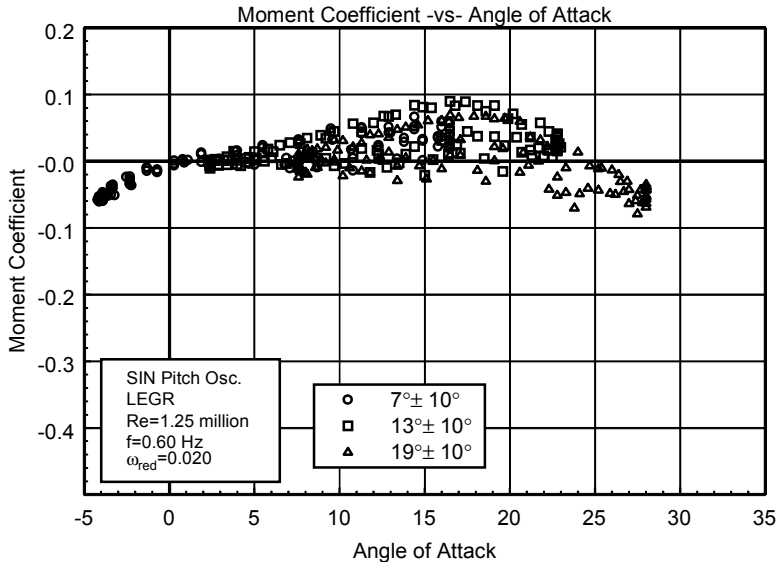

Figure C102. Moment coefficient vs α.

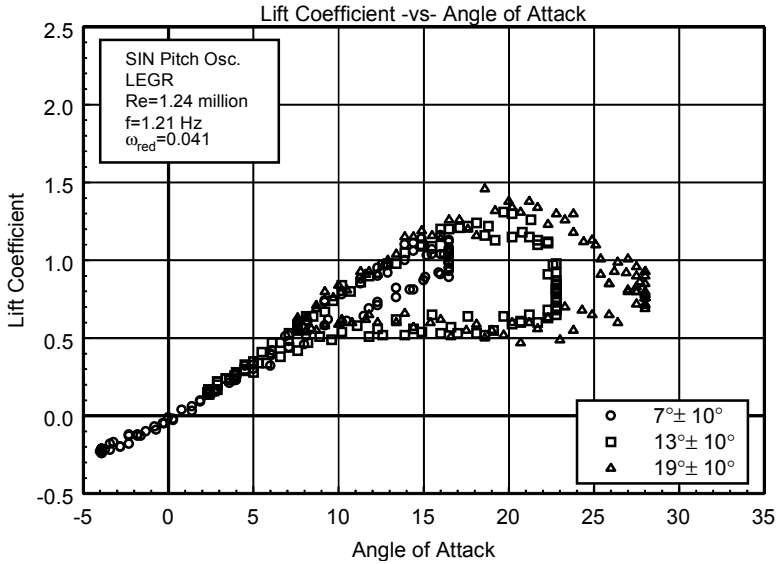

Figure C103. Lift coefficient vs α.

L303
LEGR
Re=1.24 million
$\omega_{reduced}$=0.041

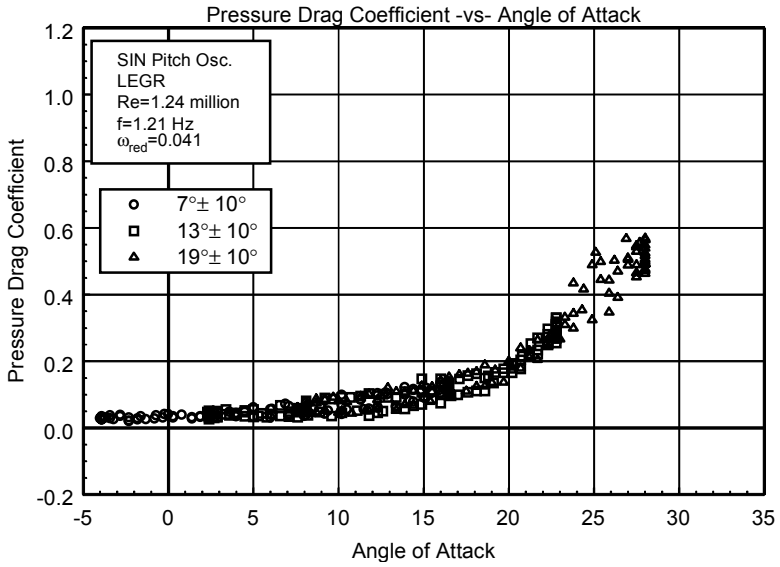

Figure C104. Pressure drag coefficient vs α.

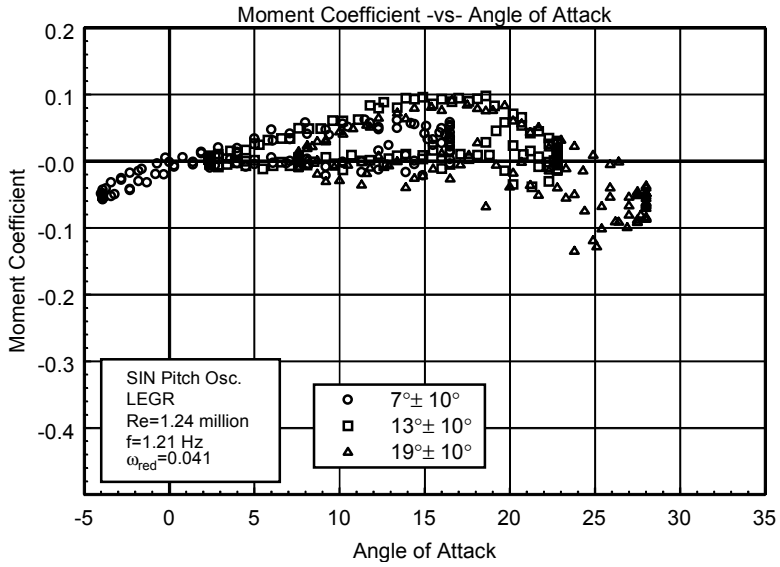

Figure C105. Moment coefficient vs α.

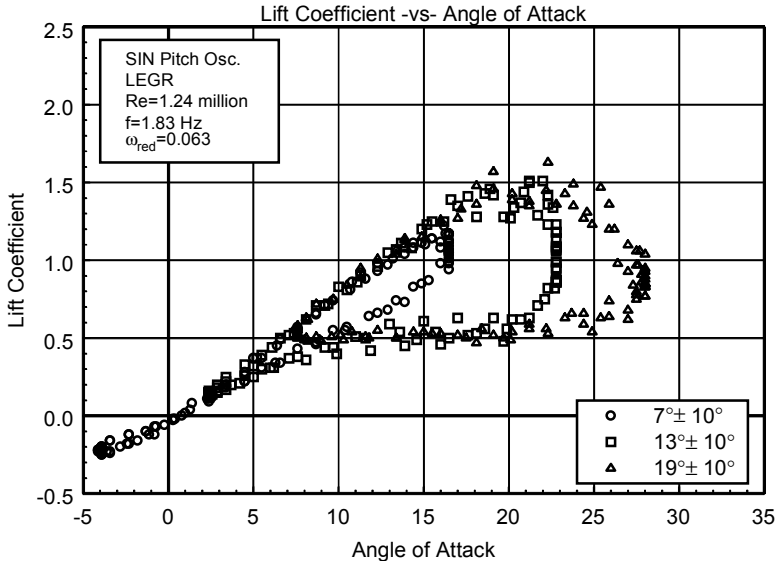

Figure C106. Lift coefficient vs α.

L303
LEGR
Re=1.24 million
$\omega_{reduced}$=0.063

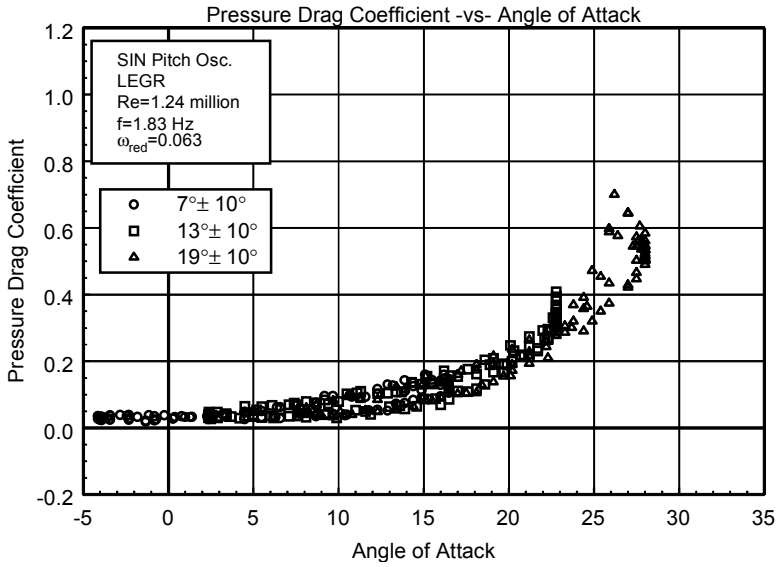

Figure C107. Pressure drag coefficient vs α.

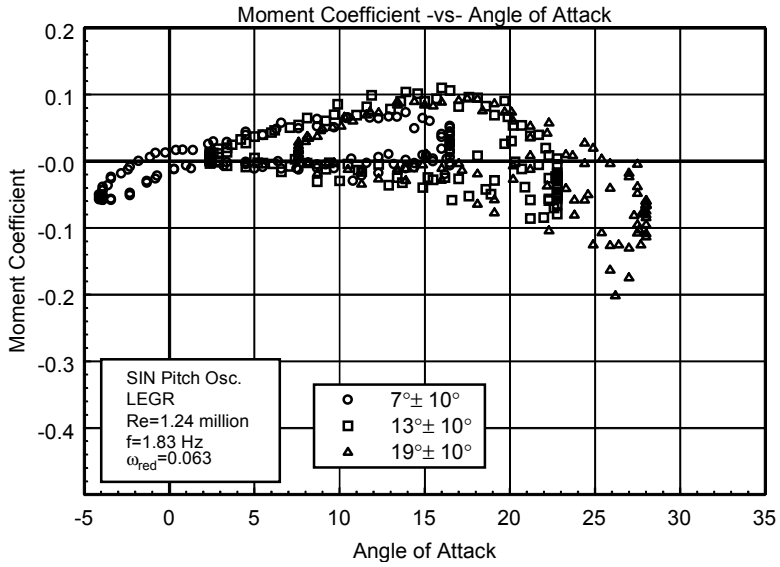

Figure C108. Moment coefficient vs α.